

PONTIFÍCIA UNIVERSIDADE CATÓLICA
DO RIO DE JANEIRO



Thiago de Souza Carnavale

**Soil-Thunder Interaction:
A Field Monitoring Analysis**

Tese de Doutorado

Thesis presented to the Programa de Pós-graduação em Engenharia Civil da PUC-Rio in partial fulfillment of the requirements for the degree of Doutor em Engenharia Civil. Approved by the undersigned Examination Committee.

Advisor: Prof. Tácio Mauro Pereira de Campos
Co-Advisor: Prof. Antônio Roberto Martins Barboza de Oliveira

Rio de Janeiro
November, 2018



Thiago de Souza Carnavale

**Soil-Thunder Interaction:
A Field Monitoring Analysis**

Thesis presented to the Programa de Pós-graduação em Engenharia Civil da PUC-Rio in partial fulfillment of the requirements for the degree of Doutor em Engenharia Civil. Approved by the undersigned Examination Committee.

Prof. Tácio Mauro Pereira de Campos

Advisor

Departamento de Engenharia Civil e Ambiental - PUC-Rio

Prof. Antônio Roberto Barbosa de Oliveira

Co-Advisor

Departamento de Engenharia Civil e Ambiental - PUC-Rio

Prof. Vitor Nascimento Aguiar

Departamento de Engenharia Civil e Ambiental - PUC-Rio

Prof. Fernando Antônio Medeiros Marinho

Universidade de São Paulo

Dr. Haimon Diniz Lopes Alves

Universidade do Estado do Rio de Janeiro

Dr. Sergio Luiz Fontes

Observatório Nacional

Prof. Márcio da Silveira Carvalho

Vice Dean of Graduate Studies

Centro Técnico Científico – PUC-Rio

Rio de Janeiro, November 30th, 2018.

All rights reservd.

Thiago de Souza Carnavale

Bachelor's degree in Geography from Rio de Janeiro State University (UERJ) in 2010. Teacher's degree in Geography from Rio de Janeiro State University (UERJ) in 2011. Master's degree in Civil Engineering (Geotechnics) from the Pontifical Catholic University of Rio de Janeiro - (PUC-Rio) in 2013. Sponsored by the scholarship from CNPq from 2013 to 2015 and from FAPERJ Nota 10 in the period of 2016 and 2017. The main areas of interest and lines of research are: Soil Mechanics, Experimental Geotechnics and Unsaturated Soils.

Bibliographic data

Carnavale, Thiago de Souza

Soil-thunder interaction : a field monitoring analysis / Thiago de Souza Carnavale ; advisor: Tácio Mauro Pereira de Campos ; co-advisor: Antônio Roberto Martins Barboza de Oliveira. – 2018.

137 f. : il. color. ; 30 cm

Tese (doutorado)–Pontifícia Universidade Católica do Rio de Janeiro, Departamento de Engenharia Civil e Ambiental, 2018.

Inclui bibliografia

1. Engenharia Civil e Ambiental - Teses. 2. Trovões. 3. Monitoramento de campo. 4. Técnicas de instalação do EC-5. 5. Monitoramento sísmico de trovões. I. Campos, Tácio Mauro Pereira de. II. Oliveira, Antônio Roberto Martins Barboza de. III. Pontifícia Universidade Católica do Rio de Janeiro. Departamento de Engenharia Civil e Ambiental. IV. Título.

CDD: 624

Acknowledgements

To my advisor, Tácio de Campos. Dear professor, you gave me all the responsibilities to become a good professional in the academic area. Thank you for training me and improve my skills.

To my supervisor, Antônio Roberto. Dear professor, thank you to share your room and knowledge. I have no words to describe how thank I am.

To Natália Carnavale. You are my best partner. Thank you!

To Carmelinda Carnavale, my mother. Thanks to be my first teacher.

To my goddaughters Giovanna and Maitê and my godson Lucas.

To my brother, Victor Carnavale.

To my father, Ricardo Pinto Carnavale, in memory.

To Paula Benedetti, Ricardo Froitzheim.

To my family and friends. Without you it would never have happened.

To professor Franklin Antunes. You are my inspiration in life and work. Thank you to be my friend and advisor!

To professor Haimon Alves for the extremely important contribution in MCT.

To André Barros, Euclides Moura, for technical procedures, helps and friendly.

To Rita and Fátima, for all the support during this long period.

To Observatório Nacional, professor Sergio Fontes Fábio Dias, Thiago Moeda and Ronaldo Marins de Carvalho, for seismic monitoring.

To UFRJ, for tomography procedures.

To CEPEL, for high-voltage experimental contribution.

To Euripedes Vargas, Raquel Veloso and Michele Casagrande for all advices.

To the PUC-Rio staff.

This study was financed in part by the Coordenação de Aperfeiçoamento de Pessoal de Nível Superior - Brasil (CAPES) - Finance Code 001.

To CNPq, FAPERJ, and Brazilian Government, for the financial support during the program.

To PUC-Rio, for the knowledge and training.

Abstract

Carnavale, Thiago de Souza; de Campos, Tácio Mauro Pereira (Advisor); de Oliveira, Antônio Roberto Martins Barboza (Co-Advisor). **Soil-Thunder Interaction: A Field Monitoring Analysis**. Rio de Janeiro, 2018. 137p. Tese de Doutorado - Departamento de Engenharia Civil e Ambiental, Pontifícia Universidade Católica do Rio de Janeiro.

The present thesis aims to evaluate thunder-soil interaction verifying the influence of its induced vibrations to the reduction of the factor of safety in a pseudo-static slope stability analysis. In order to carry out this research, considering the unpublished approach, a theoretical survey was made in order to present the main characteristics of the lightning and its correlations with the soil. As a material, a colluvial soil, mainly composed of quartz, feldspar and biotite was characterized by standard methods (supplemented with the use of 3D microtomography) in order to reveal its mineral composition, structural arrangement and water retention. After field and laboratory calibration of the water potential and volumetric moisture sensors, a long-term field monitoring was performed to evaluate the correlation between climatic data (including lightning incidence) and soil water potential. Finally, a seismographic monitoring station was used to capture the vibrations induced by thunder in the soils. The results depicted 39 lightning events near the field monitoring site. However, no rapid variation of water potential was revealed during thunderstorm days. Seismic monitoring showed that thunder caused micro-seismic signals composed of ground peak accelerations up to 0.02 m/s^2 . In conclusion, for geotechnical purposes, thunder is a subject that can be evaluated in the light of pseudostatic loads. However, further researches are required to verify the vibrations of larger magnitudes, induced by rays that occur at smaller distances of the seismic monitoring point.

Keywords

Soil-thunder correlation; Microtomography for colluvial soil; EC-5 installing procedures comparison; Correlation of meteorological and soil-suction data; Thunder as a micro-seismic source.

Resumo

Carnavale, Thiago de Souza; de Campos, Tácio Mauro Pereira (Orientador); de Oliveira, Antônio Roberto Martins Barboza (Coorientador). **Interação solo-trovão: Uma análise de monitoramento de campo.** Rio de Janeiro, 2018. 137p. Tese de Doutorado - Departamento de Engenharia Civil e Ambiental, Pontifícia Universidade Católica do Rio de Janeiro.

A presente tese tem como objetivo avaliar a interação trovão-solo no que toca a ocorrência de trovões e suas características microssísmicas, apontando a influência de vibrações induzidas para a redução do fator de segurança em uma análise (pseudo-estática) de estabilidade de encostas. Considerando a abordagem inédita, foi efetuado um levantamento teórico com o intuito de apresentar as principais características dos relâmpagos e suas correlações com o solo. Como material, foi utilizado um solo coluvionar, composto principalmente de quartzo, feldspato e biotita. O referido foi caracterizado através de métodos padrão (complementados com o uso da microtomografia 3D), e a retenção e disponibilidade de água foram reveladas. Foi efetuado um monitoramento de campo de longo prazo para avaliar a correlação entre os dados climáticos (incluindo incidência de raios) e o potencial hídrico dos solos. Por fim, foi utilizada uma estação para monitoramento sismográfico para captar as vibrações induzidas por trovões nos solos. Os resultados mostram 39 ocorrências de raios próximos ao local de monitoramento de campo. O monitoramento sísmico mostrou que os trovões causam sinais microssísmicos compostos por acelerações de pico do solo até $0,02 \text{ m/s}^2$. Em conclusão, para fins geotécnicos, o trovão é um assunto que pode ser avaliado à luz de um carregamento sísmico.

Palavras-chave

Interação solo-trovão; Microtomografia para solo coluvionar; Procedimentos de instalação sensores de umidade volumétrica; Correlação clima – meteorologia - sucção do solo; Trovão como uma fonte microssísmica.

Summary	
1 Introduction	13
1.1. Organisation of the thesis	14
2 Lightning	21
2.1. Motivation	22
2.2. Lightning	25
2.3. Lightning-soil interaction	26
2.4. Electrical influences	27
2.5. Thunder – Formation. pressure and seismic	32
2.6. Conclusion	38
3 Using 3D microtomography for soil characterisation	40
3.1. Review (3D Microtomography)	41
3.2. Materials and Methods	47
3.3. Physical Characterisation	49
3.4. Chemical - Mineralogical Characterisation	51
3.5. Structural Characterisation	56
3.6. 3D Microtomography	60
3.7. Conclusion	64
4 A correlation between laboratory and field monitoring data	65
4.1. Review	67
4.2. Materials	70
4.3. Methods	70
4.4. Results	78
4.5. Conclusions	85
5 Soil-atmosphere interactions	87
5.1. Environmental background	89
5.2. Soil characterisation	91
5.3. Field monitoring	93
5.4. Results	94
5.5. Conclusions	103
6 Thunder: A micro seismic atmospheric source	104
6.1. Review	106
6.2. Methods	108
6.3. Results	115
6.4. Conclusions – Final considerations	120
7 Final considerations	121
8 References	122

Figure Contents

Figure 1.1 - Thesis' organisation	15
Figure 2.1 - Landslides in the mountainous region of Rio de Janeiro. (Photo taken by F. Dourado on January 13th, 2011)	22
Figure 2.2 - Relation between the total number of rays and the types of Brazilian soils (hatched bars).	26
Figure 2.3 - Highvolt pulse generator. (SF) Spherical charging steps. (Rd. Re and Rs) Resistive components. (Cs) Charging capacitive redemption components	27
Figure 2.4 - Simulated lightning developed in the lab and borehole caused in the soil	28
Figure 2.5 - Microtomography. Top (a) and central hole (b) images	28
Figure 2.6 - A Florida fulgurite of about 5 m length excavated by the University of Florida lightning research group (Rakov & Uman, 2003)	29
Figure 2.7 - Simulated lightning developed in the lab	30
Figure 2.8 - Unconfined strength tests for the samples struck and non-struck by replicated lightning versus moisture content and matric suction	32
Figure 2.9 - Thunder sound formation scheme - ignoring refraction effects (from RIBNER et al. 1975)	33
Figure 2.10 - Refraction cut-off. Effects of curved atmospheric temperature variations on the sound rays causing the observer to hear only the rays that are between points a and b (from Ribner et al. 1975)	33
Figure 2.11 - a) Replicated thunder sound. b) Test setup	35
Figure 2.12 – Matric suction (T5X) versus simulated thunders	36
Figure 2.13 - (a) Event 1 total pressure and ground velocity recorded by the array. (b) Velocity particle motion for surface and borehole sensors for event 1. The numbers (1 – 5) in the particle-motion plot represent the time sequence from 1 (initial) to 5 (end), (Lin & Langston. 2007)	37
Figure 2.14 - Seismogram obtained during a thunderstorm (Voss <i>et al.</i> , 2015)	38
Figure 3.1 - Acquisition and reconstruction of the simplified scheme (Alves, 2015)	44

Figure 3.2 - a) RAW microtomography image. b) Mineral segmentation (Alves, 2015)	46
Figure 3.3 - Grain size distribution of the analysed soils	49
Figure 3.4 - Grain size distribution: S1 (a), UD – using dispersive solution; UG – using CILAS 1198; ND – without dispersive solution	51
Figure 3.5 - Column (a) – Moistened samples. Column (b) Washed material retained on the sieve #40	53
Figure 3.6 - Washed materials, retained on the #40	54
Figure 3.7 - Diffractogram. Ct = Kaolinite / Gb = Gibbsite / Q = Quartz	55
Figure 3.8 - S1 Differential Thermal Analysis (DTA)	56
Figure 3.9 - Soil water retention curve of sample S1, S2, S3 and S4	56
Figure 3.10 - Pore size distribution and mercury intrusion distribution	58
Figure 3.11- S1 (a), S2 (b), S3 (c) and S4 (d)	59
Figure 3.12 - SEM of soils	60
Figure 3.13 - Internal distribution of the porosity	61
Figure 3.14 - 3D-Microtomography images	63
Figure 4.1 - a) EC-5 and b) MPS-2	71
Figure 4.2 - Principle of operation of the EC-5 probe (Decagon, 2014)	72
Figure 4.3 - MPS-2 (Decagon, 2014)	72
Figure 4.4 - a) Dielectric constant vs. soil volumetric moisture. b) Dielectric constant vs. soil bulk density. (Cihlar & Ulaby, 1976)	73
Figure 4.5 - Normal Proctor (a) and double ring compaction tests (b)	74
Figure 4.6 - Hydraulic compaction (a to c)	75
Figure 4.7 - Drying monitoring procedure	75

Figure 4.8 - Different installation procedures: driving the rod directly into the soil (a), with mud support (b), and with a hardened steel gauge (c)	76
Figure 4.9 - GE (phoenix v tome x m)	77
Figure 4.10 - Filter paper laboratory soil water retention curve	78
Figure 4.11 - Bulk density and volumetric water content	79
Figure 4.12 - Filter paper vs. sensors readings. EC-5 vertical adjustment and limits for MPS-2	80
Figure 4.13 - Comparing installing equipment technics of field soil water retention curve and lab values	81
Figure 4.14 - Microtomography images – rendering the first 10 cm height	82
Figure 4.15: 3D-microtomography pore calculations.	83
Figure 4.16 - Tomography images. Interaction between the probe and the ground	84
Figure 4.17 - Higher resolution microtomography images	85
Figure 5.1 - Filter Paper Method – Soil Water Retention Curve (SWRC)	92
Figure 5.2 - System used for soil moisture monitoring	93
Figure 5.3 - PUC-Rio, Tinguá Experimental Campus	94
Figure 5.4 - Correlation between rainfall, matric potential and soil temperature - 2014	95
Figure 5.5 - Correlation between rainfall, matric potential and soil temperature - 2015	96
Figure 5.6 - Correlation between rainfall, soil temperature and suction – 2016	97
Figure 5.7 - Correlation between rainfall, water potential and soil temperature – 2017	98
Figure 5.8 - Correlation between atmospheric and soil data – Event 1	99
Figure 5.9 - Soil water retention curve and drying-wetting cycling points	101
Figure 5.10 - Lightning distribution during 21, 23, 26 and 29 of December 2017	102

Figure 5.11 - Rainfall and Suction during thunderstorm period	102
Figure 6.1 - Distribution of casualties in Brazil due to rainfall-induced landslides from January 1988 to May 2016 (data reproduced from IPT, 2016)	105
Figure 6.2 - Increase of atmospheric pressure caused by lightning incidence vs. distance	107
Figure 6.3 - Tinguá experimental campus	109
Figure 6.4 - Experimental apparatus. a) STS-2 Seismometer. b) Baler PB44. c) Q-330	109
Figure 6.5 - STS-2 internal arrangement. The 3 obliquely-oriented sensors (Quanterra, 1996)	110
Figure 6.6 - Seismographic equipment setup	112
Figure 6.7 - Installing procedure and field disposal	112
Figure 6.8 - Seismic forces kh and kv	113
Figure 6.9 - Yield coefficient (ky)	114
Figure 6.10 - Lightning distribution	116
Figure 6.11 - Lightning L5. Acceleration vs Time (a); dB vs Frequency (b)	117
Figure 6.12 - Lightning L22. Acceleration vs Time (a); dB vs Frequency (b)	117
Figure 6.13 - Lightning L21. Acceleration vs Time (a); dB vs Frequency (b)	118
Figure 6.14 - Lightning L34. Acceleration vs Time (a); dB vs Frequency (b)	118
Figure 6.15 - Lightning L10. Acceleration vs Time (a); dB vs Frequency (b)	118
Figure 6.16 - Lightning L23. Acceleration vs Time (a); dB vs Frequency (b)	118
Figure 6.17 - Comparison of horizontal seismic coefficient obtained during thunder monitoring (PGA and $\frac{1}{2}$ of PGA) and Yield coefficient	119

Table Contents

Table 1.1. - Chapter 2 organisation	16
Table 1.2. - Chapter 3 organisation	17
Table 1.3. - Chapter 4 organisation	18
Table 1.4. Chapter 5 organisation	19
Table 1.5. - Chapter 6 organisation	20
Table 2.1. - General statistical data – Incidence of lightning	24
Table 2.2. - Effective shear strength - soil struck and non-struck by simulated lightning	31
Table 3.1. - Physical indexes	49
Table 3.2. - Grain size distribution (GSD)	50
Table 3.3. - Atterberg limits	51
Table 3.4. - Chemical analyses	52
Table 3.5. - Microtomography	61
Table 4.1. - Grain size distribution (GSD) data	70
Table 4.2. - Physical Index	70
Table 4.3. - Compaction methods – VWC EC-5 readings vs. p_n	78
Table 4.4.: 3D-Microtomography – pore calculations.	83
Table 5.1. - Physical Index of the samples	91
Table 5.2. - Grain size distribution (GSD)	91
Table 5.3. - Time-interval used for correlation	101
Table 6.1. - Horizontal seismic coefficient.	114
Table 6.2 - Relative Position of K_y and PGA	114
Table 6.3. - Slope geometries	115
Table 6.4. - Lightning spatial distribution	115
Table 6.5. - Distances of lightning occurrences in comparison with sampling point (seismic monitoring)	116
Table 6.6. - k_h and the equivalent FOS	119

1 Introduction

This research was performed in order to contribute to the explanation of a huge natural disaster, which is considered as one of the worst in Brazil's history. At that time, the infiltration processes raised from rainwater and pore water pressure increase on the slope basis, may not have been the unique or the main factor responsible for numerous triggered movements. In such a case, there is a possibility that vibrations processes from thunders may have had some relevance as well.

To investigate such hypothesis, a bibliographic survey revealed the principal aspects concerned to the lightning, soils and eventually slope stability scenario. Thus, a background is described, emphasizing the main characteristics of rays and thunders, suggesting them as potential disturbance agents, and pointing out the interaction between thunders and soils as a relevant research to be carried out.

A colluvial soil was used. Further, regarding methods, and laboratory and field routines were performed as follows:

- Simulated lightning: Soil samples were subjected to electric discharges in order to evaluate the correlation between soil and the electric discharge. In addition, triaxial and unconfined compressive tests were performed to verify the stiffness changes of the soils.
- Soil characterisation: The material was characterised in laboratory by standard methods (comprised by physic, mineral, structural characterisations). In addition, 3D-microtomography procedures were used to complement the structural and mineral data of the undisturbed soil samples.
- Sensor calibration: calibration of field equipment (EC-5 and MPS-2) was required, and different installing technique were tested to evaluate the most efficient procedure for field monitoring.
- Field monitoring: A long-term field monitoring was performed and the correlation between atmospheric parameters (as such thunderstorms) and water potential was evaluated for a soil profile.
- Vibrations monitoring: The lightning incidences were monitored, the vibrations caused by thunders were quantified and the obtained accelerations were applied into a pseudostatic slope stability analyse of a hypothetical slope stability problem.

1.1.

Organisation of the thesis

The aim of the current thesis is to analyse lightning, thunders in particular, as an atmospheric seismic source. To perform this analysis, five steps have been spread over chapters in the paper format, disposed by the central structure (Figure 1.1) and its own results:

Chapter 2: *Lightning: A review of its formation and its potential effects on soils slope stability.* In this chapter, the primary aim is to present the characteristics of lightning, depicting its interactions with soils (Table 1.1).

Chapter 3: *Using 3D microtomography for soil characterisation.* In this chapter, the main aim is to present the internal imaging procedures as a complementary tool for soil characterisation (Table 1.2).

Chapter 4: *A correlation between laboratory and field monitoring data: Producing a reliable Soil Water Retention Curve.* In this chapter, the principle aims concerns probing calibrations and their installation procedures in the light of the production of reliable field monitoring data of volumetric water content and matric potential (Table 1.3).

Chapter 5: *Soil-atmosphere interaction: Using field monitoring to evaluate rapid matric potential changes.* The aim of this chapter pertains to the saturation processes and its interaction with atmospheric parameters, especially during days of thunderstorms (Table 1.4).

Chapter 6: *Thunder: A micro-seismic atmospheric source.* This chapter presents seismic field monitoring; further, it includes a lightning incidence cross-checking. Essentially, it aims to quantify the maximum acceleration induced by thunders and analyse the incidence of distance-acceleration correlation. Additionally, a pseudo-static hypothetical slope-stability analysis is performed (Table 1.5).

Finally, in Chapter 7, the conclusions are presented.

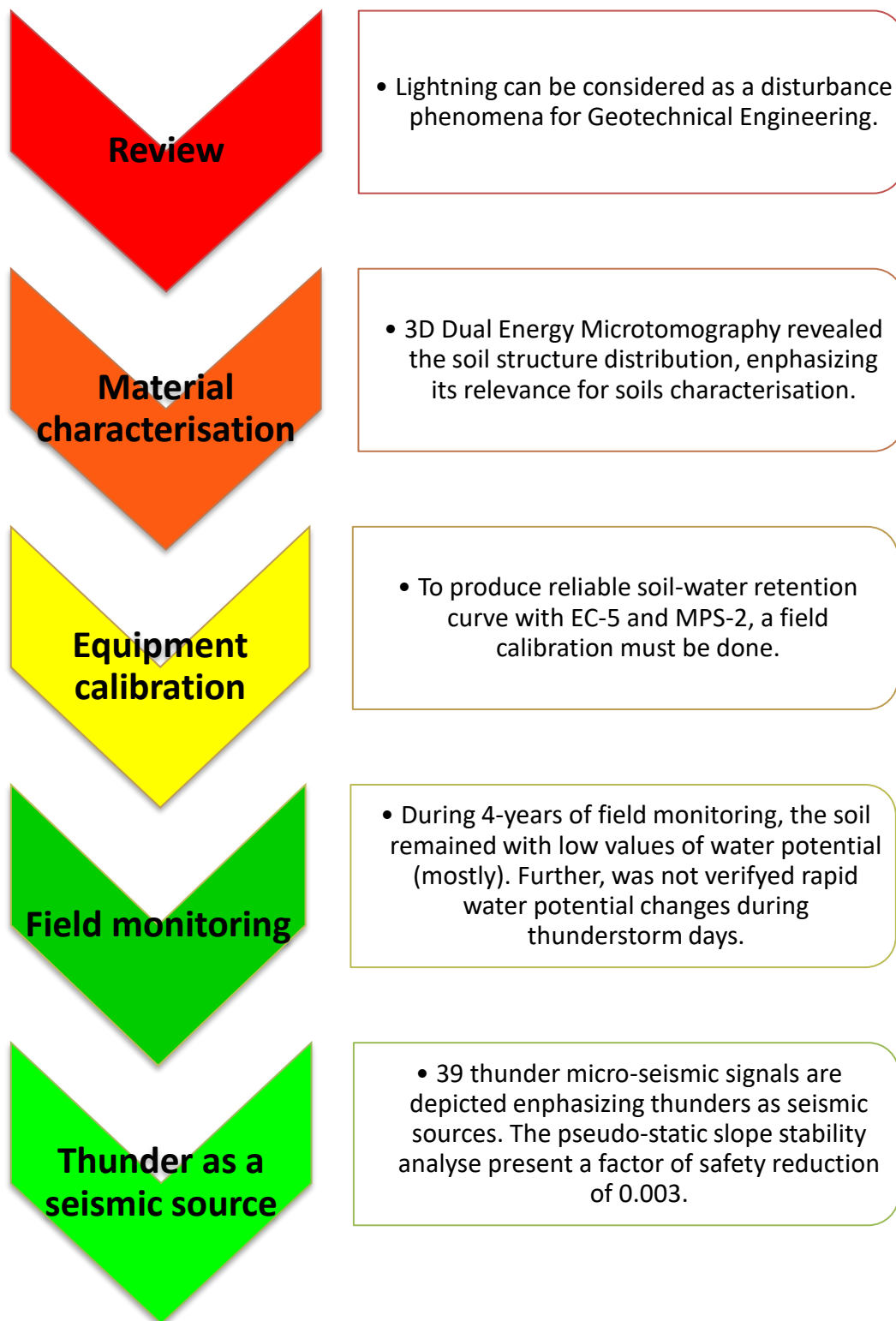


Figure 0.1 - Thesis' organisation

Table 0.1 - Chapter 2 organisation

Chapter 2
Lightning: A review on its formation and its potential effects on soils slope stability.
Context
<ul style="list-style-type: none"> • Around hundred thousand lightning occurs worldwide, and although this phenomenon has been widely studied by the physical and meteorological areas, researches concerning lightning influences into the soils physic-mechanic behaviour were never compiled until now.
Introduction
<ul style="list-style-type: none"> • Motivation - Disaster on the Mountainous Region of Rio de Janeiro.
Lightning
<ul style="list-style-type: none"> • Lightning-soil interaction - bibliographic survey. • Electrical effects. • Effective shear strength parameters reduction of the soil struck by simulated lightning. • Unconfined compressive strength tests on samples struck by replicated lightning.
Thunder
<ul style="list-style-type: none"> • Thunder-soil interaction - bibliographic survey. • Seismic previous characteristics. • Rapid pressure changes. • Simulated thunders and tensiometer response.
Conclusion
<ul style="list-style-type: none"> • Lightning is not a punctual phenomenon. • The atmospheric electrical discharge has different phases that release energy in a short time interval. • Concerning electrical incidence, it is evident that heated channels and soil interaction are relevant subjects for future studies about soil mechanical behaviour and soil mineralogy changes. • Thunder can be analysed by acoustic and seismic ways. • Lightning (flash and thunder) are disturbing agents of the physical environment and it can be an important subject for soil mechanics.

Table 0.2 - Chapter 3 organisation

Chapter 3
Using 3D microtomography for soil characterization.
Context
<ul style="list-style-type: none"> In the light of geotechnical studies, the necessity to improve and complement soil characterization data in order to observe the mineral and void distribution of undisturbed soil samples is remarkable.
Introduction
<ul style="list-style-type: none"> The use of microtomography for geotechnical and earth sciences purposes is related to the comprehension of the materials, once the soil structure may still contain characteristics of the origin's material and/or information on pre-existent geomorphological processes. Bibliographic review (3D Microtomography). Description of Dual Energy microtomography.
Regular Characterization (standard)
<ul style="list-style-type: none"> Physical Index. Grain Size Distribution. Atterberg Limits. Mineralogical characterization. X-ray diffraction and Differential Thermal Analyse. Soil Water Retention Curve. Mercury Injection Porosimetry. Scanning Electron Microscopy / Energy Dispersive Spectroscopy.
μ CT
<ul style="list-style-type: none"> Image rendering. Quantitative data. Voids distribution. Porosity. Qualitative approach. Dual Energy Results - Iron Oxide distribution.
Conclusion
<ul style="list-style-type: none"> Tomography can be a relevant approach to analyse the soil's internal structure. It can distinguish the open and closed pores. Iron oxide and quartz can be identified. The microtomography confirms the microscopy. The microtomography cannot be performed for determining all soil characterization parameters such as porosity. The equipment resolution only reveals information on macro pores.

Table 0.3 - Chapter 4 organisation

Chapter 4
A correlation between laboratory and field monitoring data: Testing different installation procedures to produce a reliable Soil Water Retention Curve (SWRC) during field monitoring.
Context
<ul style="list-style-type: none"> Real-time data acquisition is extremely important to predict and solve problems. In terms of geotechnical issues such as landslides, recovery of degraded areas and disasters management, the volumetric water content (VWC) and the matric potential (MP) determination reveals remarkable information concerning the transient features of soil-weather interaction.
Introduction
<ul style="list-style-type: none"> Li <i>et al.</i> (2005), pointed out that the field SWRC "<i>matches well with the wetting portion of the laboratory SWRC</i>", however, wetting and drying cycles in the field present significant differences from the drying portion of the laboratory curve. Ng and Pang, (2000) emphasized a slight air-entry value for natural samples, pointing out a pore-size distribution dependence. The analysis of capacitance/permittivity highlights that the volumetric water content variations lead to variations of the dielectric constant of the soil in which the probe is inserted.
Lab. Procedures
<ul style="list-style-type: none"> The methodology consists in testing the influence of variation of bulk density in volumetric water content measured values. Proctor vs. hydraulic compactions were compared. A laboratory drying SWRC – Frequency Domain Reflectometry EC-5 and Water Potential MPS-2 range test was performed.
Field Calibration
<ul style="list-style-type: none"> Volumetric ring - SWRC field calibration. Probe's installation testing procedures. 3D microtomography to evaluate the contact between EC-5, MPS-2 and the soil.
Conclusion
<ul style="list-style-type: none"> The EC-5 sensor is extremely sensitive to installation techniques, requiring field calibration for different techniques in each installation point. The drive-in installation technique is recommended because it presents a better correlation with the filter paper method. The 3D microtomography depicted structural changes for the rod (auger) technique and the mud injection installation methods.

Table 0.4 Chapter 5 organisation

Chapter 5
Soil-atmosphere interactions: Using field monitoring to evaluate matric suction transient features.
Context
<ul style="list-style-type: none"> • Soil-atmosphere interactions can reveal important transient conditions and even mechanical behaviour. • Many papers have associated landslide occurrences to rainfall/water influence (e.g., Vargas, 1971; Lumb, 1975; Brand, 1984; Gerscovich <i>et al.</i> 2006), and to soil suction variations (Lim & Rahardjo, 1994; Faisal, 2000; Toll <i>et al.</i>, 2011; Blight, 2013; Springman <i>et al.</i>, 2013). • However, rapid changes in soil saturation are still unrevealed.
Main Goals
<ul style="list-style-type: none"> • Evaluate possible rapid variation of water potential of the soil in comparison with atmospheric parameters variations. • Analyse the lower saturation degree periods. • Verify the depth of the meteorological daily-influence on the soil. • Analyse the soil behaviour during thunderstorm days.
Field Monitoring
<ul style="list-style-type: none"> • Long-term field monitoring of matric potential variations by using MPS-2 probes and a Campbell Water Station. • Satellite lightning detection network was used to monitor the electric discharges in the atmosphere.
Conclusion
<ul style="list-style-type: none"> • The scale effects are a problem for field monitoring. • The soil remained with low water potential condition for a longer period. • Lower matric potential values were observed only in dry periods of the year. • When considering thunderstorm and lightning events, no correlation was observed between atmospheric discharges and water potential variations.

Table 0.5 - Chapter 6 organisation

Chapter 6
Thunder: A micro-seismic atmospheric source.
Context
<ul style="list-style-type: none"> • Thunders are not treated in the light of geotechnical researches as a dynamic loading.
Main Goals
<ul style="list-style-type: none"> • To analyse the thunder occurrences and its micro-seismic characteristics, pointing out its influence in a pseudostatic slope stability analyse.
Lightning Detection System (Field Monitoring)
<ul style="list-style-type: none"> • The lightning spatial distribution was obtained by a satellite monitoring program (STARNET system), depicting 39 occurrences, in a radial 10 km distribution area. • A seismographic field monitoring was performed, using the Kinematics Quanterra STS-2 equipment, installed on a concrete pile, 1 meter under the soil surface, connected in a datalogger Quanterra Q330 and Baller P44.
Slope Stability
<ul style="list-style-type: none"> • The SVSLOPE was used to perform a pseudostatic stability analyse, using the seismic horizontal coefficient k_h based in the measured horizontal component accelerations in thunderstorm days.
Conclusion
<ul style="list-style-type: none"> • The results emphasized that the observed lightning induced accelerations up to 0.02 m/s^2, highlighting a power frequency spectrum up to 80 Hz. • Thunders can be considered a seismic source. • The results showed the seismic horizontal coefficient induced by thunders are lowers than Yields coefficients (the horizontal coefficient (k_h) when factor of safety reaches 1). • However, it is important to emphasize that nearer phenomena can produce higher accelerations and then higher horizontal seismic coefficient values.

2

Lightning: A review of its formation and its potential effects on soils and slope stability

Abstract

Annually, around a hundred thousand lightning occurs worldwide. Although this phenomenon has been widely studied in the physical and meteorological areas, researches concerning lightning's influences on soils and slope stability has not been of much attention so far in the geotechnical and environmental engineering areas. As an attempt to evaluate that, this Chapter depicts the main features of the lightning global incidence, pointing out researches that correlate the occurrence of lightnings to soils and slope stability. In addition, some geotechnical peculiarities have been briefly discussed in the light of researches developed at PUC-Rio, in which the atmospheric electrical pulse incidence and the effect of pressure variation have been brought up. This paper also depicts lightning as a potential agent for geotechnical occurrences, suggesting that the phenomenon should be considered and studied by different areas of geotechnical engineering. It concludes that potential effects of dynamic events must be further investigated to provide better understand of failure mechanisms of soils during thunderstorms.

Impact factor: Lightning can be considered as a potential trigger agent for landslides.

Keywords: Lightning, lightning-soil interaction, thunder pressure.

2.1.

Motivation - 2011 Disaster on the Mountainous Region of Rio de Janeiro

In January 2011, the state of Rio de Janeiro, Brazil, suffered what was considered as the worst natural disaster in its history. At that time, thousands of landslides of differing types and proportions (Figure 2.1) occurred in the mountainous region under heavy rainfalls, claiming more than 900 casualties and leading to a loss of millions of dollars.



Figure 2.1 - Landslides in the mountainous region of Rio de Janeiro. (Photo taken by F. Dourado on January 13th, 2011)

Although the major influence of water to the stability of those natural slopes has been fully recognised, the identification of the ultimate factor, responsible for a mass movement, was not depicted for all landslides, suggesting that something else may have acted as a potential trigger.

This fact is supported considering that both shallow and deep landslides occurred, comprising both mature and residual soils at approximately the same time in the whole area. Indeed, witnesses of the events reported that (de Campos *et al*, 2018):

- “Winds were not abnormal. Indeed, they were almost absent”.

As winds were not a factor, this information indicated that the occurrence of an atmospheric phenomena such as anti-cyclone (e.g., Nimer, 1979) could be disregarded.

- *“It was like a water bucket pouring water continuously onto our heads for 15 to 20 minutes”.*

Fairly long, high intensity rainfall would not promote, by itself, any further infiltration into the soil profiles prevailing in the region, which were probably already saturated at their surface due to previous rainfall conditions. Nonetheless, it could provide the occurrence of important erosion processes that could, on the other hand, promote initialization of slope failures by erosion at the slope toe or propitiate the exposure of unsaturated material along the slope to further rainwater infiltration, leading to failures due to further loss of suction. In view of the generalized and, as reported, nearly simultaneously occurring landslides, such assumption could only be taken into consideration if unprecedented rainfall would have happened. This, however, does not look as have been the case, as reported by Coelho Netto *et al.* (2011) and Medeiros & de Barros (2011). These authors concluded that although the rainfall event was exceptional, it could not be considered as unprecedented. Furthermore, Entralgo (2013) presented evidences that the locus of the highest rainfall intensity did not fully coincide with the location of the scars of the main landslides in the site as a whole.

- *“Everything was shacking”.*

It was considered that shacking could have been due to: occurrence of a relevant seismic event, impact of nearby large soil masses failing at the same time, and/or propagation of sound waves associated to atmospheric events. As earthquakes in Brazil have not been considered, so far, as relevant in processes of instabilization of natural slopes, seismic effects were preliminary disregarded. Supporting that, no registration of quakes in the region was found in the data provided by the seismological stations from the Brazilian network. Shacking promoted by the impact of nearby soils mass was disregarded due to the distribution of the events. Thus, propagation of sound waves could be relevant.

- *“It was a thunder storm, with abnormal lightning”.*

Only rainfall conditions had previously been considered as a contributing atmospheric factor to the onset of landslides in Rio de Janeiro. Thus, such information, associated to the above one, called attention and led to investigations

looking at the potential occurrence of failure mechanisms, not previously considered, associated to thunder storms and lightning.

In addition, the mountainous region of Rio de Janeiro has shown an increase in the average number of atmospheric discharges per unit area (Table 2.1 - ELAT, 2013).

Table 2.1 - General statistical data – Incidence of lightning in the cities of the mountainous region of Rio de Janeiro (ELAT (2010); ELAT (2013))

Municipality (RJ)	Area	Population (censo 2000)	2005-2006	2007-2008	2009-2010	in 2013
			Density lightning / km ² . year	Density lightning / km ² . year	Density lightning / km ² . year	Lightning Dens / km ² . year
Areal	112.35	11.421	2.8223	3.031	5.044	8.75
Bom Jardim	386.52	37.828	2.209	2.3395	3.3395	11.69
Cachoeiras de Macacu	956	54.370	3.0425	4.6363	10.1118	12.6
Cantagalo	752.32	19.826	1.8439	2.0387	4.1131	9.71
Cordeiro	115.63	20.403	2.3727	2.1937	3.6562	11.07
Duas Barras	376.86	10.933	2.094	2.5438	3.9622	10.79
Nova Friburgo	933.33	182.082	2.644	2.4227	2.9901	12.12
Petrópolis	794.84	296.044	2.1637	2.774	3.8223	10.01
Santa Maria Madalena	816	10.321	1.4787	1.8896	3.1222	9.02
Santo Antônio de Pádua	612	40.569	2.0175	1.8184	5.6779	10.02
São Fidélis	1.028	37.553	1.9317	1.6794	3.3768	6.96
S. J. do Vale do Rio Preto	220.83	20.252	1.9838	2.4773	3.4217	10.39
Sumidouro	396.24	14.920	1.8572	2.4293	3.5698	11.27
Teresópolis	772.6	163.805	1.669	2.4425	2.6185	10.45
Trajano de Moraes	589	10.281	1.6344	1.6897	2.9059	9.75
Rio de Janeiro	1.182	6.323.037	2.2403	1.8531	5.7216	6.43

In an attempt to investigate the lightning influences, an ancient question had come up: Is it possible that atmospheric discharges have contributed to trigger those landslides?

Concerning the possible answers to this question, lightnings (rays) are a phenomenon that reaches temperatures close to 30.000 °C (Uman. 1964) in a short time interval (up to microseconds). The high temperature disposed in the luminous path, responsible to increase the pressure, is dampened in accordance with the radial distance as such: 8 atm for 5 μ s. in the zone of contact with the

luminous path (Orville. 1968c); 2 atm to 35 cm from the luminous path (Newman *et al.* 1967a and b); and 10⁻⁴ atm for 1 km distance (Few. 1970).

In this way, in the light of the geotechnical approach, preliminary tests were performed to evaluate flash (electrical) and thunder (sound pressure).

2.2. Lightning

In the 90's, the global lightning distribution remained unknown, with only a part of the earth covered by worldwide detection networks (Orville. 1995). Nowadays, satellites placed in low orbit are used to measure lightning over the intertropical area of the globe, and the use of this equipment, mainly used by NASA, highlights a strong incidence of lightnings on: Asia (in the mountainous area), Central Africa, South and Southeast of United States, and South and Southeast regions of South America.

The atmospheric discharges are of great interest to many scientific and industrial areas because the phenomenon causes hundreds of deaths per year, immeasurable injuries to the biodiversity (through fires in forests and agricultural areas), and thousands of dollars are lost due to the damage to the electric power utilities, by interruptions or damage in electrical or electronic system exposed to thunderstorms.

The electric discharge is performed by the concentration of charges over the air motion and its grounding performs through the lower resistance air path. The luminous channel reveals the route in which the air is used as a dielectric, transferring energy from the clouds to the ground or from the ground to the clouds. It happens because *“the atmosphere below about 50 km is conducting, owing to the presence of ions created by cosmic rays and the natural radioactivity of the Earth. In lower atmospheric levels, the average production rate of ions (at sea level) is one to 10 million pairs per cubic meter per second”* (Rakov & Uman. 2003).

About the luminous path, also named main heated channel, it may have multiple branches and it can reach nearby areas. This fact makes it possible to challenge the hypothesis that atmospheric discharges are a punctual phenomenon

for soil, requiring kilometres of distance for another lightning occurrence. In addition, researches such as that developed by the INPE's atmospheric discharge detection network and the STARNET network (associated to the São Paulo State University) has revealed a hundred of rays' incidence in a short period.

2.3. Lightning-soil interaction

Regarding lightning occurrence, Gomes (2002) developed a pioneer study that correlates the incidence of atmospheric discharges with altitude and different soil types from Minas Gerais, Brazil. At that time, it was emphasized that a lightning's incidence increases with the altitude increase and there's a high correlation of the total number of atmospheric discharges with oxisols - Aquox (LFE – Figure 2.2). In addition, Bourscheidt (2008) correlated the occurrences of atmospheric discharges with the relief and soil surface temperature, pointing out that steep slopes are responsible for increasing the incidence of lightning in specific regions, indicating a linear lightning occurrence increasement due to the temperature increase.

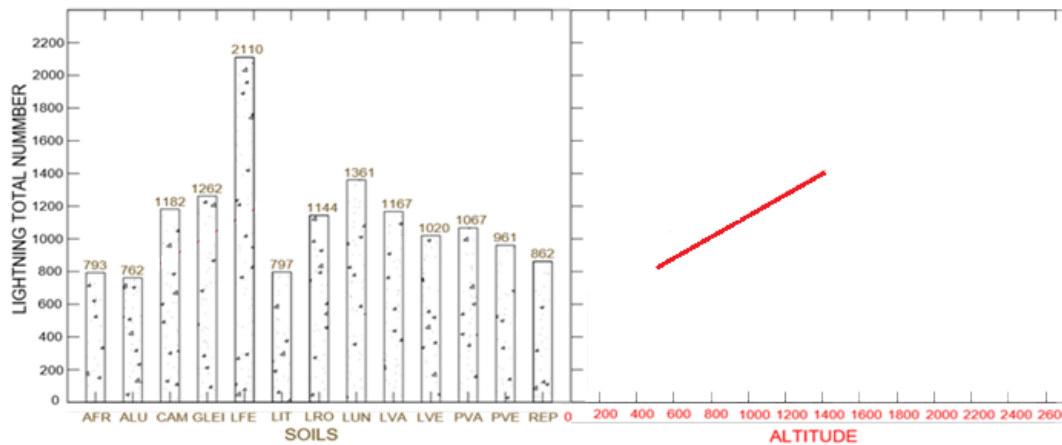


Figure 2.2 - Relation between the total number of rays and the types of Brazilian soils (hatched bars). Red line represents the distribution of lightning with the altitude increase (ruled by red horizontal superior axis). Adapted from Gomes (2002). (AFR) Rocky outcrop; (ALU) Alluvial soil; (CAM) Cambissol; (GLEI) Gleí humic soil; (LFE) Iron latosol; (LIT) Litosol; (LRO) Purple latosol; (LUN) Una latossol; (LVA) Red-yellow latossol. (LVE) Dark-red latossol; (PVA) Red-yellow podzolic soil; (PVE) Dark-red podzolic soil; (REP) Reservoir soil

2.4. Electrical influences

To evaluate the electric influences from lightnings into the soil, Carnavale *et al.* (2015) performed an experimental procedure comprised by high-voltage setup (Figure 2.3), constituted by seven spherical charging steps, manufactured by HIGHVOLT and disposed at Cepel - Electrical Energy Research Centre - Brazil.

The method was constituted by subsection of undisturbed and reconstituted samples, with 38 mm of diameter and 76 mm in height, of a residual granite-gneiss soil, to electric pulses (300 kV, 450 kV and 600 kV).

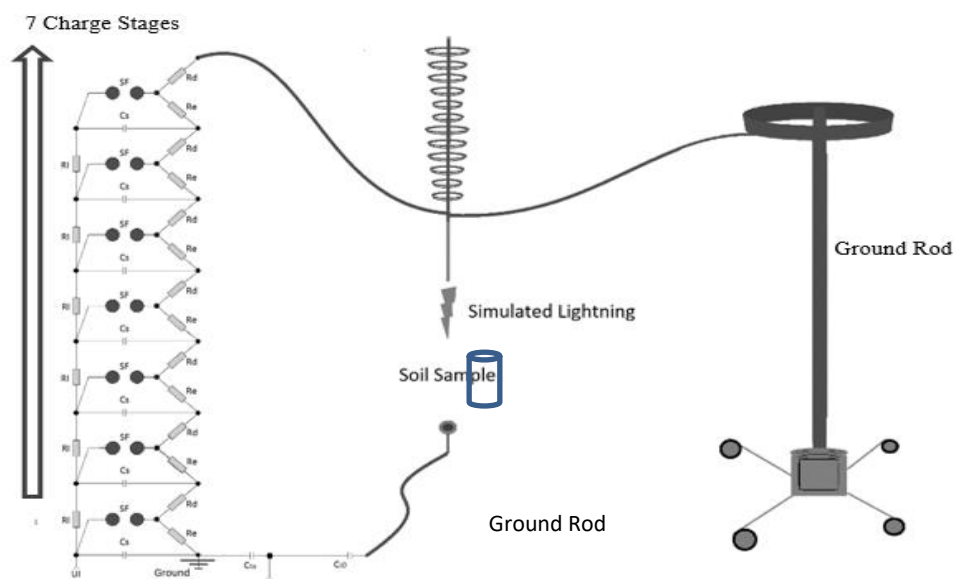


Figure 2.3 - Highvolt pulse generator. (SF) Spherical charging steps. (Rd, Re and Rs) Resistive components. (Cs) Charging capacitive redemption components

Concerning simulated lightning formation, the heated luminous channel is formed if the electrical signal is higher than the air resistance, discharging the electric pulse in the ground rod. At this time, it is possible to observe the replicated lightning and the consequence of the impact in the sample struck by the phenomenon (Figure 2.4).

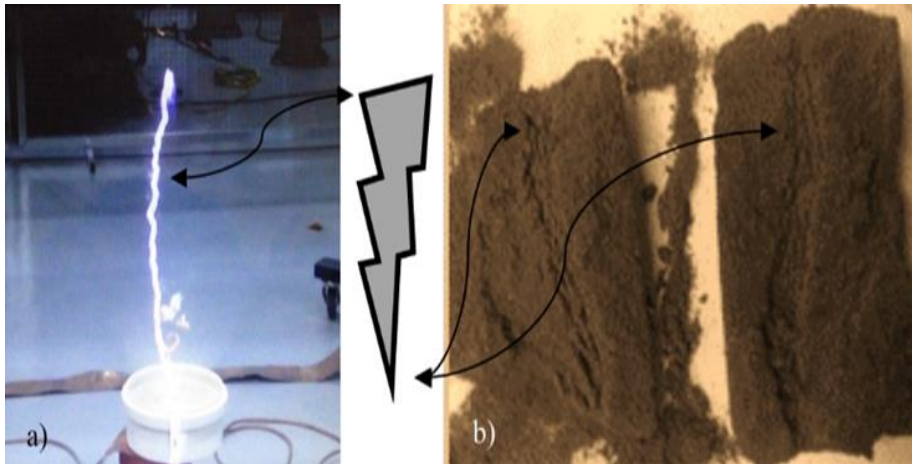


Figure 2.4 - Simulated lightning developed in the lab and borehole caused in the soil

During the use of the microtomography technical approach it was observed that the electric discharge affects the structure of the samples struck only with 450 kV and 600 kV. The simulated lightning caused an irregular tortuous hole with some radial cracks, using the central area of the sample as the principal path (Figure 2.5).

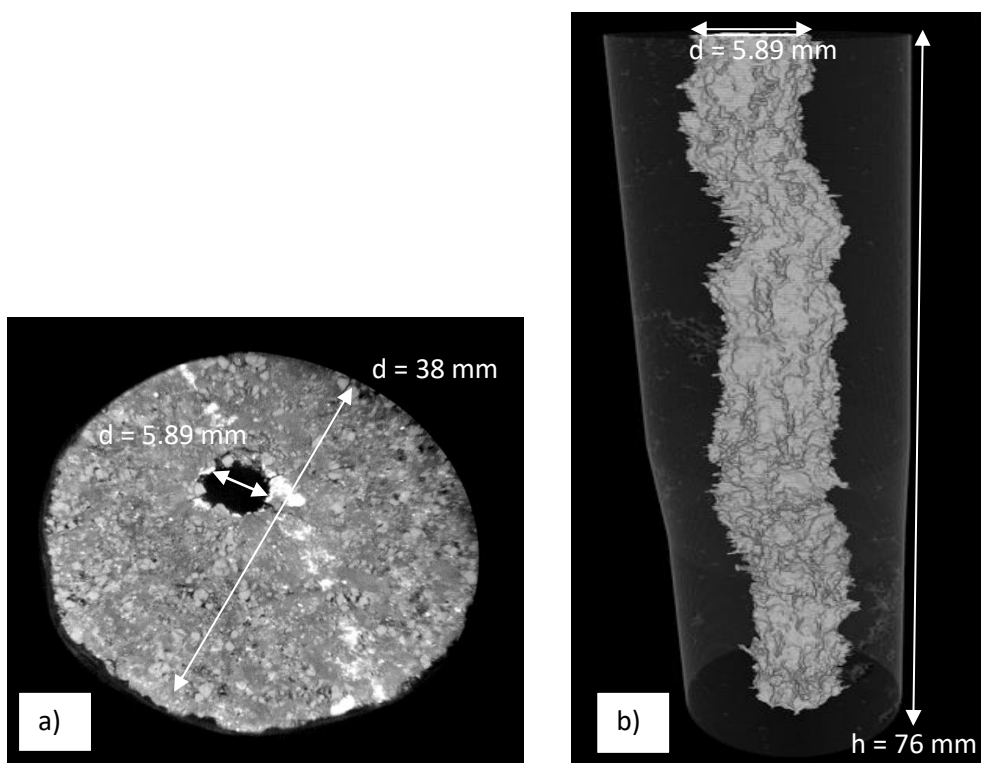


Figure 2.5 - Microtomography. Top (a) and central hole (b) images

For the 600-kV sample, the hole size distribution was analysed, and it was possible to observe a higher hole size near the sample bottom, with maximum 6 mm of diameter. Another observation refers to the spiral behaviour: apparently, the simulated lightning crossed the soil sample through a zig-zag path.

An additional information obtained by this procedure refers to the absence of soil mineralogy alteration. Even the borehole walls presenting a “burnt path”, the equipment could not reach high temperatures in a short time. In this way, for mineral alteration and an eventual fulgurite composition such as disposed in the Figure 2.6, higher temperatures must be reached.



Figure 2.6 - A Florida fulgurite of about 5 m length excavated by the University of Florida lightning research group (Rakov & Uman, 2003)

In the light of simulation, the research emphasized the induced electric discharges must be considered a replicated lightning, since they are respecting with the time to reach the peak of voltage ($1.2 \mu\text{s}$) and tail ($50 \mu\text{s}$) values (ABNT NBR 5418 / 1995).

Confirming the signal characteristic, Figure 2.7 shows the technical response emitted by the equipment, presenting kV (voltage) for channel 1 and A (amperage), for channel 2. Further, the data sheet reveals that the amperage did not increase such as the voltage (peak value remained around 10 A). In addition, it also pointed out the negative characteristic of the charge, which represent a negative, downward lightning, considered the most common for soil incidence in the world (Rakov & Uman. 2003).

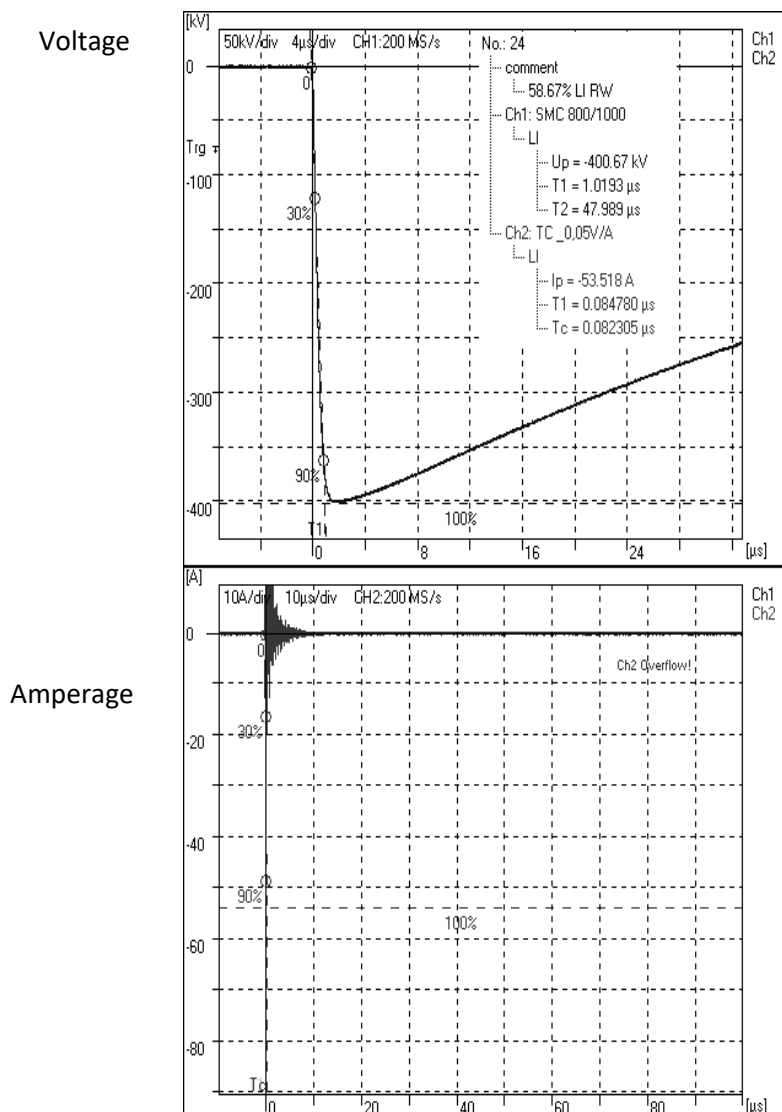


Figure 2.7 - Simulated lightning developed in the lab

In the light of mechanical response, on the same set of samples subjected to the simulated lightning, Carnavale *et al.* (2015) performed a consolidated and drained triaxial tests (with 50 kPa, 100 kPa, and 150 kPa of confining stresses) and the results are shown in Table 2.2. It shows that simulated lightning promoted a decrease in the cohesion intercept to zero and a decrease in the friction angle of circa 7%.

Table 2.2 - Effective shear strength parameters of the soil struck and non-struck by simulated lightning (Carnavale *et al.* 2015)

Soil Condition	c' (kPa)*	ϕ' (degree)
Samples not struck by simulated lightning	4.6	28
Sample struck by simulated lightning	0	26

Concerning the electrical incidence and soil-disturbance correlation, Carnavale *et al.* (2016) reported unconfined compressive strength tests results for specimens struck by simulated lightning under three different electric loads (300 kV, 450 kV, and 600 kV).

The research emphasized that the method must be changed due saturated samples performed explosive ruptures when submitted to replicated lightning, causing the entire sample destruction. Regarding this, the research is comprised by tests in samples with the same moisture contents, just changing the simulated lightning power-energy, revealing a peak resistance reduction with the energy incensement.

The Figure 2.8 shows the effects of the water content of the unsaturated soil samples, comparing them with strength results, obtained for samples non-struck by simulated lightning. In addition, is plotted in this figure the values for the samples hit by simulated lightnings with different charges, emphasizing this samples are comprised by the natural moisture content.

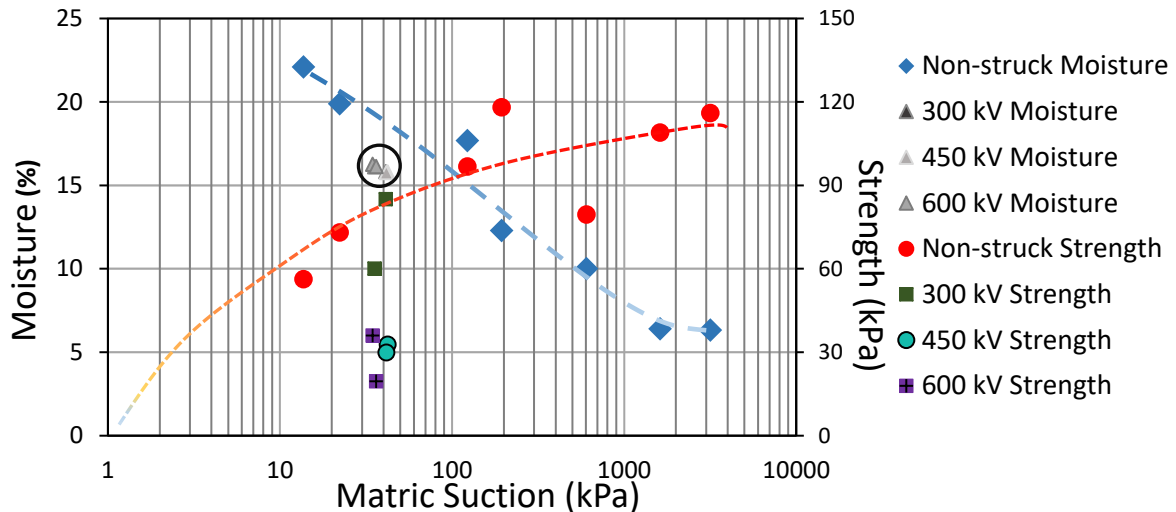


Figure 2.8 - Unconfined strength tests for the samples struck and non-struck by replicated lightning versus moisture content and matric suction

Finally, it is suggested that the effects of non-saturation must be considered in the analysis of possible interactions between lightning and soils, as different moisture contents provide different structural changes in samples of the same type of soil.

2.5.

Thunder – Formation, pressure and seismic

Regarding the acoustic waves (thunder sound), it is emphasized that it is not possible to dissociate this phenomenon from the flashes because the heated channels and their pressure signatures are strongly connected (Roy & Ribner, 1984). Moreover, the thunders' influence area is higher than that of the flashes, a thunder can be heard up to 25 km distances, suffering damping/attenuation depending on the geometry of its propagation site (Bass, 1980).

The thunder sound formation is a consequence of the multiple points of explosion, arranged in one or multiple irregular lines (Ribner *et al.* 1975). They have distinct propagations in time and space, providing a unique pressure signature based in the ray's geometry (Lee, 2009).

A simplified model is presented by Ribner *et al.* (1975). At that time, it was postulated that spherical waves are emitted simultaneously by each point of explosion of a ray, that such waves propagate independently, and the sound heard

at any distance is made by a range of pressures that reach the point of hearing simultaneously (Figure 2.9).

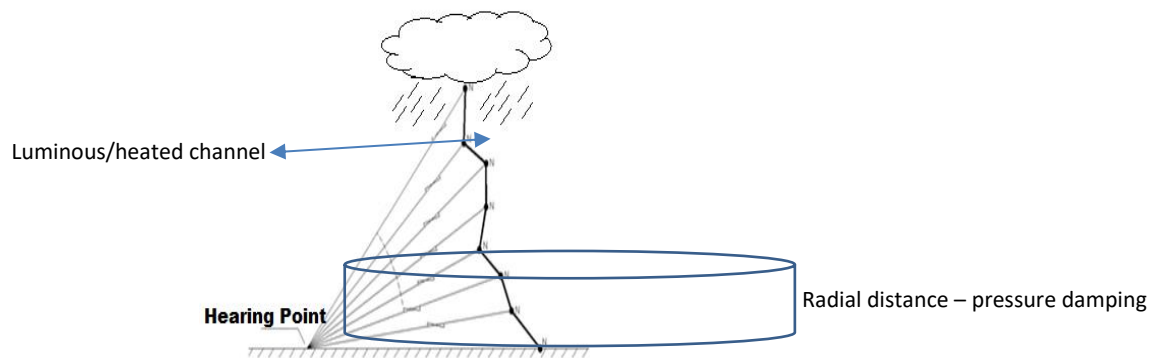


Figure 2.9 - Thunder sound formation scheme - ignoring refraction effects (from Ribner *et al.* 1975)

According to Ribner *et al.* (1975), even though visually it seems that the rays are not straight, and the wave fronts are not spherical due to refraction by temperature gradients (mainly) and air motion in the atmosphere. The rays are curved and usually concave upwards. It has the additional effect, as shown in figure 2.10, of “producing a cut-off due to refraction where the sound from the lower part of the radius cannot reach the observer, suggesting that the acoustic pressure does not increase with the heated channel proximity and that the conversion of the shock waves to acoustic waves governs the possible pressure variations in that area”.

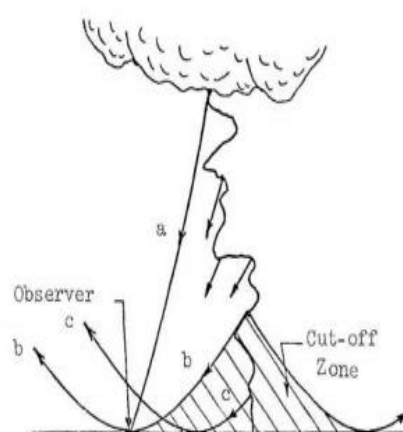


Figure 2.10 - Refraction cut-off. Effects of curved atmospheric temperature variations on the sound rays causing the observer to hear only the rays that are between points a and b (from Ribner *et al.* 1975)

It is important to emphasize that even if the simplifications are not totally faithful to reality, they are necessary for the simulations and analyses of thunder. Concerning this, the curved rays are simplified by rectilinear elements, and a 2D framework instead of 3D is also assumed (Wright & Medendorp, 1967; Ribner *et al.*, 1975; Ribner & Roy, 1982; Lee, 2009; Glassner's, 2010).

In relation to channel geometry replication, Rakov and Uman (2003) highlighted five Few's theory points (one of the first to be accepted scientifically) on the processes of thunder's constitution: energy balance - sound-radiating-channel length - transformations of the shock waves - formation of N-shaped pressure pulse and - power spectrum of thunder.

Regarding the energy balance, all incoming electrical energy (which is arranged in a unit of specific length of one of the segments of the heated channel) are delivered to the shock wave depending on the thermodynamic operation of the atmosphere within a radiated distance, which is called relaxation radiation.

Concerning the emitted pressure and the sound of thunder, the phenomenon is related to the process of transformation of the shock waves into acoustic waves and the pressure is normalized as a function of the radial distance, i.e., normalized to the radius of relaxation.

The signal pressure is emanated from each point along each ray segment, ranging from a few hertz or less to a few kilohertz. It is audible when they are between 20 Hz and 20 kHz, i.e. the human hearing range.

Pointing out shock-acoustic transforming, Few (1969 b) emphasized that the “shock wave diverges cylindrically during the thermodynamic work stage, and after this stage, it makes the transition to spherical divergence. Thus, at the end of the thermodynamic working stage, each section of the heated channel can be replaced by a volume of hot air resulting from a shock wave, producing acoustical waves”.

According to Few *et al.* (1967), the distance in which the transition from the shock wave to the acoustic wave occurs is probably from 11 to 89 cm, for an input energy of 10^3 to 10^4 J m⁻¹ and, from 1.1 to 8-9 m, for an input power of 10^5

to 10^6 J m^{-1} . Such a transition occurs during the thermodynamic work routines, as the gas forces the pressure in the channel axis to decrease to a value lower than the ambient temperature, creating a kink related to the N-wave and the thunder sound.

Thunders is a phenomenon that can be explored by the air pressure approach. This occurs because Rakov and Uman (2003), presented an increase of 0.3 to 2 atm for 10 to 35 cm of luminous channel, and Orville (1968 c), presented a 10 atm increase of pressure in the heated channel during the first $0.5 \mu\text{s}$.

In this way, considering pressure variations, Carnavale *et al.* (2014) sought to analyse the variations in matric suction during the simulated thunder sound pressure incidence in a granite-gneiss soil from Nova Friburgo, Rio de Janeiro, Brazil.

For the tests (Figure 2.11 a and b), the confined and unconfined blocks (saturated by Mariotte bottle and direct wetting), were arranged in a chamber with thermo-acoustic treatment, and 6 thunder sound waves emission were triggered, crosschecking the sound pressures with suction responses (UMS - tensiometers T5X).

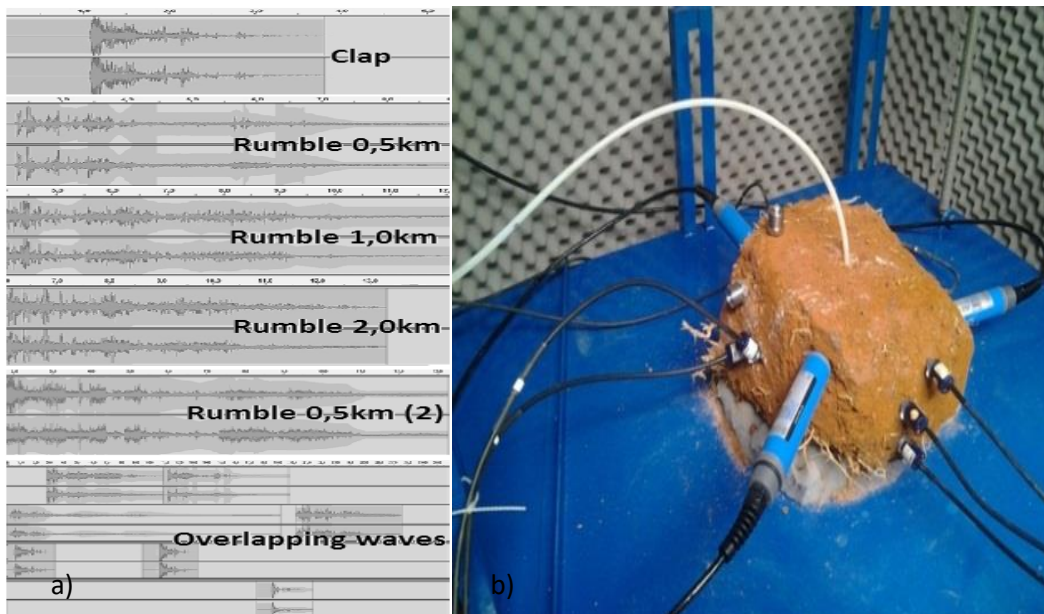


Figure 2.11 - a) Replicated thunder sound. b) Test setup

As a result, the occurrence of variations in suction up to 0.4 kPa (Figure 2.12) and a failure of a soil block from one of the areas affected by the disaster in the Mountainous Region of Rio de Janeiro State was induced.

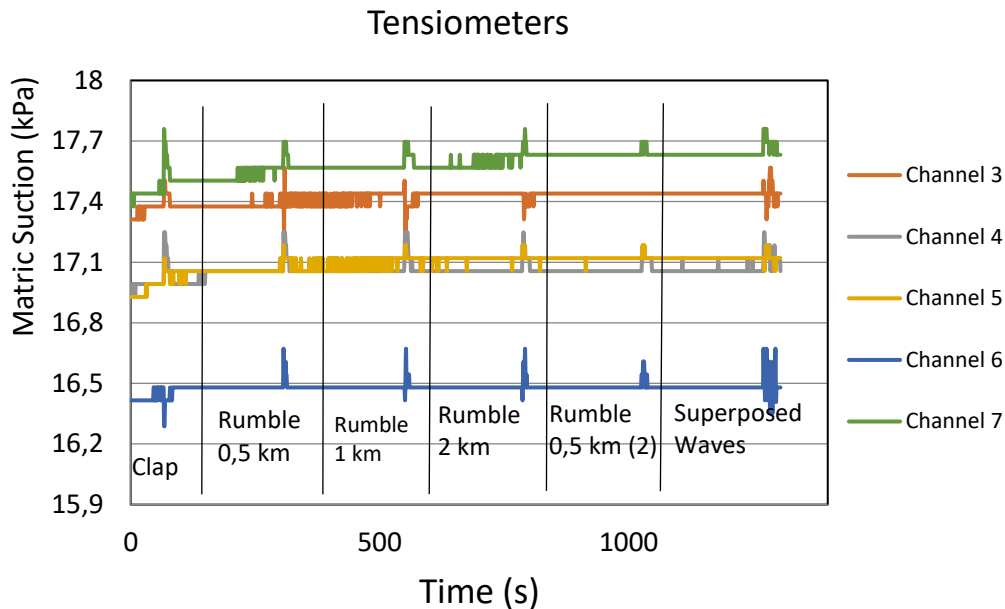


Figure 2.12 – Matric suction (T5X) versus simulated thunders

In the light of thunder acceleration and its correlations with dynamic of soils or any geotechnical approach, there are relevant aspects that can be used by geotechnical engineers.

Balachandran (1979) presented a study about infrasonic waves during thunderstorms, presenting a 10 μ Bar maximum peak-to-peak pressure, emphasizing that sound pressure signature has good correlations with shock waves forms, suggesting that the pressure propagates with a similar signature of the shock wave.

Kappus and Vernon (1991) performed readings of three uniaxial seismic sensors and the results revealed that the seismic records are faithful to the acoustic thunder signal in the air. However, “no attempt was made to quantify amplitude reduction via transmission across the interface or ground attenuation”. Furthermore, the obtained data depicts peaks at low frequencies varying from 6 to 13 Hz in the ground.

Lin and Langston (2007) considered thunder infrasound as a natural seismic source. In an experimental research, they used 3-component seismological sensors and infrasound microphones to perform the record. In that case, it was observed that thunder occurrence caused P and S waves near the surface and the radial component “decays as much as 63 percent with depth but vertical component amplitudes are unaffected, consistent with air-coupled Rayleigh wave excitation” (Lin & Langston. 2007). Additionally, peak-to-peak pressure of 0.18 and 0.13 Pa in the analysed events was obtained.

Concerning the main results, it was revealed that ground velocity was different comparing vertical and radial components. It can be explained by vertical air-coupling and its compressional pattern that causes different responses in terms of velocity particle motion (Figure 2.13).

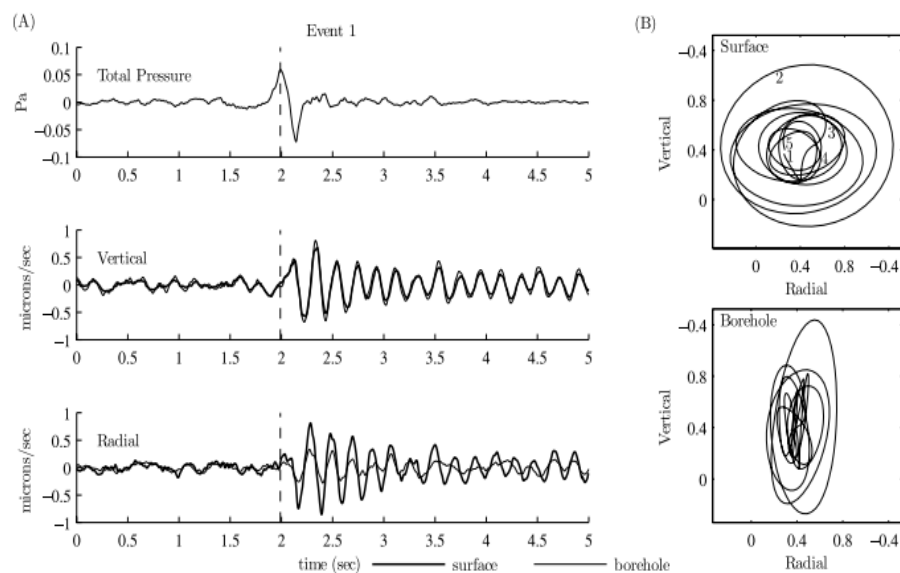


Figure 2.13 - (a) Event 1 total pressure and ground velocity recorded by the array. (b) Velocity particle motion for surface and borehole sensors for event 1. The numbers (1 – 5) in the particle-motion plot represent the time sequence from 1 (initial) to 5 (end), (Lin & Langston. 2007)

In a similar perspective, Voss *et al.* (2015) developed a research that introduced a network with 6 seismic stations, of over 5 km of radius, with the aim to detect thunder signals that are normally regarded as noise. The thunders observed occurred up to 30 km from a seismic station, presenting seven waveforms (Figure 2.14).

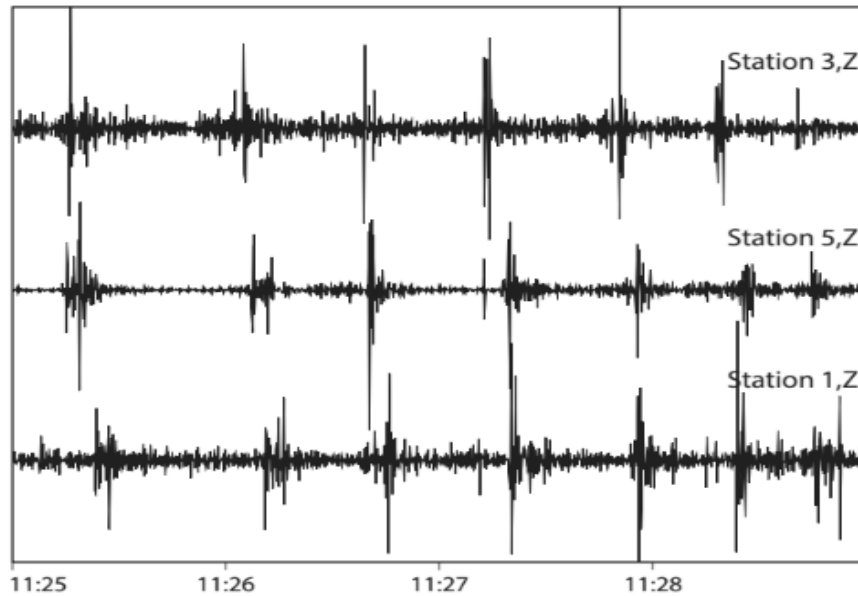


Figure 2.14 - Seismogram obtained during a thunderstorm (Voss *et al.*, 2015)

2.6.

Conclusion

Lightnings are not a punctual phenomenon, and its occurrence is increasing in many places such as the mountainous region of Rio de Janeiro. The atmospheric electrical discharge has different phases that release energy in short time intervals.

Taking into consideration atmospheric effects (other than just rainfall), preliminary results of researches being developed at PUC-Rio were also put forward, emphasizing that a sudden increase in atmospheric pressure may promote a decrease in both strength and stiffness of the unsaturated soil.

Concerning electric incidence, it is evident that heated channels and soil interaction are relevant subjects for future studies about mechanical behaviour and mineralogy alterations.

The analysis of this paper emphasizes that thunder can be analysed by acoustic and seismic ways in an acoustic-seismic coupling perspective. Its methods have a good ratio, and its seismic responses can be applied to earthquake analysis because it is related to a near-surface structures.

Still regarding the vibrations caused by thunders, the presented researches did not correlate the time occurrence or the incidence area of lightnings with the power energy measured into the soils. Even confirming the results based on the waveforms theory and acceleration characteristics, there is a gap related to the distance of occurrence and its superficial propagation into the soil to be understood.

In conclusion, it was depicted that lightning (electric rays and thunders pressure increase and vibrations) are agents that can promote physic-mechanics alterations in soils, confirming the subject as a relevant phenomenon for geotechnical engineering.

3

Using 3D microtomography for soil characterisation

Abstract

In the light of geotechnical studies, the necessity to improve and complement soil characterisation data in order to observe the mineral and void distribution of soil samples is remarkable. Regarding this, this research aims: to apply 3D microtomography (μ CT) and evaluate its potential use to understand the internal structure of soil; to quantify the opened and closed voids to obtain the macro porosity; to analyse the quartz and oxide distribution in the soil sample. To perform this study, a colluvial soil from the coordinates 663961E/7500946N, mainly composed of quartz, feldspar, and biotite, collected at 0.25 m (S1), 0.5 m (S2), 0.75 m (S3), and 1.0 m (S4) depths was used. The methodology included: regular soil-characterisation procedures such as physical index, chemical analysis, and grain size distribution; mineralogical analysis using optical microscopy, x-ray diffraction, and thermo-differential analyses; mercury porosimetry; Soil Water Retention Curve (SWRC); and Scanning Electron Microscopy (SEM). In addition, a 3D- microtomography was performed. The results depict the μ CT as an important tool, providing extra information about the soil structure. By overlapping the data obtained from the procedures performed in this research, it became apparent that the μ CT results cannot replace regular soil characterisation. However, it must still be considered a relevant tool for soil structural analysis.

Impact factor: Non-destructive 3D analyses are fundamental for soil characterisation, as it allows for qualitative and quantitative analysis, upgrading from conventional geotechnical lab procedures.

Keywords: 3D Microtomography, soil characterisation, pore quantification.

Introduction

Problems such as landslides, erosion, disposal, and reuse of mining, transport of contaminants, and degraded area recoveries are evaluated, studied, monitored, and solved using many concepts in which soil characterisation is a crucial component, as these are associated with the prediction, prevention, and remediation of natural and man-made accidents.

The use of 3D-microtomography (μ CT) for geotechnical and earth science purposes is related to the comprehension of the materials, as the soil structure may still contain characteristics of the origin material and/or information on pre-existent geomorphological processes (e.g., it is possible to highlight the mineral banding and alignment from different types of rock), allowing us to understand the connection between the environment and the soil.

In addition, considering that it is not possible to observe and analyze the internal structure in a conventional soil characterisation, the microtomography imaging contribute to fill the theoretical gaps in the light of understanding pore distribution, grain surface, grain distribution, layering systems, and soil anisotropy. Furthermore, by using the dual energy technique, it is possible to identify different materials, isolating some interesting compounds such as quartz and iron oxides.

Although there are a vast number of potentials uses, the procedure also has limitations. Alves *et al.* (2013) pointed out that results are related to the resolution of the equipment, and the data quality is dependent on the algorithms used in the data processing software.

3.1.

Review (3D Microtomography)

The use of microtomography (μ CT) for the study of physical properties of the soil has been emphasised in several correlated sciences (agronomy, geography, geology, and geotechnics) as an extremely relevant means of analysis (Crestana *et al.*, 1992; Cruvinel, 1990; Eliot & Heck 2007b; Tainá, 2008; Issanov *et al.*, 2009;

Huillca, 2014).

As such, the method performs non-destructive investigations with 0.5 to 50 μm of resolution of multiphase porous systems (Crestana, 1994; Luo *et al.*, 2010).

The μCT procedures are used to evaluate soil compaction (Vaz *et al.*, 1992), determine the spatial distribution of soil moisture content (Hainsworth & Aylmore, 1983; Tippkötter, 2009), and evaluate the macro porosity and density of particles of different materials (Petrovic, Siebert & Rieke, 1982; Macedo & Crestana, 1999; Stolf *et al.*, 2011; Rab *et al.*, 2014; Passoni *et al.*, 2015; Bacher, 2015).

In the matter of internal analysis, the μCT is used as a key element that is able to provide detailed information in two or three dimensions (Crestana, Mascarenhas & Pozzi-Mucelli, 1985; Eliot & Heck 2007a; Wang *et al.*, 2011), producing quantitative and qualitative results. This technique consists of measuring the spatial distribution of a physical amount called attenuation coefficient, mapping the object's internal constitution and providing cross-sectional digital images.

In computerised tomography, the radiation intensity I , attenuated by an object, is compared with the original radiation I_0 , generated by the radiation source. In this way, it is possible to calculate the attenuation across the object (soil particles) from the source until the detector. Considering a simplified and homogenous object with a monochromatic source with just one radiation energy, it is experimentally well-known that (eq. 3.1):

$$I = I_0 e^{-\mu d} \quad (\text{eq.3.1})$$

Where:

I is the radiation intensity measured by detector;

I_0 is the radiation intensity delivered by the source;

μ is the linear attenuation coefficient;

d is the object thickness.

Although the explanation may look simple, there is a strong occurrence of non-homogeneity in natural materials. The attenuation coefficient varies in order

to deal with this, and the sources are polychromatic with a range of energy that varies from 0 to a maximum energy value ($E_{\text{máx}}$).

The calculation is done by the sum of the attenuation in small slices that comprises the object to obtain the total attenuation. The path of radiation is related to different structural composition of the objects subjected to the tomography. Thus, the equation to be solved is (eq.3.2):

$$I = \int_0^{E_{\text{máx}}} I_0(E) e^{-\int_0^d \mu(E) ds} dE \quad (\text{eq.3.2})$$

In general terms, for many 3D image systems, the object is placed close to the source to increase the resolution. Thus, the relevance of using x-ray sources with the smallest possible focus (micro focus or nano focus) to obtain a cone with a higher solid angle for the radiation is observed. Additionally, it is limited by heating and the radiation intensity, both associated with the available system power.

All these considerations provide a correlation between sample thickness and spatial resolution, so that the smallest observable detail (or the voxel size – *volume element*) is 1/1000 to 1/2000 of the sample thickness (depending on the sample size).

With the evolution of technology, the typical limitations of the geometry of a benchtop scanner were partially solved by positioning a special optical microscope between the sample and the detector and using lenses with scintillators in the input, which convert x-rays into light, which is then captured by a specialised detector.

Such advents make it possible to perform a tomography and take a sample at low magnification and low resolution, and then focus and enlarge a region of smaller interest. This procedure obtains projections with higher resolution, allowing the acquirement of the images of the soil sample's layers in any orientation (Figure 3.1). Furthermore, the composition and density of a volume element (voxel) are related to the attenuation coefficient.

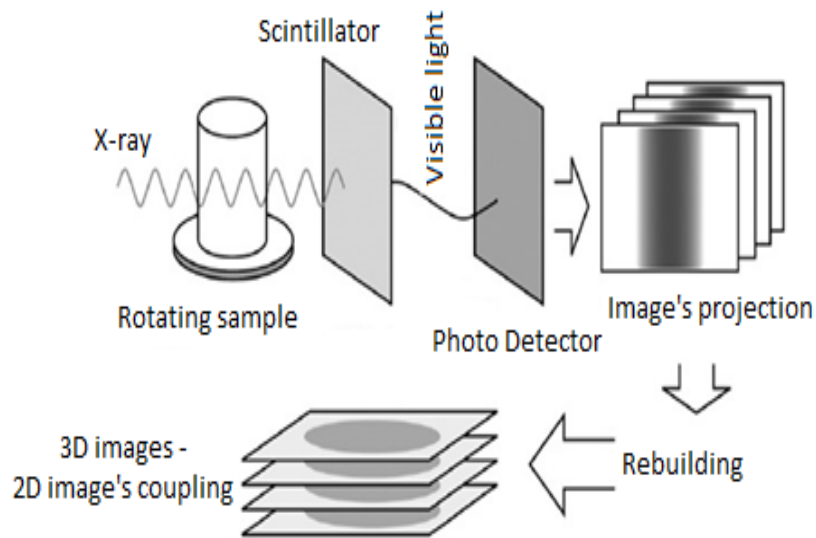


Figure 3.1 - Acquisition and reconstruction of the simplified scheme (Alves, 2015)

For multicomponent materials, such as soil, the image interpretations are complex because of the high difficulty to visualise different grey tones on the finer material. Furthermore, poly energetic or poly chromatic beams represent an additional difficulty, considering the soil density association and the effective atomic number inside the attenuation coefficient composition.

In this way, there is an interest in applying the dual energy technique (μ CT-DE) by polychromatic beam microtomography to identify the composition, density, and atomic number inside the soil sample. However, it cannot be performed by any conventional test because, until now, it could not be achieved by a conventional tomographic system, as there is no single combination of these parameters for a specific energy or energy spectrum. Regarding this, the problem can be solved by acquiring data with 2 different x-ray spectra, characterising the μ CT-DE (Alves, 2015).

Changes in the values obtained in the conventional computed tomography can be associated to a change in density ρ and in the effective atomic number Z_{ef} of the object. This corresponds to the physical definition of the linear attenuation coefficient (eq.3.3):

$$\mu = \mu/\rho (E,Z) * \rho = \mu_m * \rho \quad (\text{eq.3.3})$$

Where:

ρ is the density of the object;

Z is the atomic number of the object;

μ_m is the mass attenuation coefficient.

However, the mass attenuation coefficient is dependent on the energy of the radiation and the atomic number of the object in question. It is possible that the combination of the density and atomic number parameters provide similar values for the linear attenuation coefficient, which would result in similar attenuation coefficient images, not allowing the differentiation of different structures inside the soil.

In this way, the μ CT-DE technique uses the energy dependence of μ due to the atomic number of the materials that make up the object. In general, two tomograms acquired with different energy spectra from the radiation source allow us to relate the differences in the attenuation coefficient of the tomographic image.

Then, the μ CT-DE permits the reconstruction of the tomography of an object, where the final result provides the distribution of the density and the effective atomic number in the object volume.

The grayscale values obtained in the tomographic images are proportional to the radiation attenuation, which is dependent on the density, the effective atomic number, and the radiation energy. An increase in the atomic number generates a predominance of the photoelectric absorption effect.

The acquisition of homogeneous calibration materials in two different energies allows the reconstruction of two new images. However, the dual energy method is extremely sensitive to small variations in the image or acquisition artefacts. In this way, tomographic acquisitions with good image quality are necessary, preferentially eliminating distortions due to ring artefacts and beam hardening.

The most important points to be evaluated for a better result by the dual energy technique are: signal to noise ratio (SNR), reducing the presence of noise in the image, and the use of filters, either physical or computational, to decrease the effect of hardening of the beam in the reconstructed tomographic image,

especially for more attenuating (denser) materials.

The decomposition of the materials provides the information on the differences between the two measured attenuation values. The differences may be extremely small, particularly if the actual energies used in the two measurements are not considerably different. The images with the use of μ CT-DE also present greater noise, as any small variation, such as object movement, can be interpreted as a variation in the internal composition of the object.

In this context, it is reinforced that there is a relevant interest in the non-destructive study of soil samples for geotechnical purposes, as the analysis of the interconnected and occluded pores may reveal peculiarities hitherto little seen. The μ CT is a viable alternative, as it presents a solid theoretical recognised base, reliable results, resolution of micrometres for microscopic identification, and does not require the destruction of the samples, emphasising the ability to segment images in mineralogical phases, as shown in Figure 3.2-a (three mineral samples were used for exemplification: fluorite, howlite, and opal), and Figure 3.2-b (identifying the different minerals through different colorations defined in scale).

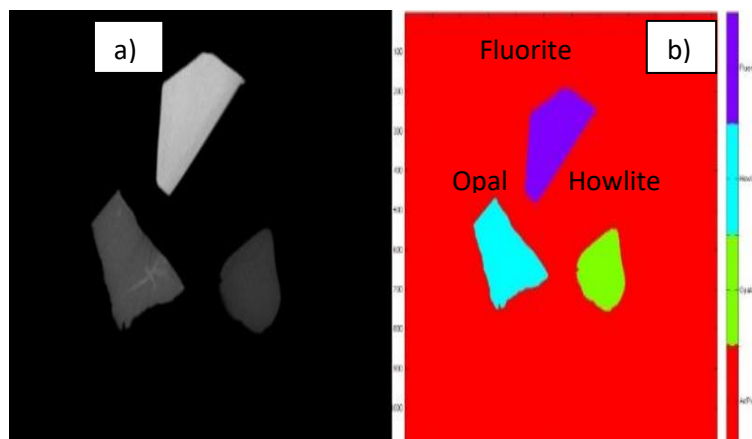


Figure 3.2 - a) RAW microtomography image. b) Mineral segmentation (Alves, 2015)

The typical contrast generated by traditional microtomography depends essentially on the absorption of x-rays by the sample, that is, the interaction of the x-ray with the sample and the attenuation of its intensity due to these interactions. In this way, modern lenses, which are used in this research, allow to perform procedures under geometric conditions in which phase delays in the x-ray wave can be enhanced.

These delays are caused by interfaces between different compounds or voids present in the sample. In addition, they are more sensitive to samples of low atomic number. As a result, better boundary definition and better contrast between phases with similar absorptions can be obtained.

Further, the absorption of x-rays in μ CT depends essentially on the Compton and photoelectric effects on the interaction between x-rays and matter. The intensity of these effects varies basically with the energy of the radiation and with the atomic number of the materials.

To conclude, the tomographic image is an interpretation of the x-ray absorption by the sample under analysis. However, this absorption depends on the density and the effective (atomic) number of the sample. In some materials, it is possible that the combination of these parameters provides an extremely close absorption, preventing discrimination of the different phases in the image.

Finally, to solve small differences in X-ray absorption, it is possible to perform tomographic images acquired at two different energies, and it is possible to combine the results obtained to discriminate between similar materials.

3.2.

Materials and Methods

For this paper, the materials used were soils from Tinguá, Nova Iguaçu city, Brazil. Before the field campaign, a geologic and geographic survey was realised, indicating that the site is surrounded by talus and colluvial deposits over the low talweg slopes comprised also by residual soils in steep areas. Further, regarding the geological survey, the macro area is composed of intercalations granitic orthogenesis and biotite gneiss.

After the geological data acquisition, a field campaign was assembled to choose the sampling area. In this way, colluvial soils, from coordinates 663961E/7500946N, were collected at 0.25 m (S1), 0.5 m (S2), 0.75 m (S3), and 1.0 m (S4) depths. After obtaining the undisturbed soil sampling, the material was taken into a chamber to be protected against moisture loss. Subsequently, the materials were portioned and used in the physical, mineralogical, and structural characterisations.

Regarding the methodology, the current research presents the physical, chemical, mineralogical, and structural characterisation. In this way, the grain size distribution procedure was performed by sieving (for coarse grains), and by sedimentation (with and without dispersive solution). In addition, a laser particle size analyser was used for finer materials grain size characterisation. The Atterberg' limits were taken and additionally, the activity index was determined. In complement, chemical analyses were realised to verify the possible weathering traces and the soil's chemical composition. Regarding the mineralogy, a structural analysis of the dried and moistened materials was performed with a microscopy apparatus. Further, a differential thermal analysis and an x-ray diffraction were conducted to obtain more information on the soil's mineral classification. For the structural analyses, a soil water retention curve (filter paper method), a porosimetry (by mercury's injection), a scanning electron microscopy (SEM), and a 3D microtomography were performed.

Finally, in the matter of the microtomography procedure, the soil samples were tested to obtain internal data about its structures. In this way, the acquired images were submitted to several stages of processing and analysis to obtain quantitative information such as:

- 1) Noise reduction pre-processing, background correction, homogenisation of brightness, and contrast between layers.
- 2) Segmentation to discriminate between structures of interest.
- 3) Post-processing to correct segmentation defects and morphological discrimination between structures (e.g., open pores vs. closed pores elongated cracking pores, etc.)
- 4) 3D measurements such as volume, surface area, main axes, elongation, alignment, sphericity, and compactness.
- 5) 3D visualisation (rendering) of the discriminated structures, with the generation of videos and virtual navigation within the material.

3.3. Physical Characterisation

A set of 3 undisturbed samples was used for the soil characteristics in each depth (0.25, 0.50, 0.75 and 1 meter), and the physical indexes determined by volume-mass relations are presented in the Table 3.1.

Table 3.1 - Physical indexes

Sample	Value	Gs	ρ_n (g/cm ³)	ρ_d (g/cm ³)	w _{rat} (%)	e	n (%)	S (%)
S1 25 cm	Max.	2.69	1.62	1.30	24.35	1.04	50.90	62
	Min.		1.66	1.34	24.01			62
	Av.		1.64	1.32	24.18			62
S2 50 cm	Max.	2.69	1.53	1.22	25.74	1.18	54.03	58
	Min.		1.55	1.26	23.35			53
	Av.		1.54	1.24	24.545			54
S3 75 cm	Max.	2.72	1.48	1.21	22.35	1.15	53.49	52
	Min.		1.61	1.32	21.91			51
	Av.		1.545	1.27	22.13			52
S4 100 cm	Max.	2.67	1.51	1.23	22.85	1.09	52.11	55
	Min.		1.62	1.33	21.97			53
	Av.		1.565	1.28	22.41			54

The grain size distribution (GSD) was classified by the Brazilian Technical Standards Association, NBR-7181 (ABNT, 1984b), and NBR-6457 (ABNT, 1984c) procedures. The measured data were analysed with a mass-based model, performing the sieving and sedimentation procedures, and the results are shown in Figure 3.3.

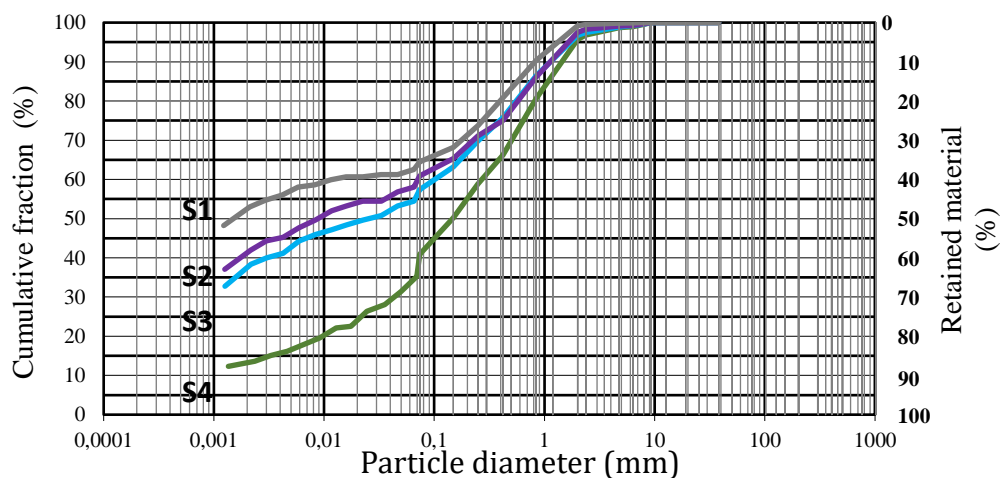


Figure 3.3 - Grain size distribution of the analysed soils

The sedimentation tests were performed with material that passed through the 0.42 mm (#40) screen mesh. At that time, was used 50 g of air-dried crushed soil, dispersed in 125 mL of sodium-hexametaphosphate solution. After 24 hours of standby, the soil and solution were mixed into a shaker, then poured into a 1000 mL measuring cylinder (filled with distilled water), and finally, the data were collected by a densimeter at regular time-intervals until 24 hours.

At the end of the densimeter's readings, the material was washed and sieved on the 0.075 mm (#200) mesh. The retained material was dried, and the fine material was also sieved. Further, the material retained on the 0.42 mm (#40) was washed and dried for coarse sieving.

The results present an increase of the sand percentage and a reduction of the total fine percentage along with an increase in the sampling collection depth (Table 3.2).

Table 3.2 - Grain size distribution (GSD)

GSD (%)		S1	S2	S3	S4
Boulder		0.49	1.74	2.50	3.21
Sand	Coarse	18.36	22.38	20.96	29.48
	Medium	12.67	9.77	12.59	16.03
	Fine	6.97	8.47	9.96	18.73
Total Sand		38.00	40.62	43.51	64.24
Fine	Silt	8.23	14.87	14.87	17.81
	Clay	52.97	41.96	38.35	13.65
Total Fine		61.20	56.83	53.23	31.47

With the aim to assess the fine soil fraction, the sedimentation was replicated without dispersion in a hexametaphosphate solution, depicting in Figure 3.4 the soils have a high flocculation behaviour because there is large difference between dispersive solution result's procedure in comparison with water solution procedure.

Further, the particle analyser CILAS 1180 was used (tenting 2 grams of soils). The results revealed a different pore size distribution, probably due the scale effects.

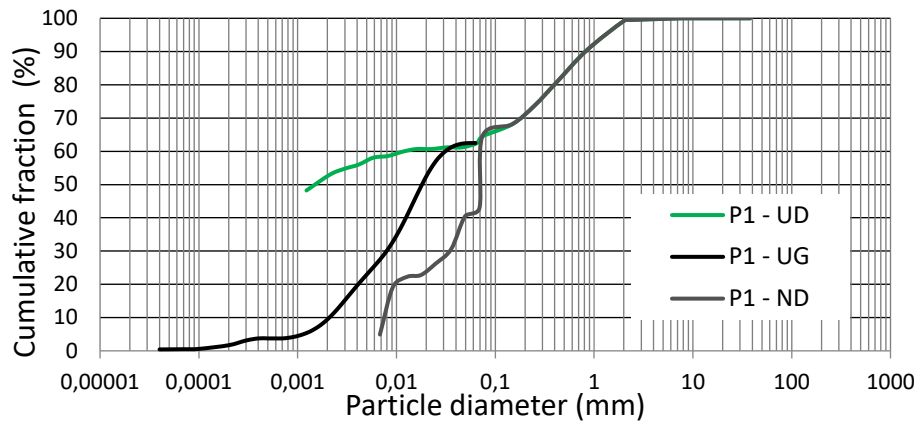


Figure 3.4 - Grain size distribution: S1 (a), UD – using dispersive solution; UG – using CILAS 1198; ND – without dispersive solution

The Atterberg limits were also determined. The Liquid Limit (WL) and the Plastic Limit (WP) were performed based on the NBR-6459 (WL) and NBR-7180 (WP), using the #40 sieved material. In addition, the activity index (Acl), was determined.

The obtained results are presented in Table 3.3, where it is possible to observe the values for all the samples analysed. The values of sample 3 clarify a normal activity of the clay. All the other samples present an inactive result.

Table 3.3 - Atterberg limits

Sample	WL (%)	WP (%)	PI (%)	Acl
S1	65.7	39.3	26,4	0.50
S2	61.1	38.3	22.8	0.54
S3	56.8	12.3	44.5	1.16
S4	33.4	27.3	6.1	0.44

3.4.

Chemical - Mineralogical Characterisation

The mineralogical characterisation presented in this paper relates to the evaluation, quantification, and qualification of the soils' mineralogy. Regarding this, the analysis of chemical composition, binocular lens (microscopy), x-ray diffraction, and differential thermal analysis are depicted in this section.

The chemical characterisation was performed in the PUC-Rio chemistry laboratory, according to EMBRAPA (1997) procedure, carried through by x-ray

fluorescence. The results present the main oxides of the soils inside secondary materials such as Alumina (Al_2O_3), Silica (SiO_2), Iron (Fe_2O_3), and Titanium (TiO_2), measured in g/kg (Table 3.4).

Table 3.4 - Chemical analyses

Sample	g/kg					
	Al_2O_3	SiO_2	Fe_2O_3	TiO_2	K_2O	SO_3
S1	54.81	36.52	6.74	1.12	0.41	0.35
S2	58.36	32.21	7.32	1.24	0.42	0.29
S3	57.06	34.15	6.24	1.11	1.06	0.27
S4	55.27	35.49	4.21	3.88	0.79	0.24

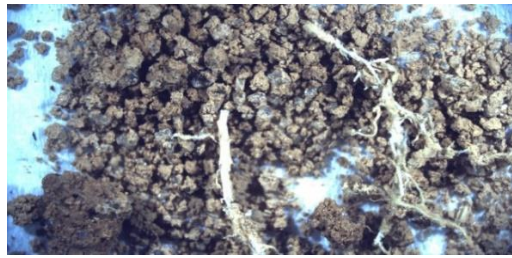
In complement, to determine the weathering Ki index (Antunes *et al.*, 1975), the sulphuric attack procedure was realised by EMBRAPA. This routine represents the soil colloidal molecular relation between silica and aluminium to evaluate the clay mineralogic composition (eq.3.4).

$$\text{Ki} = \text{mols of SiO}_2 / \text{mols of Al}_2\text{O}_3 \quad (\text{eq.3.4})$$

Further, Ki values below 2 indicate a weathered (mature) soil. For Ki equal to 2, the colloidal fraction is composed essentially of kaolinite, and for values greater than 2.50, the fraction is composed of 2: 1 clay minerals (Duriez *et al.*, 1982b).

Regarding the similar chemical composition of the soils, the average result obtained for the Tinguá colluvium indicated a KI equal to 1.39. It confirms the high degree of weathering of the materials. However, the values depicted by EMBRAPA emphasise the soils is comprised mostly by silica while the PUC-Rio chemistry analysis revealed a higher value of aluminium.

The mineralogical analyses comprised the use of binocular lens, model NIKON SMZ 800N. The material was initially verified in the natural water content condition (Figure 3.5 column a), revealing a root occurrence in S1, a reddish colour in S2 and a coarse material for S3 and S4. Further, the soil was washed on the #40 sieve and dried inside the 110°C oven (Figure 3.5 column b), revealing with increased depth, the soil is composed of an increased variety of materials while the quartz grains are more prominent in the sample collected near the surface.



Column (a) – S1 -> Scale 1cm:1000 μ m



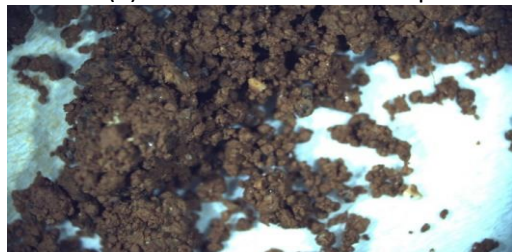
Column (b) – S1 -> Scale 0.8cm:500 μ m



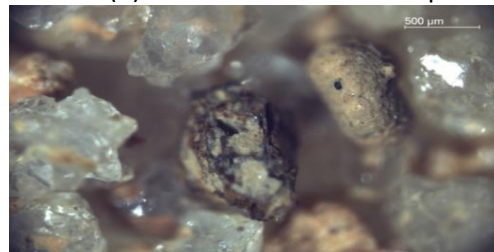
Column (a) – S2 -> Scale 1cm:1000 μ m



Column (b) – S2 -> Scale 1.5cm:500 μ m



Column (a) – S3 -> Scale 1cm:1000 μ m



Column (b) – S3 -> Scale 1cm:500 μ m



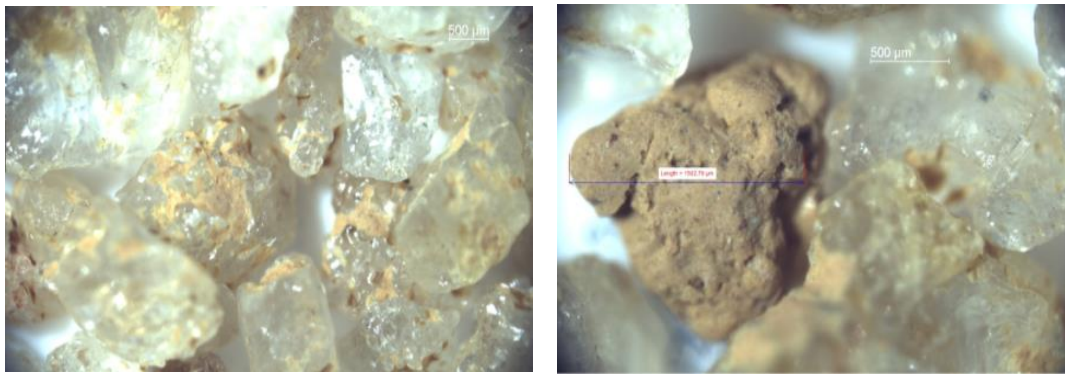
Column (a) – S4 -> Scale 1cm:1000 μ m



Column (b) – S4 -> Scale 0.7cm:500 μ m

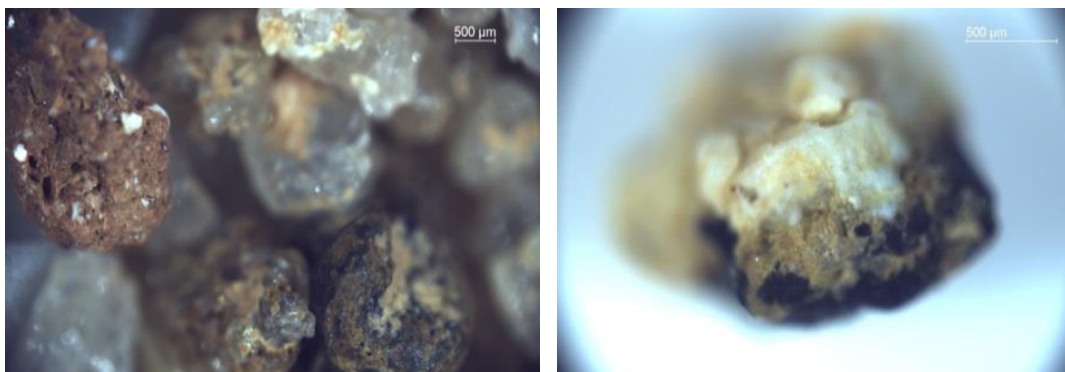
Figure 3.5 - Column (a) – Moistened samples. Column (b) Washed material retained on the sieve #40

Further observations from the washed materials analyses (Figure 3.6) include: iron-oxides joined to quartz (a–S1), iron-clay concretions (b–S2), modified biotite and iron-clay concretions (c–S3), and biotite-feldspar concretions (d–S4).



a – S1

b – S2



c – S3

d – S4

Figure 3.6 - Washed materials, retained on the #40

The x-ray diffraction was performed for all samples to identify the soils' crystalline phases. These tests were conducted by the Materials and Metallurgy Science Department at PUC-Rio. A Siemens D5000 diffractometer was used, disposed inside a of range 3 to 32°, with 0.02° of scan per second.

The clay mineral identification procedure consists of taking a soil powder from the material passed through the #40 sieve and, on a small plate, analysing the fine sand, silt, and clay composition. The results present 2θ peaks that indicate gibbsite and quartz for the analysed material (Figure 3.7).

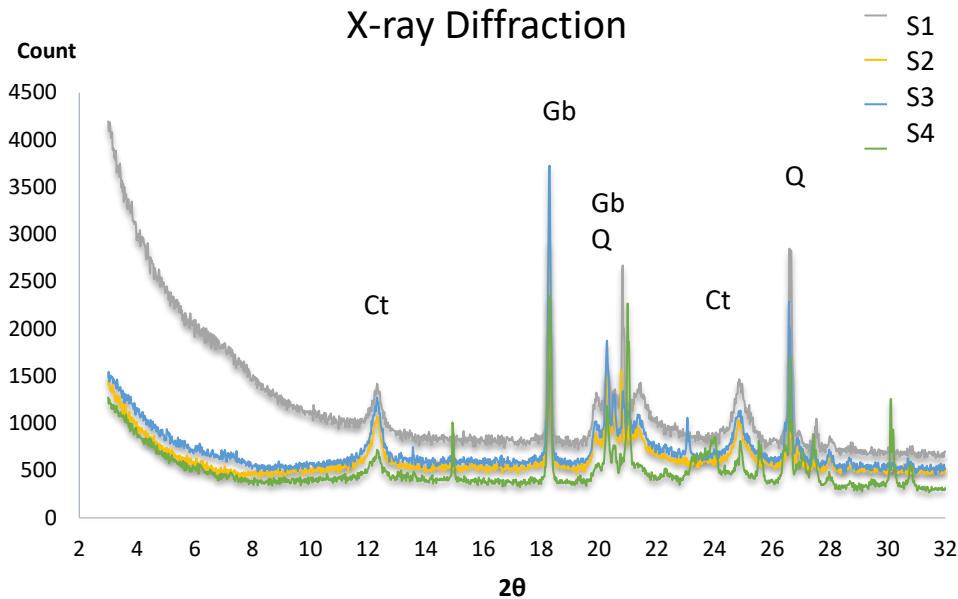


Figure 3.7 - Diffractogram. Ct = Kaolinite / Gb = Gibbsite / Q = Quartz

Upon concluding the mineralogical characterisation, the Differential Thermal Analysis (DTA) was performed. The procedure consists of heating the material at a constant velocity with a substance thermally inert, while registering the temperature.

The tests were carried out at the Department of Materials Science and Metallurgy (DCMM) of PUC-Rio, using an equipment manufactured by Perkin Elmer, with a Pyris data acquisition system. The samples with fraction passing through the # 40 sieve were heated to 890 °C, increasing 10 °C per minute, and the thermogram obtained for the soils are presented in Figure 3.8.

When endo or exothermic transformations occur (onset and end, as seen in Figure 3.8), they appear as deflections (Carvalho, 2012). According to Santos (1975), the water filling the capillaries of the soil presents an endothermic and acute peak, with a maximum temperature of 110 °C. Gibbsite and goethite often have superimposed endothermic peaks, as they lose their water of constitution at around 300–350 °C. At 450 °C, the kaolinite dihydroxylation reaction is initiated, completing at 600 °C (presence of an endothermic peak at this temperature).

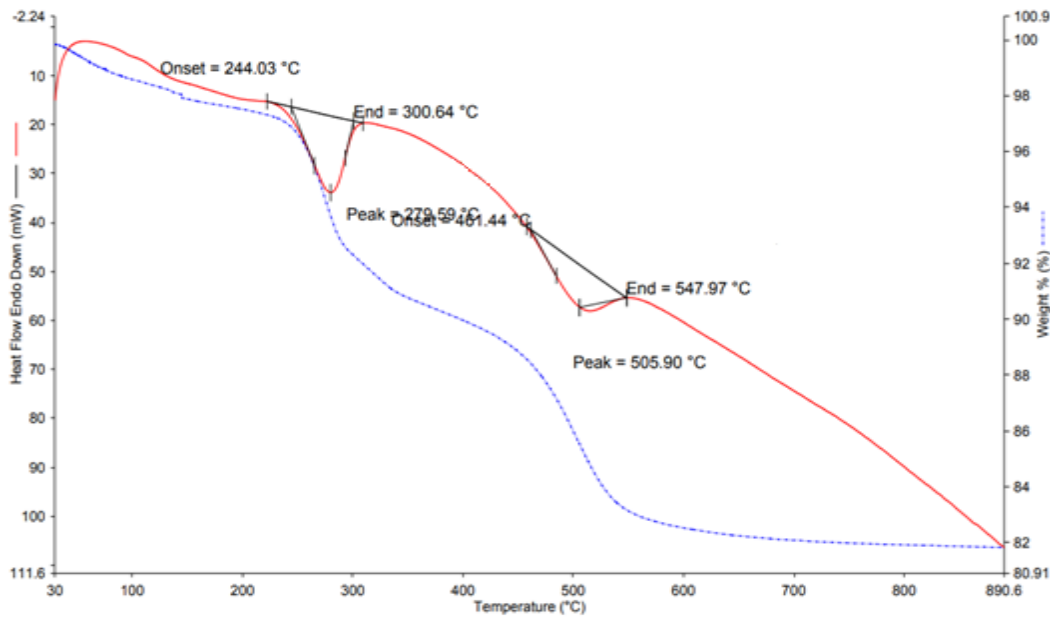


Figure 3.8 - S1 Differential Thermal Analysis (DTA)

3.5. Structural Characterisation

Soil structure is related to the spatial heterogeneity of different components or properties, depending on mineral origin and void distribution. In this way, the soil water retention curve (SWRC) was performed using the filter paper method (ASTM, 2003). The result points out the soil saturation and its matric suction correspondent in the macro and micro pores, depicting a bimodal behaviour (Figure 3.9).

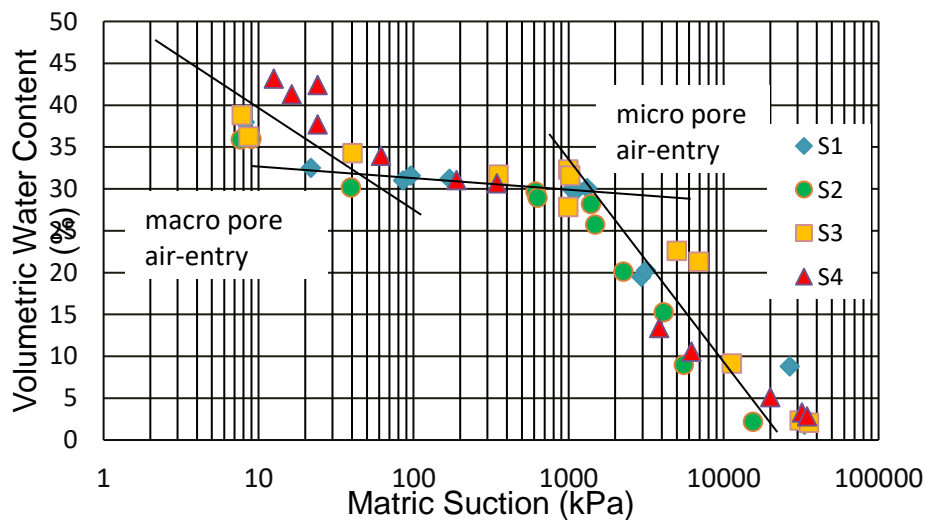


Figure 3.9 - Soil water retention curve of sample S1, S2, S3 and S4

The SWRC illustrates the macro pore air-entry value of 25 kPa (with 32,5% of volumetric water content), and, in the residual stage, the micro pore air-entry value (1500 kPa with 30% of volumetric water content).

In addition to the SWRC, the mercury intrusion porosimetry (MIP) was also performed in order to verify the pore size distribution, confirming or not the bimodal feature. The MIP procedure is a well-known technique in which mercury is injected at increasingly higher pressures into a porous material, and the injected volume is recorded.

The mercury injection allows the analysis of pore size distribution over the range of approximately 0.0036–1.000 μm . However, at high pressures, the particles can be broken and the closed pores can be opened, affecting the accuracy of the size of small pores (Penumadu & Dean, 2000; Kuila & Prasad, 2013). Despite these limitations, the ability of MIP to record pores (>50 nm) makes it a useful tool (Drake, 1949; Diamond, 1970; Delage, 2007; Romero & Simms, 2008).

It should be noted that this study chose to establish pore bands corresponding to grain size, according to ABNT (1995) NBR 6502/95. In this way, considering that the pore diameter is approximately ten times smaller than the grain diameter, it was assumed that the micro pore is related to the clay fraction ($\phi < 0.2$ μm), the meso pore to the silt fraction ($0.2 < \phi < 6$ μm), and the macro pore to the soil sand fraction ($\phi > 6$ μm).

These tests were carried out at the Laboratory of Support to Physics and Chemistry of the University of São Paulo in São Carlos with the Micromeritics Pore Size 9320 porosimetry. The equipment analysed pores with 0.7 mm in diameter with an applied pressure of approximately 0.0017 MPa, reaching pores sizes up to 0.000006 mm in diameter at a pressure of 212 MPa.

For the material (S1 and S4) presented in Figure 3.10, two main peaks were verified inside the micro-pores and macro-pores interval. These characteristics deal with the results obtained in Moncada (2008), Boszczowski (2008), and Carvalho (2012), where it was found out that the greater the soil weathering, the greater the percentage of micro pores present.

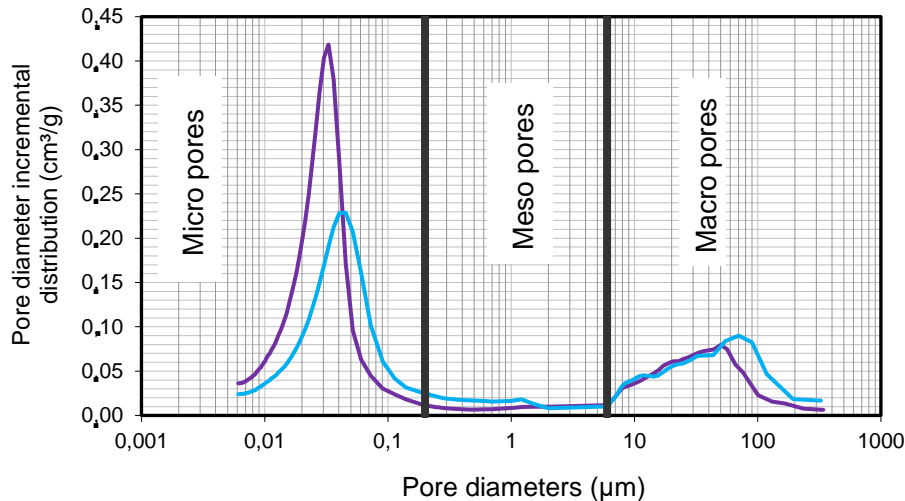


Figure 3.10 - Pore size distribution and mercury intrusion distribution

In the matter of mineral and structural correlation, a scanning electron microscopy (SEM) was performed to verify the internal arrangement. SEM is a technique used to generate a variety of signals at the surface of a solid specimen by high-energy electrons. The signals that derive from electron-sample interactions reveal information about the sample, including external morphology (texture), chemical composition, crystalline structure, and orientation of materials making up the sample. In most applications, data are collected over a selected area of the surface of the sample, and a two-dimensional image is generated that displays spatial variations in these properties (Pathak & Lokhande, 2014). Areas ranging from approximately 1 cm to 5 μm in width can be imaged in a scanning mode using conventional SEM techniques.

In addition, SEM is also capable of performing analyses of selected point locations on the sample. This approach is especially useful for qualitatively or semi-quantitatively determining chemical compositions using the x-ray dispersive-energy detector (EDS).

For this paper, cylindrical undisturbed soil samples with 1 cm of diameter and 0.8 cm of height were analysed (sample enlargement was limited once the imaging resolution was up to 10 μm). The tests were performed in the low vacuum microscopy model JSM-6510LV, manufactured by JEOL with a coupled Thermo Scientific - Noran System 7 EDS' detector at the Electron Microscopy Laboratory in the Department of Chemical and Materials Engineering, PUC-Rio.

The EDS procedure considers the soil particle X-ray spectrum, in which a focused beam of bombarded electrons is used to obtain a punctual chemical analysis. All elements from atomic number 4 (Be) to 92 (U) can be detected in principle, though not all instruments are equipped for “light” elements ($Z < 10$).

From the results, disposed in Figure 3.11, it was possible to identify gibbsite and probably goethite in the S1 and S2, lumps for the samples S3 and mineral orientation in S4. By the EDS analysis, the observed soils are composed essentially of aluminium silicates (clay minerals) and the iron oxides adhered to the clay minerals (Figure 3.12) for all the sampling depths.

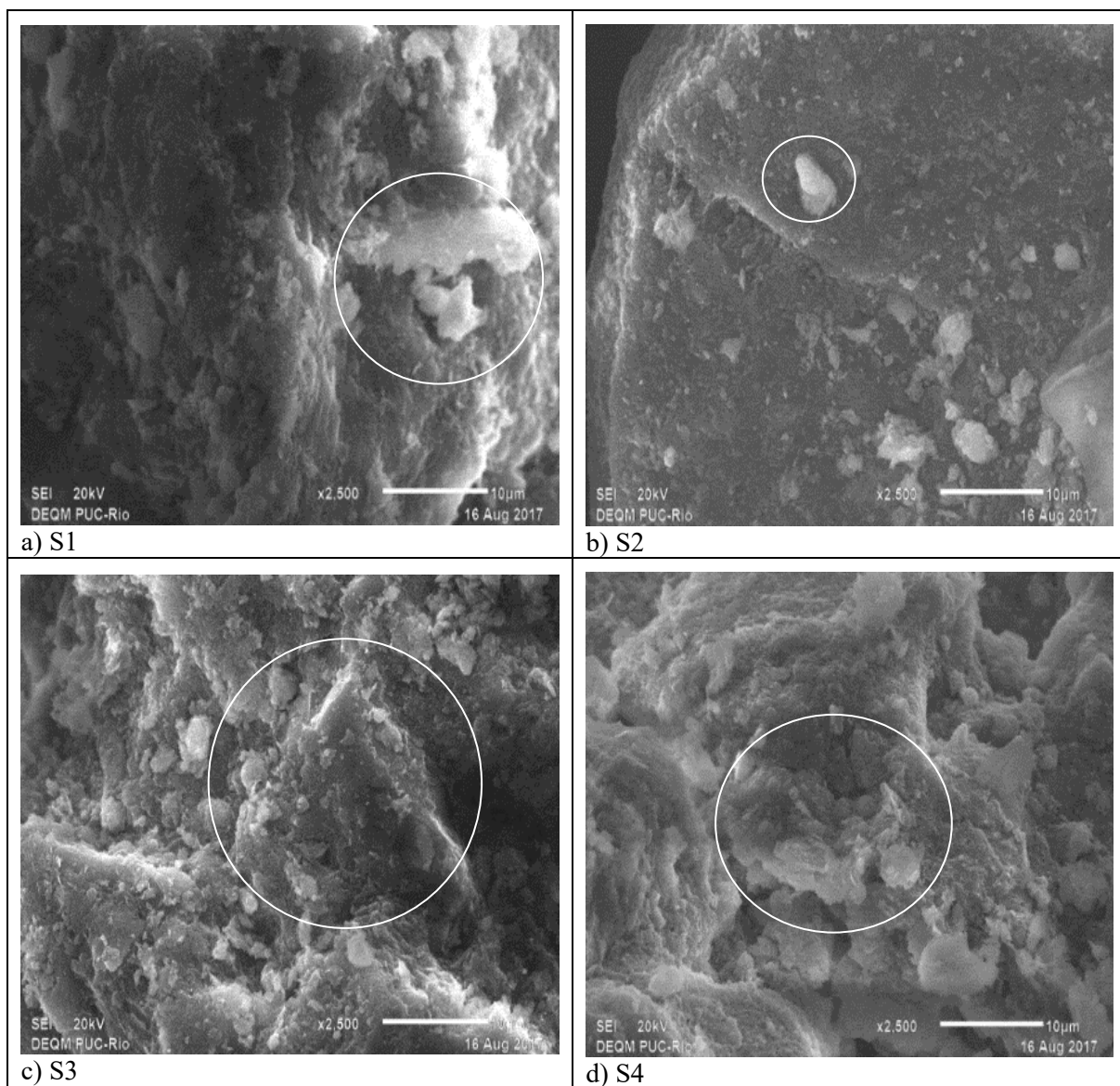


Figure 3.11- S1 (a), S2 (b), S3 (c) and S4 (d)

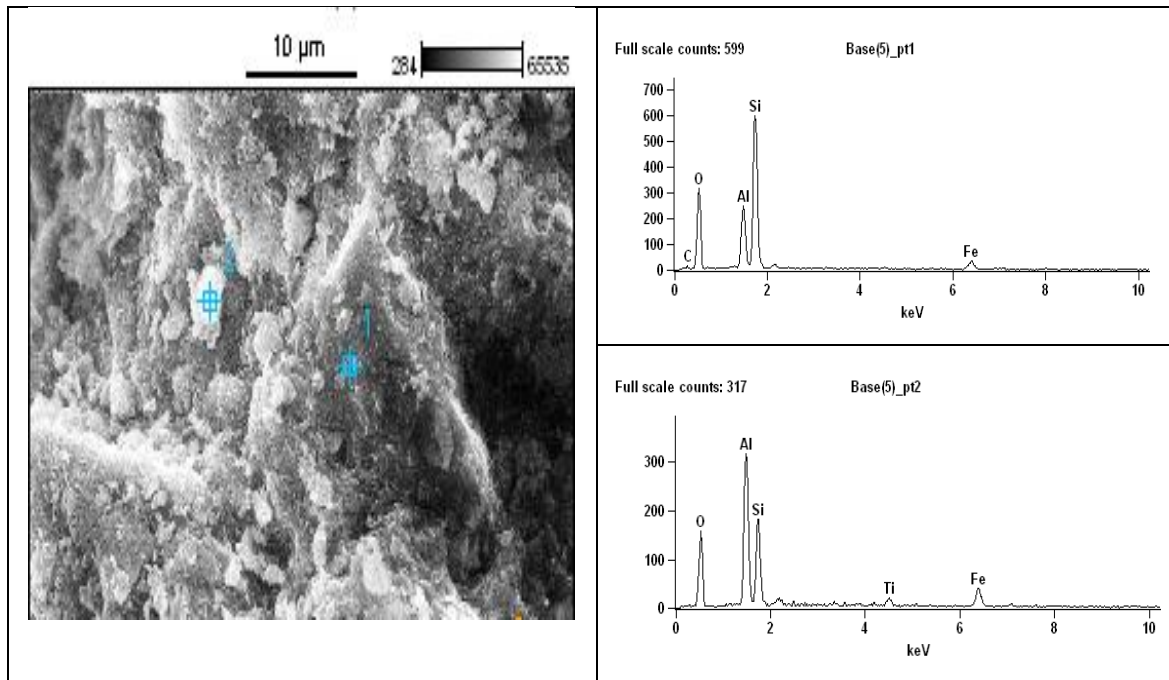


Figure 3.12 - SEM of soils

3.6. 3D Microtomography

Although microstructural investigation has evolved past the traditional microscopy techniques (resulting in 2D images), 3D analysis has not developed much over the past years. With this in mind, an x-ray 3D microtomography was performed with the Zeiss model X-Radia Versa 510 and Bruker Skyscan 1173 in order to build up geotechnical knowledge in this area.

The soil samples were prepared using undisturbed soils and were protected by a PVC cylinder (25 mm of diameter and 25 mm of height) in order to maintain the structural integrity and protect the soils against moisture loss during the microtomography procedure.

The mass-volume calculations were performed in the cylindrical core of the sample, having 7 mm height and 14 mm of diameter. In the light of the sample size, the voids distribution and quantitative analysis revealed the size of individual particles to be higher than 6 µm.

Considering the values of total porosity, it is important to emphasise that it is related to the macro-porosity, and because of this, it cannot be related to the regular total porosity of the soils, as presented in Table 3.1. In this way, Table 3.5

depicts a comparison between 3D-microtomography and regular soil characterisation values for porosity and void ratio, emphasising a much lower value in the μ CT results.

Table 3.5 - Microtomography data vs. regular soil characterisation data

Samples	S1	S2	S3	S4
μ CT - Total volume (cm ³)	1.44	1.26	1.37	1.41
μ CT - Solid volume (cm ³)	1.34	1.17	1.28	1.31
μ CT - Total volume of pore space (cm ³)	0.09	0.09	0.09	0.10
μ CT - Volume of closed pores (cm ³)	0.01	0.01	0.01	0.01
μ CT - Volume of open pore space (cm ³)	0.08	0.08	0.08	0.09
Porosity - Regular characterisation (%)	50.90	54.03	53.49	52.11
μ CT - Porosity - Macro pore (%)	6.41	7.26	6.44	7.10
Micro and meso pores (%) = (Porosity - Regular characterisation) – (μ CT - Porosity - Macro pore)	44.49	46.77	47.05	45.01
Void ratio - Regular characterisation	1.04	1.18	1.15	1.09
μ CT - Void ratio	0.07	0.08	0.07	0.08

The μ CT equipment resolution presents a reduced performance in the matter of quantifying the micro porosity. It occurred because of sample size and its relations with the emitted x-rays, that must to respect a limited area to quantify parameters, (Table 3.5). Thus, the sample size is a real limitation for the μ CT procedures because, in general terms, the tests must choose which focus will be performed for a quantitative or qualitative analysis. Regarding the qualitative approach, the opened and closed pores of the entire samples are demonstrated, considering only the macro pores, in Figure 3.13.

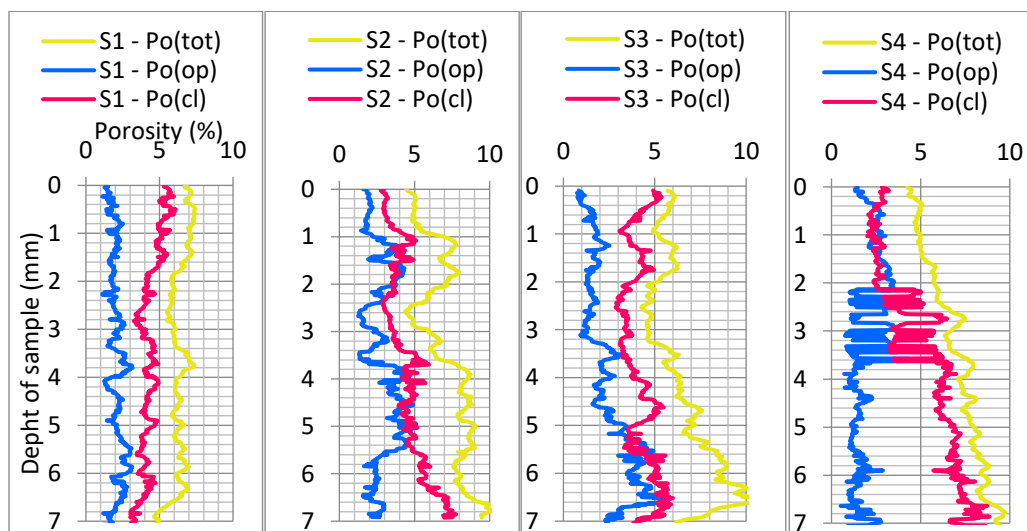


Figure 3.13 - Internal distribution of the porosity

Regarding Figure 3.13, it is emphasised that: the S1 presented more uniform distribution of porosity; the S2 and S3 increased the porosities at the bottom of the samples; the S4 had an internal disturbance, once it presented a remarkable variation of particles counted from 2 to 4 mm of depth.

For the internal analysis the images were rendered into Ctan software, creating a 3D microtomography images for the samples (Figure 3.14), depicting a raw - shade of grey for the 3D reconstitution of the material and the images of coloured isolated conditions.

Regarding a raw rendering, observed in 3D- Microtomography line, the samples were then cut transversally, and the oxide particles were presented. It revealed the samples S1 and S2 are different then S3 and S4 in the matter of mass density. It is confirmed by the white points and the grey shades disposed in the rendered images.

Concerning the iron-oxide distribution, it is clear a homogeneous distribution of small particles in S1 and S2 and higher cumulative values for, disposed in lumps, in the samples S3 and S4.

The void distribution has a complex arrangement and because the open and closed pores could not be separated in order to render the entire image. However, it is possible to visualise the diffuse voids distributions, highlighting no arrangement pattern.

Finally, the quartz distribution rendered image revealed large sizes particles in the sample S4.

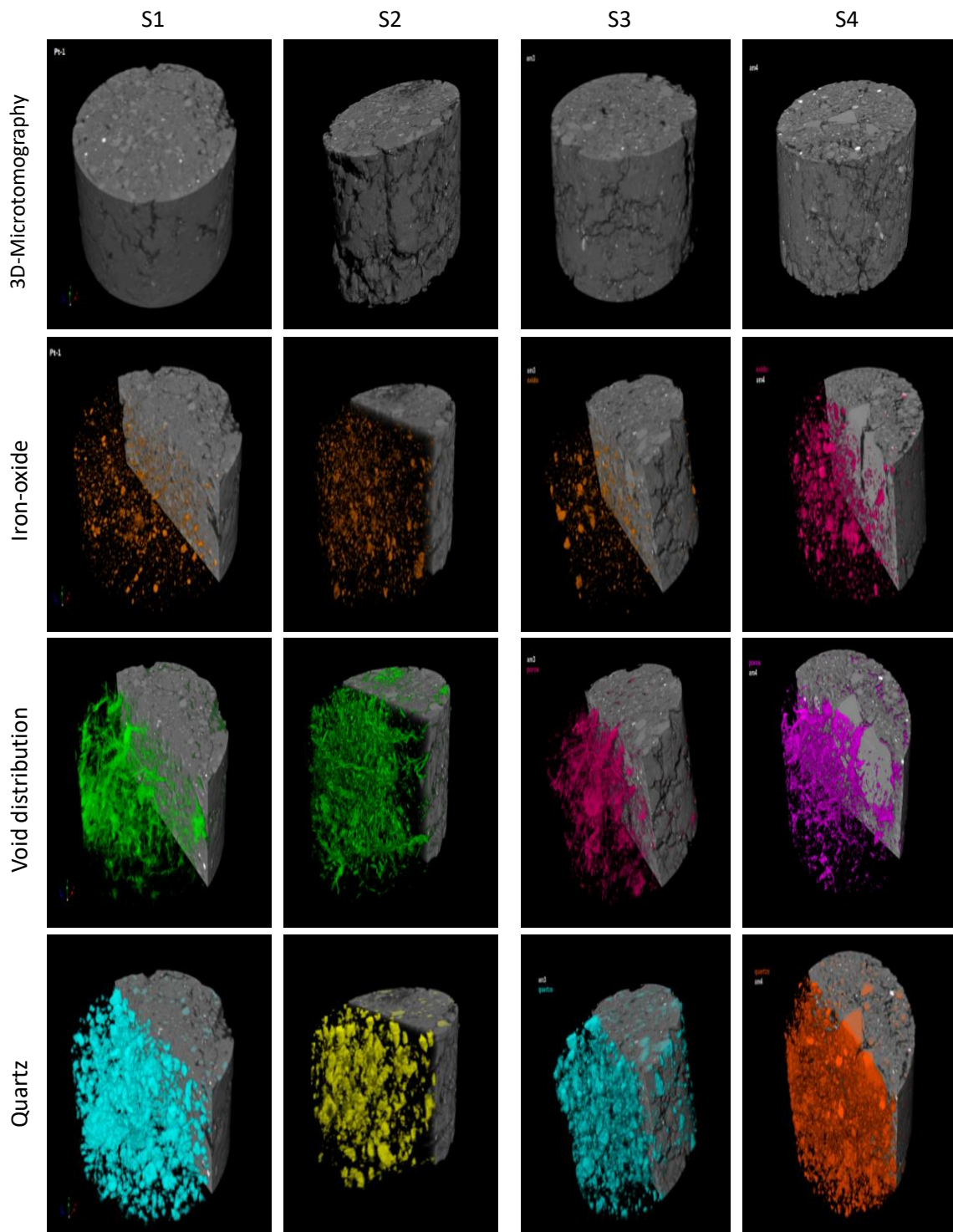


Figure 3.14 - 3D-Microtomography images

3.7.

Conclusion

The μ CT of the soils revealed in the rendered images a decrease of finer particles with an increase in depth (in accordance with the microscopy of and GSD analysis).

Concerning grain size distribution, the regular procedure can determine the amount of particle sizes, however, it cannot verify how they are arranged over the soil sample. In this way, the μ CT is revealed as an important tool because it is possible to confirm that S1 and S2 have a similar internal structure and the S4 has the coarse material comprised by cracked particles.

In terms of the dual energy isolation procedure, the μ CT did not revealed an arrangement pattern of different materials. However, the results show the main oxides of the soils such as Alumina (Al_2O_3), Silica (SiO_2), and Iron (Fe_2O_3). Nevertheless, it was not possible to isolate these materials as such the scanning electron microscopy (SEM).

Regarding the macro-pores and its characteristics, the use of microtomography was able to distinguish the open and closed pores.

Concerning the use of the μ CT as a complementary procedure to the soil characterisation, it is important to highlight that the range used during the imaging processes was not enough to substitute the conventional tests for obtaining soil parameters, such as mercury injection. This occurs due to the correlation between the size of soil sample and tomography resolution, requiring smaller samples to reach higher resolutions.

Finally, it is important to emphasise that further research must be conducted using small samples to perform high-resolution 3D μ CT in order to quantify smaller pore sizes.

4

A correlation between laboratory and field monitoring data: Producing a reliable field SWRC

Abstract

The correlation between predicted and measured data is an important subject to understand the environment and its transient features such as volumetric water content (VWC) and matric potential (MP). This Chapter aims to analyse the Soil Water Retention Curve by correlating laboratory data (based on the filter paper technique) and field monitoring data (based on the EC-5 and MPS-2 probes, manufactured by Decagon Devices Inc.) for colluvial soil from Tinguá, Rio de Janeiro, Brazil. The methodology consists of testing the influence of the variation of Bulk density on volumetric water content values by using the Proctor and a double ring hydraulic system (developed exclusively for this research campaign). In addition, three different installation procedures were tested: driving the rod directly into the soil, with application of mud inside the auger hole and with a hardened steel gauge. Finally, a microtomography of cylindrical samples was carried out to analyse the soil particles-rod coupling. The results point out that the frequency domain reflectometry EC-5 sensor accuracy is strongly connected to the bulk density of the material, producing higher volumetric water content values with increasing bulk density. Comparing the results obtained by the different EC-5 installation methods with laboratory results, it is possible to conclude that driving the rod directly into the soil is the best way to install the equipment, as the probe only underestimates the VWC data by 2.5%, while with the mud application, the results are underestimated by 4%, and with the gauge method by 5%. Hence, this Chapter indicates that the EC-5 requires calibration to obtain accurate data during field monitoring. Regarding the MPS-2, the results indicated that (if following the installation method specified by Decagon's Operator Manual) the calibration it was not necessary because the outputted data was well fitted to the SWRC performed with the filter paper method.

Impact factor: Field SWRC is a key aspect in the light of understanding drying-wetting soil cycles.

Keywords: Field monitoring soil water retention curve, FDR, 3D-microtomography.

Introduction

The use of field monitoring is expanding with the increasing interactions between society and the environment. In this context, real-time data acquisition is extremely important to predict and solve problems. In terms of geotechnical issues such as landslides, recovery of degraded areas and disaster management, the volumetric water content (VWC) and the water potential (MP) determination reveal remarkable information concerning the transient features of soil-weather interaction.

In this way, the soil water retention curve depicts free draining water and air-entry values, pointing out the transition from the saturated zone to residual water content of soils. Furthermore, it is well-known that suction, in broad terms, is related to the mechanical behaviour of soils by transient stress state variables (Fredlund & Morgenstern, 1976).

The procedures to measure and control suction and moisture content of soils are guided by Gardner (1937) and Richards (1944), who started to use the filter paper and pressure plate methods to determine the soil retention curve, which evolved respectively into ASTM 5298-94 (1997) and ASTM C1669 (2015). In the light of SWRC determination, Topp (1980) introduced the time domain reflectometry (TDR) as a technique to determine volumetric water content of soils by soil electrical permittivity, providing a new range of possibilities for real-time data acquisition and field monitoring.

Although the correlation between SWRC techniques has started almost a hundred years ago, this subject is still in progress, as new practices and arrangements are emerging. Comparisons between field and laboratory SWRC values have been presented by several authors (Morgan *et al.*, 2001; Li *et al.*, 2005; Osisnki *et al.*, 2016), who have reported divergences among the data acquired by different procedures (time domain reflectometry probes vs. tensiometer vs. filter paper vs. pressure plate).

Bearing that in mind, this study aims to reach a SWRC based on field monitoring data that comprises the use of sensors manufactured by Decagon

Devices Inc., with an MPS-2 probe for matric potential and an EC-5 probe for volumetric water content (VWC) data acquisition.

Hence, this Chapter sought to analyse the correlation between the soil's bulk density with VWC acquired values; evaluate different installation technics of EC-5 probes; verify the range and accuracy of the MPS-2 and EC-5 probes; and perform a soil water retention curve directly in the field monitoring area (FSWRC).

4.1. Review

The soil water retention curve is the constitutive relationship between water content or degree of saturation and suction (Barbour, 1998), based on the equilibrium conditions (Marinho, 2009).

Filter paper method

The filter paper method is a simple, quick and economical technique of measuring soil suction. The routine is based on the hypothesis that the filter paper has its suction equalized with the suction of the soils and it is revealed for a calibration curve that evolved for the type of paper accomplished (ASTM, D5298).

The suction in the unsaturated soils is recognized as resulting from the combined effects of different mechanisms. The total suction can be divided into matric and of solutes, where the first is related to the action of surface and capillarity forces, and the second, related to the presence of solutes in the free water (Tarantino, 2010).

The filter paper must be "quantitative", Type II, according to ASTM (1994) specifications. The most used are Whatman No 42. Further, the ASTM D 5298 emphasize the material must be initially oven-dried (16 h or overnight) and then allowed to cool to room temperature in a desiccator.

There are several calibration curves for the main filter papers used to determine the soil suction, however, there is no consensus on which is the most appropriate. In general, they are composed of two equations that indicate different

sensitivity of the filter paper response, for high and low suction levels (Moncada, 2004).

Further, to obtain correct suction values, some aspects must be considered, such as the suction equalizing time, the precision of the weighing scale, correct handling of the paper and the guarantee of a protection apparatus during the period of equalization. According to Fredlund & Rahardjo (1993), the response time of paper filter is on the order of one week.

Introduction to water content and suction field measurements

Measurements of water content is an ancient subject in geotechnical engineering because it is considered as an initial procedure when it comes to laboratory and field routines. To evaluate suction and water content an undisturbed soil sample is usually required and the direct method, based in the difference in weight before and after drying a soil, is a feasible procedure.

Conversely, considering a field monitoring condition, a laboratory approach is not the necessarily the better procedure to evaluate the water content and suctions correlations because of the difference concerned to equilibrium in both cases. Regarding this, such an approach requires sensors to measure a representative part of the SWRC in the field.

In the light of sensors to determine soil water content and water potential, the research performed by Carpena *et al.*, (2004), revealed a survey of indirect methods used for punctual measuring and/or field monitoring. These methods reveal the soil moisture by a calibrated relationship with some other predicted or measurable variable (i.e., voltage, amperage, etc.). The suitability of each method depends on several issues like cost, accuracy, response time, installation, management and durability.

Techniques classified such as volumetric and tensiometric, can reveal volumetric water content and soil suction or water potential (i.e., tension exerted by capillarity). Regarding volumetric moisture, this definition estimates the volume of water in a sample volume of undisturbed soil and it is considered a useful procedure for determining how saturated the soil is (i.e., fraction of total soil volume filled with the soil aqueous solution). When it is expressed in terms of

depth (i.e., volume of water in soil down to a given depth over a unit surface area), it can be compared with other hydrological variables like precipitation, evaporation, transpiration, deep drainage, etc.

The FDR is a method based in the electrical capacitance of a capacitor that uses the soil and its water content as a dielectric (Carpena *et al.*, 2004). When connecting this capacitor (made of metal rods) together with an oscillator to form an electrical circuit, changes in soil moisture can be detected by changes in the circuit operating frequency. This is the basis of the Frequency Domain (FD) technique used in Capacitance and Frequency Domain Reflectometry (FDR) sensors. In Capacitance sensors the dielectric permittivity of a medium is determined by measuring the charge time of a capacitor made with that medium. In FDR the oscillator frequency is swept under control within a certain frequency range to find the resonant frequency (at which the amplitude is greatest), which is a measure of water content in the soil.

Ec-5/MPS-2 soil water retention curve (Field SWRC)

When it comes to the determination a soil water retention curve in the field, some relevant researches in field monitoring area have been depicted. Researches such as performed by Beese and Ploeg (1976), emphasised that laboratory-measured suction values are in reasonable agreement with field measured values for selected periods. They revealed a drying (desorption) and a wetting (sorption) curve of the soil moisture retention for different soil-layer depths. Further, Li *et al.* (2005) pointed out that the field SWRC matches well with the wetting portion of the laboratory SWRC; however, wetting and drying cycles in the field present significant differences from the drying portion of the laboratory curve. In addition, Ng and Pang (2000) evaluated the transient seepage to predict pore water pressure distribution in natural and recompacted soil samples, pointing out a slight air-entry value for natural samples and depicting a pore-size distribution dependence.

4.2. Materials

In this research, were used soil samples from Tinguá, Nova Iguaçu, Rio de Janeiro, Brazil. The study area is situated in the Pontifical Catholic University of Rio de Janeiro Experimental Campus, under 663961E / 7500946N coordinates.

The soil profile comprises a colluvial material, developed within a biotite-gneiss domain. The grains size and physical characterisation analysis were performed using the Brazilian Standards (ABNT), NBR-718, NBR-6457, and NBR-6502, and the results of the material sampled in the 0.25 m depth are presented in Table 4.1 and Table 4.2.

Table 4.1 - Grain size distribution (GSD) data

Sample	Gravel	Sand			Finer		
		Coarse	Medium	Fine	Silt	Clay	Total
Colluvial	2.9	24.6	14.2	7.7	10.1	40.5	50.7

Table 4.2 - Physical Index

G_s	ρ_n (g/cm ³)	ρ_d (g/cm ³)	e	S (%)	WL (%)	WP (%)	IP (%)	A (Inactive)
2.66	1.59	1.3	1.06	0.58	60.9	39.1	21.8	0.43

4.3. Methods

Laboratory SWRC determination

The filter paper method (Marinho, 1994, 1997, and 2006) was used to determine the soil water retention curve in the laboratory. The filter paper Whatman No. 42 was kept in contact with the soil sample to determine matric suction was used 7 days for moisture equalization. During this period, the volumetric rings remained covered by a plastic seal, disposed into an expanded polystyrene box.

This research did not analyse the hysteresis effects. It emphasizes the approach performed by De Campos *et al.* (2005), that established the SWRC by wetting or drying the samples from their natural water content.

With regard to the mathematic equations used to adjust the experimental values in the SWRC, several authors (Gardner, 1958; Brooks & Corey, 1964; Van Genuchten, 1980; Fredlund & Xing, 1994; Gitirana Jr. & Fredlund, 2004; Durner, 1994; Burger & Shackelford 2001a; Burger & Shackelford 2001b; Zhang & Chen, 2005) emphasised that small variation of entry values may significantly affect the geometry of the curve.

In this research, the adjustment method used was that of Durner (1994). This model was chosen because it is an extension of Van Genuchten's model (1980) combined with Malem's (1976) conductivity prediction model. It regards unimodal curves superimposition, which is appropriate for heterogeneous pore systems such as bimodal and multimodal soils.

Equipment's

For this research two sensors manufactured by Decagon Devices were used: FDR EC-5 (Frequency Domain Reflectometry – Figure 4.1 a) and MPS-2 (Water Potential – Figure 4.1 b), both connected to an Em-50 data logger (also manufactured by Decagon Device Inc.).

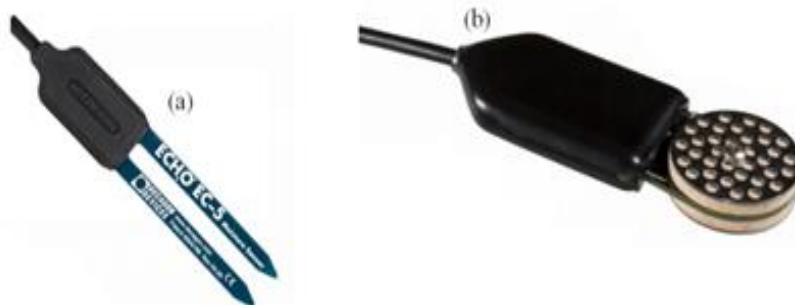


Figure 4.1 - a) EC-5 and b) MPS-2

The EC-5 determines Volumetric Water Content (VWC) and according to the Operator's Manual (Decagon, 2014), it works in the 70 MHz frequency band, minimising salinity and textural effects. In addition, it is calibrated for different soils such as mineral soils, potting soils, rockwool, and perlite.

For installation (Figure 4.2), the EC-5 requires a minimum distance (3.25 cm from the lateral and 2.25 cm from the bottom) from any barrier because the

sensor produces an electromagnetic field in which the water molecules are arranged.

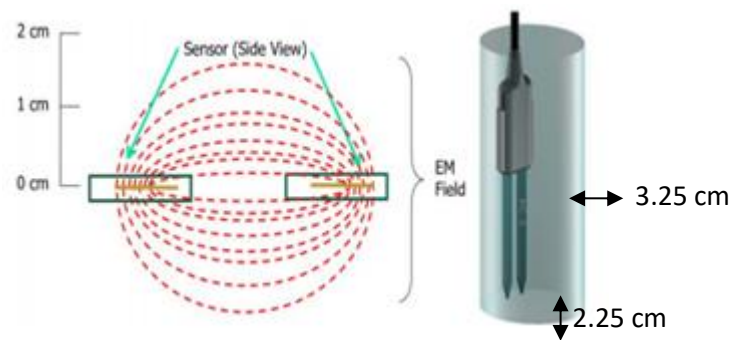


Figure 4.2 - Principle of operation of the EC-5 probe (Decagon, 2014)

Regarding the probe's range, Decagon's Operator Manual emphasises that the higher measurement frequency allows the EC-5 to measure VWC from 0% to 100% (VWC of saturated soils is generally 40% to 60% depending on the soil type). However, authors such as Veldkamp and O'Brien (2000), Portocarrero (2009), Choi *et al.* (2015), and Bore *et al.* (2015) emphasised that, in order to increase data accuracy, the sensors must be calibrated.

The MPS-2 is a water potential probe comprised by a vinyl cover filled with polyurethane resin, a printed circuit board, ceramic disks and a grounded stainless steel screens (Figure 4.3).

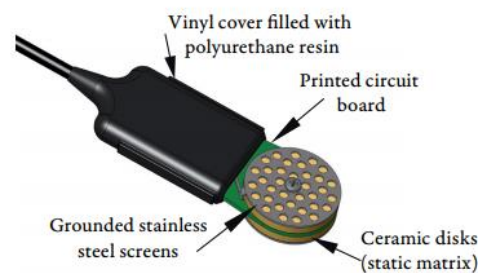


Figure 4.3 - MPS-2 (Decagon, 2014)

In comparison with Ec-5, the MPS-2 acquires values of the water potential of soils by measuring the dielectric permittivity of a porous ceramic disc instead of the soil between the EC-5 rods. This is possible because the dielectric permittivity of air, the solid ceramic, and water are different (1, 5, and 80, respectively), and the dielectric permittivity of the porous ceramic discs depends

on the amount of water present in the ceramic disc pore spaces. Further, in the matter of the equipment calibration, it is not affected by the soil type because the sensors only measure the water potential of the ceramic discs in equilibrium with the soil (Decagon, 2004).

Dielectric constant and Bulk dependency

Although it is considered a simple theory, reliable results are not easy to be obtained, requiring attention and care during the volumetric water content determination. Dielectric measurements of soils require high precision and are time-consuming due to the factors that affect soil dielectric behaviour (Figure 4.4.a), such as moisture and bulk density.

Cihlar & Ulaby, 1976, shows in the Figure 4.4.b that Bulk density has an important indirect effect on the relationship between dielectric constant and soil moisture content. Further, it was depicted that dielectric constant increases with bulk density for a given soil type (Figure 4.4 – a), suggesting that the volumetric water content values, produced by EC-5, will be modified if the Bulk density change.

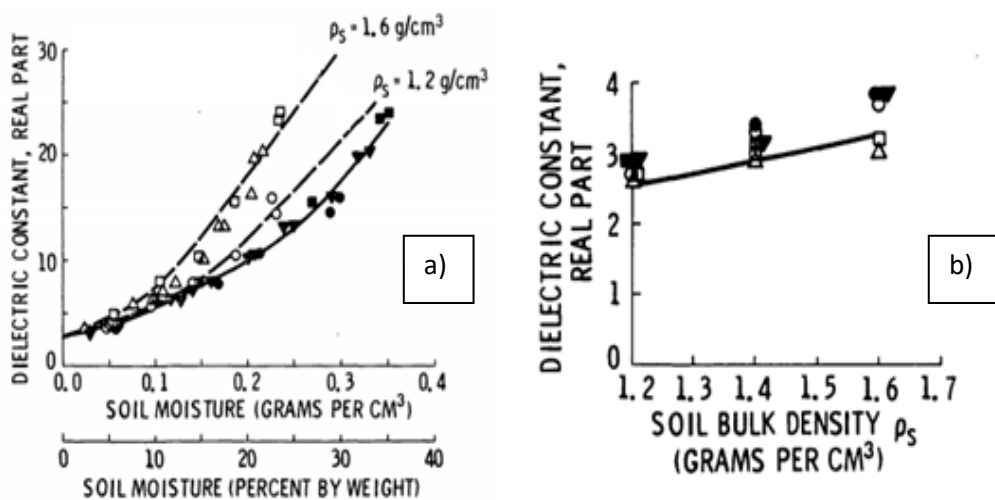


Figure 4.4 - a) Dielectric constant vs. soil volumetric moisture. b) Dielectric constant vs. soil bulk density. (Cihlar & Ulaby, 1976)

Regarding possible variation of EC-5 results, this paper sought to analyse if the Decagon's probe is sensitive to the increase of Bulk density. For this, the

test consists in remain the soil water content constant, increase the Bulk density of the material and verify the EC-5 volumetric water content readings.

The Bulk density and volumetric water content of the soil were initially determined in the field by using an average of 10 volumetric rings. The same material was collected, manually broken and taken to the laboratory for compaction procedures.

Two compaction methodologies were used to reach the same Bulk density of the field volumetric rings: The Normal Proctor (Figure 4.5-a) and a hydraulic-actuator compaction based-method, manufactured on a static compression procedure (Figure 4.5-b).

In the matter of Proctor compaction, 24 strikes were disposed in a radial distribution for 3 layers. However, to protect the probe, the central area was not reached by the standard socket.

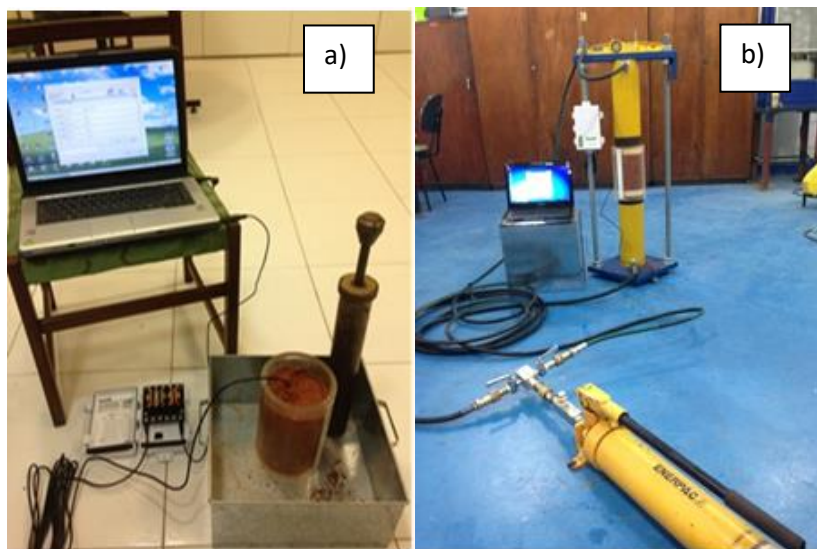


Figure 4.5 - Normal Proctor (a) and double ring compaction tests (b)

The developed equipment consists of two hydraulic 30 T actuators, manufactured by Enerpac, which are placed in opposite directions. Further, the setup has a reaction structure and one hollow acrylic cylinder ($d = 18$ cm; $h = 30$ cm), where two concave polyethylene plates (top and base) compresses the soil, driving its particles to the sensor contact in the central area. The measures were

performed as the soil compressed. It was possible because the hydraulic actuators have a hollow rod, that the cable was passed by and connected to data logger.

Regarding hydraulic compaction, the tests were carried out with the same displacement on the top and base. The routine remained the mass constant during the reduction of the cylinder's volume (Figure 4.6 – a-c). As such, the natural bulk density of the material was determined by direct volumetric measures of the cylinder.



Figure 4.6 - Hydraulic compaction (a to c)

Drying procedure – Performing the SWRC with the probes in the laboratory

To determine the range and the reliability of the Decagon's devices to reveal a field soil water retention curve, it was performed in laboratory procedure. The test used two cylindrical samples, in which, undisturbed soils were submerged to reach saturation. Further, the MPS-2 and the EC-5 probes were inserted to monitor, in the same time, the volumetric water content and matric suction during a (top face) drying period (Figure 4.7).



Figure 4.7 - Drying monitoring procedure

Testing installation procedures

After the laboratory routines, a field installation campaign began in order to evaluate how the procedures affects the volumetric water content results. For this, the EC-5 probes were analysed in three distinct installation procedures disposed in a 0.25m of depth such as: driving the rod directly into the soil, with mud support (inside an auger hole), and with a hardened steel gauge (Figure 4.8 (a), (b), e (c)). Here, to reach higher and lowers moisture values, the installation area was uncovered by vegetation and the site was exposed to sunlight all day long.

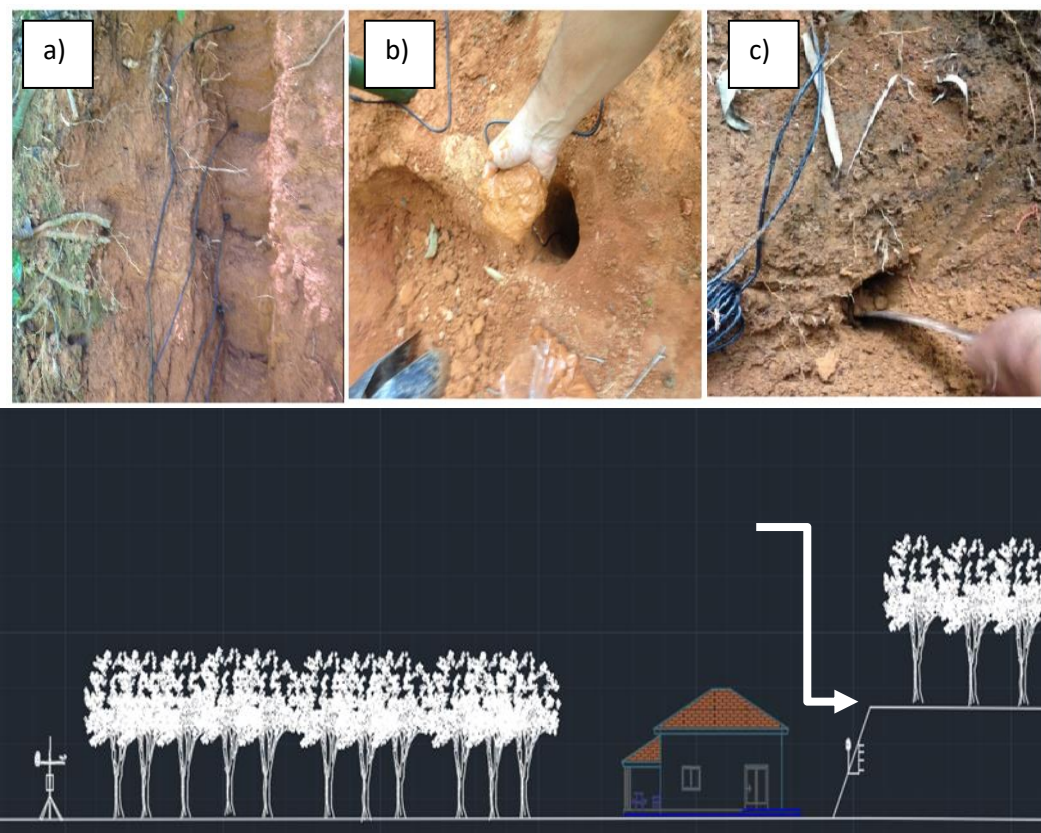


Figure 4.8 - Different installation procedures: driving the rod directly into the soil (a), with mud support (b), and with a hardened steel gauge (c)

Microtomography

In addition, to evaluate the installations techniques and the coupling for EC-5 and the soil particles, a 3D – Microtomography was performed in a dual X-ray tube of a GE (phoenix v|tome|x m) X-ray microfocus system, at the Nuclear Instrumentation Laboratory – LIN/ UFRJ (Figure 4.9).



Figure 4.9 - GE (phoenix v|tome|x m)

The test was realized with just 1 cylindrical soil sample (15 cm – d; 25 cm – h). It was performed because was sought to verify the structural damages in the same material, evaluating the EC-5 field installation procedures (driving the rod directly into the soil, with mud support, and with a hardened steel gauge) and its influences in the soil structure.

The procedure consisted in perform a raw test, regarding to a soil sample without the EC-5 probe. In addition, the *drive in* technique was performed in the same sample and the tomography procedure was realized. Further, the probe was extracted, and the auger was inserted into the ancient boreholes to create a preferred path to the probe introduction. Furthermore, a small hole was created in the core of the sample and with the extracted soil, the material mud was used to install the EC-5 probes.

In addition, the results emphasize that the first procedure (driving into) did not caused problems for the other procedures. The hardened steel gage installing method causes a similar perforation, such as the sensor would be inserted and removed from the soil. I this point, the situation is to perform a pre-hole to insert the EC-5 easily into the soil.

In addition, for the MPS-2, as the installation procedure required a borehole covered by mud, the image acquiring was performed just once.

4.4. Results

The laboratory soil water retention curve was determined by the filter paper method (Marinho, 2006) and fitted by Durner's (1994) model into `swrcfit.sourceforge.net`, presenting a bimodal geometry.

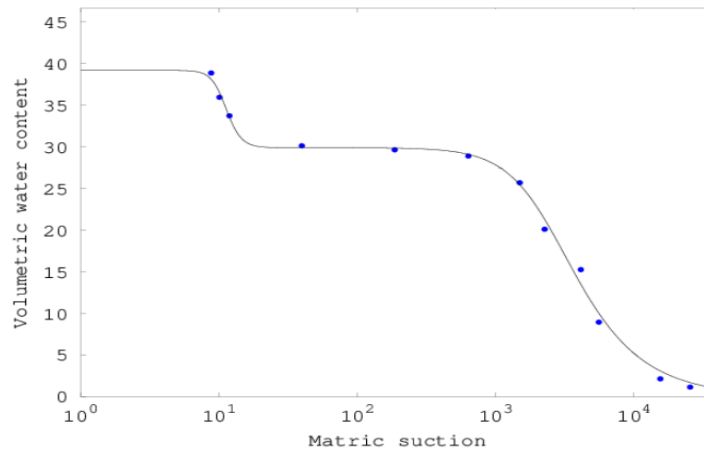


Figure 4.10 - Filter paper laboratory soil water retention curve

In the light of bulk density variation and the EC-5 volumetric water content measured values, the compaction procedures aimed to reach the same volumetric water content and bulk density measured in 10 volumetric rings soil samples results (whereby revealed a 29,13 % of volumetric water content and a Bulk density of 1,82 g/cm³).

The bulk density correlation tests present a strong dependence on the EC-5 volumetric water content data. Regarding the compaction results (Table 4.3 and Figure 4.11), both compaction methodologies (Proctor and double ring) revealed an increase in EC-5 VWC values with an increment in soil specific mass.

Table 4.3 - Compaction methods – VWC EC-5 readings vs. ρ_n

Compaction Test	Acquired Parameters	Compaction Step 1	Compaction Step 2	Compaction Step 3	Compaction Step 4	Compaction Step 5
Hydraulic	VWC (%)	14.1	19.4	24.58	27.02	29.31
	ρ_n (g/cm ³)	1.4	1.57	1.71	1.765	1.81
Proctor	VWC (%)	13.1	18.7	22.5	25.7	28.12
	ρ_n (g/cm ³)	1.42	1.57	1.69	1.76	1.8

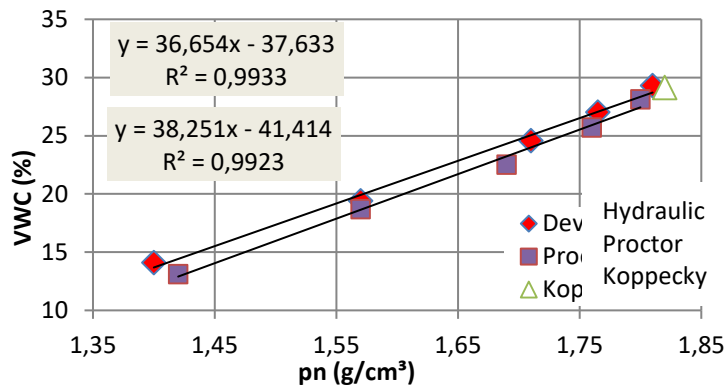


Figure 4.11 - Bulk density and volumetric water content

It is noteworthy to emphasize that the hydraulic system produced a homogenous soil distribution, providing reliable results, protecting the rod of EC-5. Conversely, the compaction performed using the Proctor revealed some rod deformations.

Concerning the Drying procedure (emphasizing it was performed from the top), Figure 4.12 depicts the results for SWRC determination in comparison with filter paper points. The procedures show a strong geometric accordance between the matric potential probe MPS-2 values in comparison with the laboratory filter paper SWRC. However, the results reveal a remarkable difference in the matter of volumetric water content EC-5 probe values (Figure 4.12 – grey line), depicting a vertical adjustment (Figure 4.12 – red line), emphasizing the calibration necessity.

In addition, it is revealed (adjusted – “calibrated”) the limits for reliable readings for the MPS-2. Conversely, even “calibrated”, according to crosschecking with filter paper method, there is a range comprised by not reliable data (red lines)

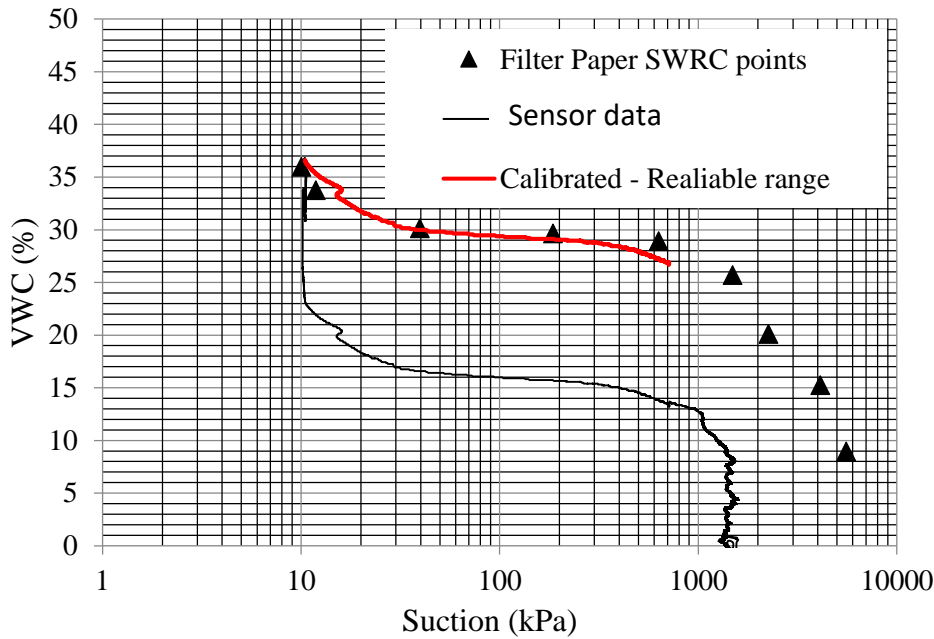
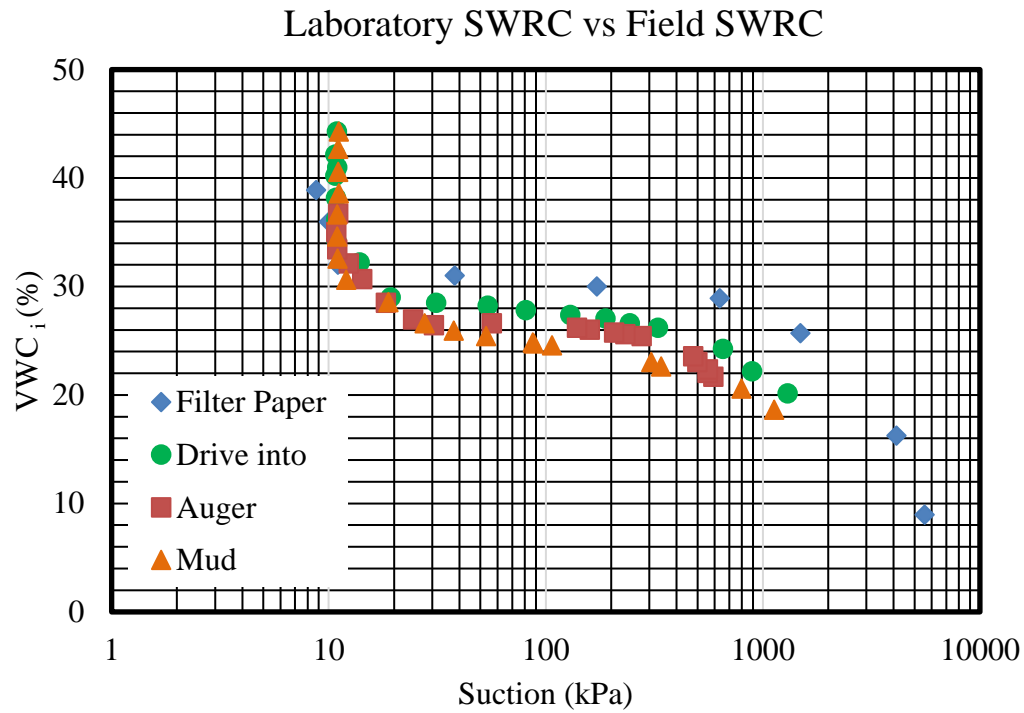
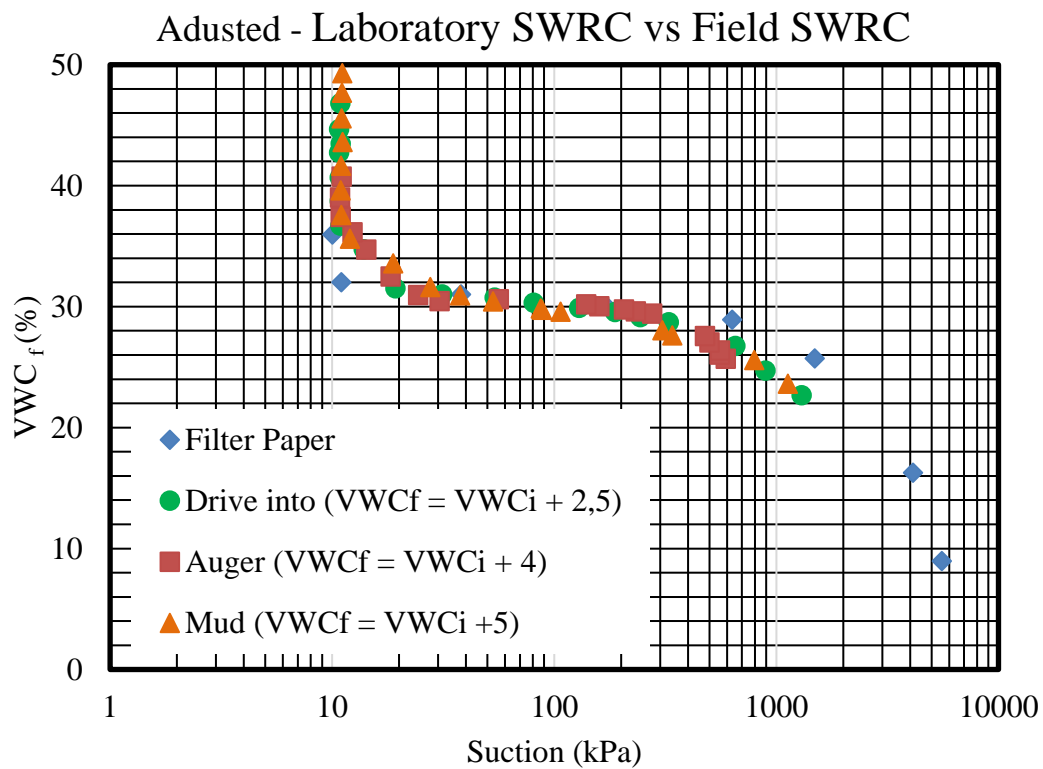


Figure 4.12 - Filter paper vs. sensors readings. EC-5 vertical adjustment and limits for MPS-2

Regarding installation procedures comparison, it is important to emphasize the probes were installed during the summer in a sun-exposed area, in a superficial (0.25m) soil layer. The results depicted a similar geometry (bimodal) for all SWRC performed by the field monitoring equipment's. In addition, was verified a relevant accordance between the laboratory and field values (Figure 4.13 a and b). Further, comparing the installation procedures, the “driving the probe directly” produced the higher correlation with filter paper method, requiring 2.5 % of adjust. Further, even with the Auger and Mud requiring respectively 4% and 5% of adjust, it was proved the curve geometries are well fitted with filter paper geometry.



a)



b)

Figure 4.13 - Comparing installing equipment technics of field soil water retention curve and lab values

When it comes to the microtomography imaging, to visualise the internal structure of the soil and its contacts with the EC-5 probe, 741 layers were rendered (Figure 4.14).

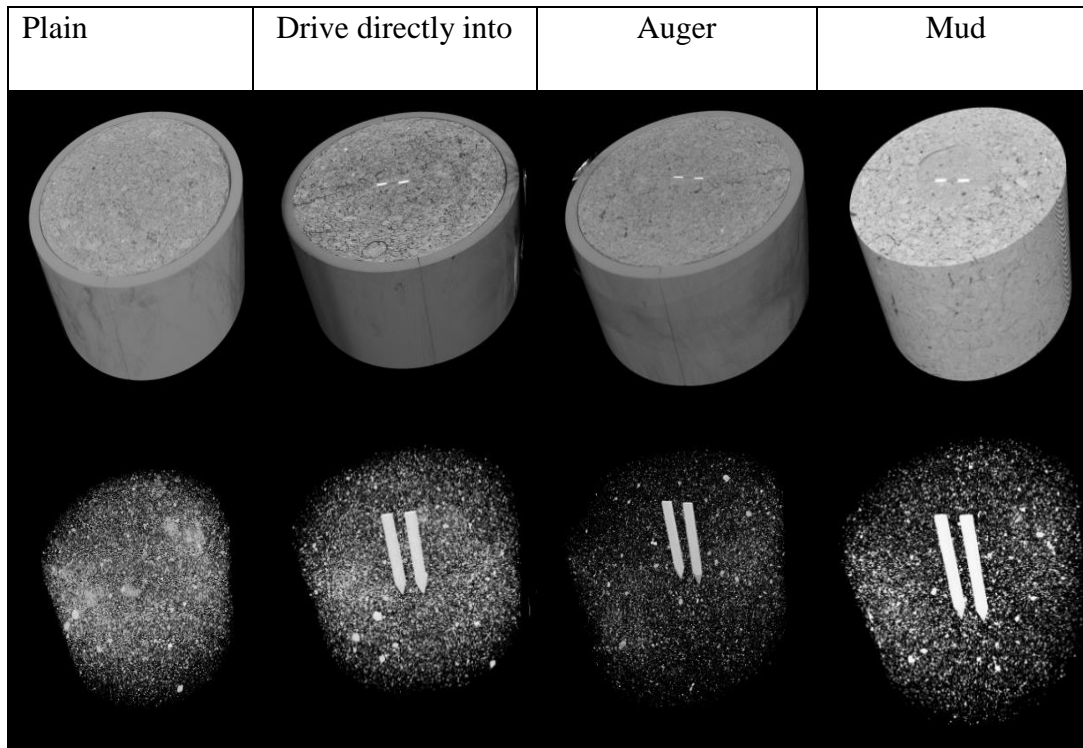


Figure 4.14 - Microtomography images – rendering the first 10 cm height

Concerning the microtomography, the imaging routine is related to parameters calculations such as: surface density; surface area, volume and percentage of closed and opened pores; porosity; and connectivity.

Thus, considering the mud installation procedure caused a relevant structural change into the soil, some cut-offs are required to evaluate the interaction between the soil particles and the EC-5 rods. In this way, the calculations were executed for two different approaches, one comprising of the whole soil sample and another comprising of a small cylinder in the core area (close to the probes).

The measured parameters revealed the volume of 469091, 2 mm³ for total area analysed and a volume of 64378.81 mm³ for the core of the sample. In addition, the object volume, related to the volume of solids (mm³), close, open and porosity values, (related to the voids volume, surface and percentage), and

pore connectivity, (related to the connection between voids) are revealed in the Table 4.4 and Figure 4.15.

Table 4.4: 3D-Microtomography – pore calculations.

Description	Total				Core			
	Plain	Drive-in	Auger	Mud	Plain	Drive-in	Auger	Mud
Solids - object volume (%)	72,25	70,55	74	73,44	70	68,71	69,31	71,83
Closed porosity (%)	1,12	1,01	1,46	1,52	0,9	1	1,02	1,77
Open porosity (%)	26,93	28,44	24,58	25,04	29,1	30,29	29,67	26,4
Total porosity (%)	28,05	29,45	26	26,56	30	31,29	30,69	28,17

3D-Microtomography

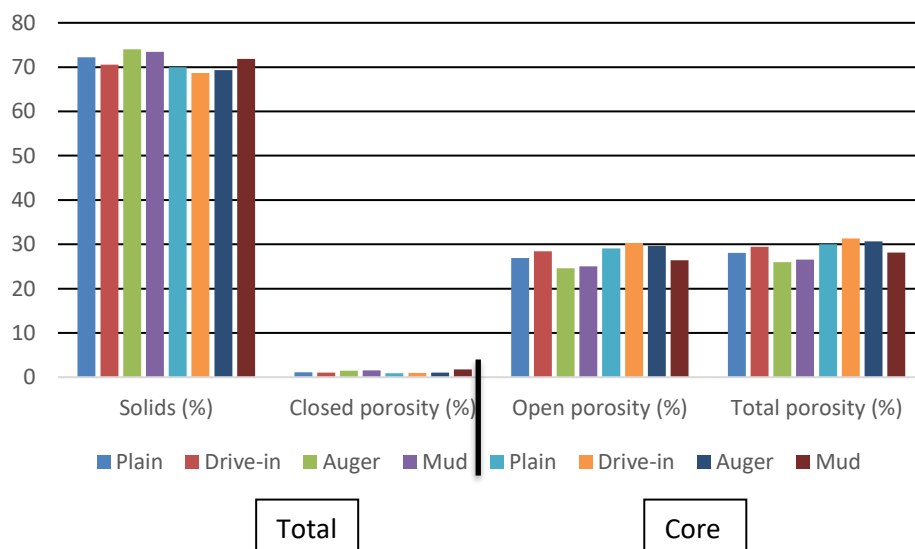


Figure 4.15: 3D-microtomography pore calculations.

Regarding the qualitative analysis, Figure 4.16 reveals the top and transversal cut-offs for the same orientation and areas of the undisturbed sample and for the samples submitted to the installation procedures.

Comparing drive into and auger techniques, the used resolution verified only one (parallel to the probe) structural change due the installation's procedures. However, the comparison between field and laboratory soil water retention curves suggest that additional changes occurred into the soil structure.

In the matter of mud injection technique, a contrast zone and new voids were revealed into the mud area and into the undisturbed area.

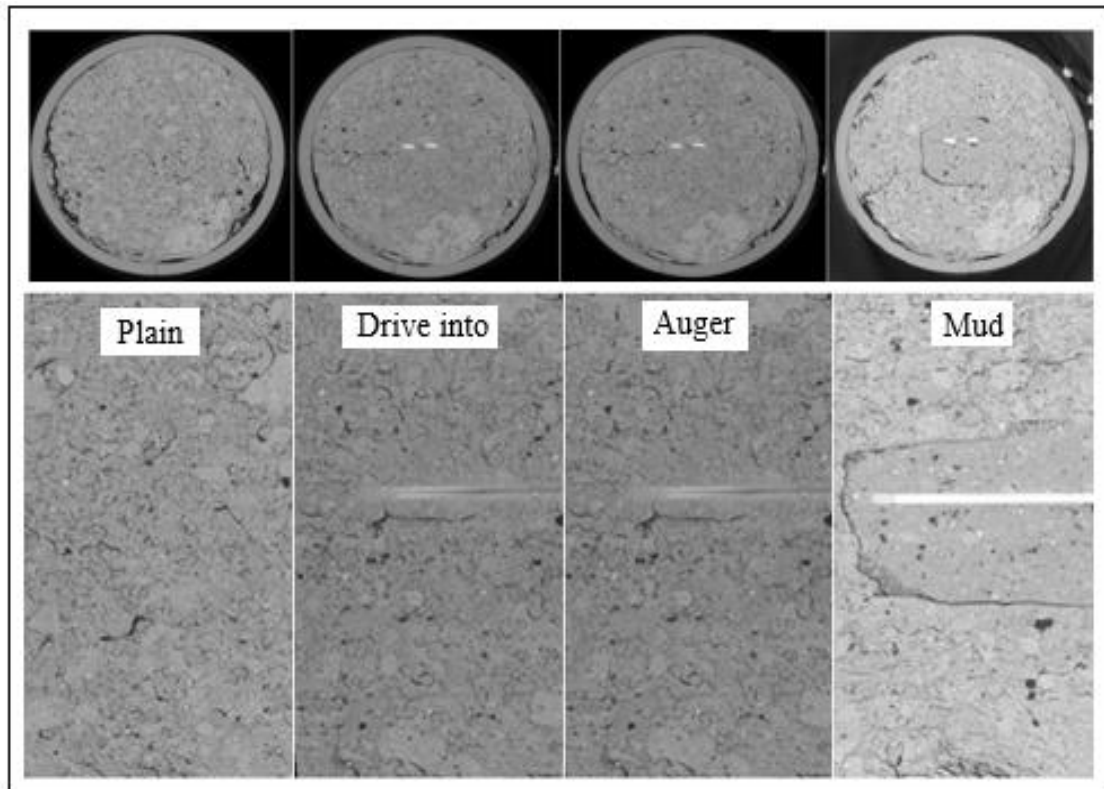


Figure 4.16 - Tomography images. Interaction between the probe and the ground

Concerning the mud injection installation procedure, it is important to emphasise that the contact between the mud and the undisturbed soil presented a void disruption, suggesting that it was responsible for the difference observed with the filter paper method.

Regarding the drive in and the auger procedures, it was not possible to verify differences in the soil structure (Figure 4.16) that justify the behaviour disposed in the field soil water retention curves. Due to this, another tomography routine was performed in a unique soil sample with a 3.8 cm diameter and 7.6 cm height, to obtain a higher resolution (75 μm) analyse of the interaction between the sensor installing techniques and the soil structure.

The new images (Figure 4.17) revealed some differences between the drive into (b) and auger installation (c) procedures. The auger created voids in the contact of the probe. Thus, the divergence between field soil water retention curve is justified because the air, water, and the solid matrix have different electrical conductivities.

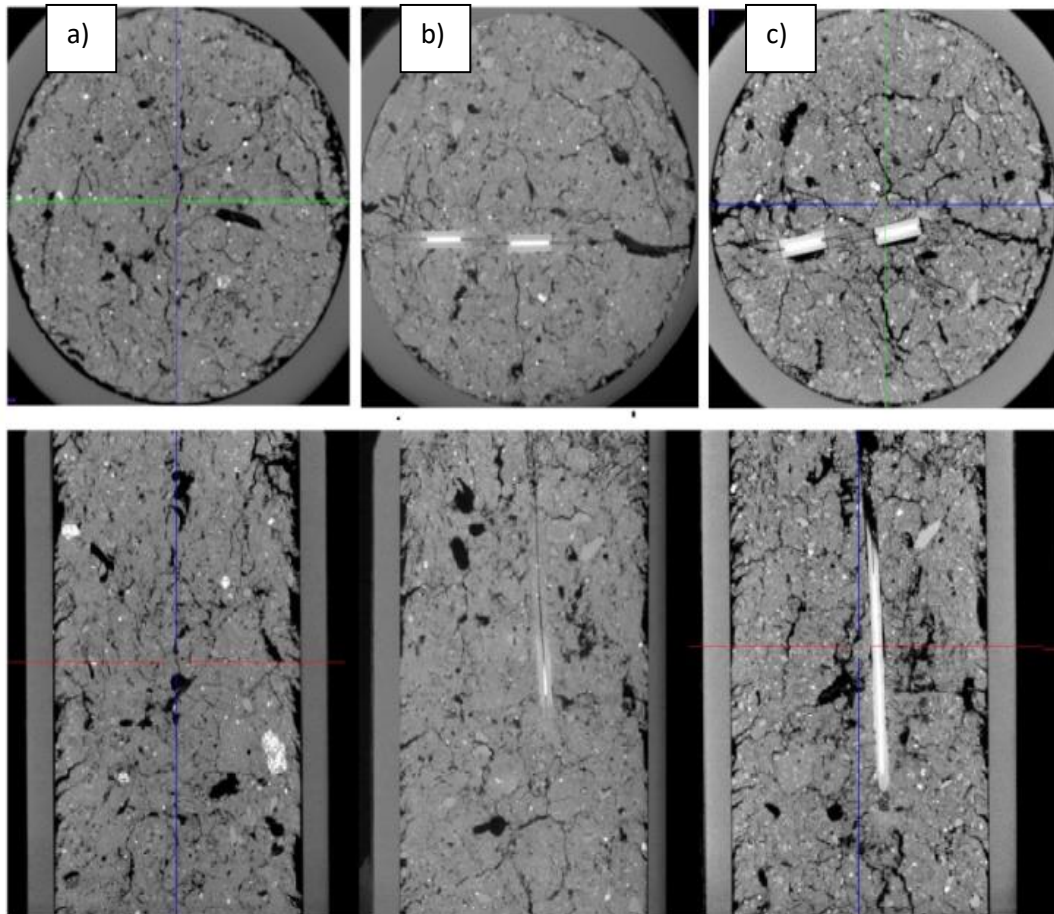


Figure 4.17 - Higher resolution microtomography images

4.5. Conclusions

The probes' calibration emphasised that the EC-5, manufactured by Decagon Devices Inc., is strongly dependent on the material's bulk density, and, because of this, when the equipment is submitted to an installation procedure, it can produce unreliable volumetric water content data.

Additionally, to produce a reliable field SWRC, the MPS-2 does not need to be calibrated because the obtained values were well-fitted to the filter paper soil water retention curve. In this way, the key elements to achieve accurate data production are to perform a field adjust ("calibration") and to conduct a careful installation procedure of the EC-5 probes.

The tomography images depict that the use of the auger to install the probes in hard soils can cause some voids in the probe-soil contact. It

underestimates the measured values of volumetric water content. The same behaviour occurred for the mud-based installation. Due to structural changes, the electrical permittivity altered, and the results were affected.

Although directly driving the rod into the soil has been the installation procedure that presented values closest to the laboratory results, it is important to emphasise that the brittle rod cannot be used for hard soils because it can cause damage to the sensor and wrong VWC values.

Finally, it is important to note the EC-5 sensor is extremely sensitive to installation techniques, requiring field calibration for different techniques in each installation point. Regarding this, the tested procedures (direct installing, auger and mud) revealed the same characteristics and underestimated the water content by 2.5%, 4%, and 5%, emphasizing the *Drive in* installation technique as the better procedure for a field monitoring with the material.

5

Soil-atmosphere interactions: Using field monitoring to evaluate matric suction transient features

Abstract

This Chapter deals with an analysis of transient atmospheric parameters and their interactions with volumetric water content and matric suction in 0.25 m, 0.50 m, 0.75 m and 1 m depths of an unsaturated colluvial soil from Tinguá, Rio de Janeiro, Brazil. The methodology includes performing a long-term 4 years of continuous field monitoring for meteorological parameters and pointing out their interaction during different events, characterised by distinct rainfall patterns. To conduct this analysis, a Campbell weather station was used to obtain the atmospheric/meteorological data. For the soil analysis, EC-5 frequency domain reflectometry probes were used to obtain volumetric water content data, and MPS-2 sensors were used to obtain matric suction data. Further, for the thunder-soils analysis, was performed a cross-referencing data of thunderstorm days (depicted by satellite lightning detection network, STARNET) and a refined 1-minute sampling rate of matric potential. The results indicate that soil-wetting and drying processes are also dependent on atmospheric conditions such as relative humidity and air temperature. Thus, rainfall cannot be the only parameter used to evaluate long-term soil-water moisture change processes. Conversely, lower matric suction values are related to the summer months in Rio de Janeiro, emphasising the effect of rainfall in inducing higher degrees of saturation for a long time. Finally, no rapid changes of matric potential or volumetric water content values were observed with the used sensors during thunderstorm events and monitored lightning occurrences.

Impact factors: Soil-wetting and drying processes are also dependent on atmospheric conditions such as relative humidity air temperature, and thus, rainfall cannot be the only parameter used to evaluate the long-term soil saturation processes.

Keywords: Rainfall, unsaturated soil, matric suction, field monitoring

Introduction

The endeavour of environmental analysis increasingly demands real-time soil and climatological field monitoring data due to many impact factors, which include material damages, economical losses or even human death.

In the light of environment complexity, Antunes *et al.* (2015) emphasises that the soil physic-mechanical behaviour must not be disconnected from environmental aspects as the material properties evolve from geological patterns and are dependent on geomorphological processes and climate exposure.

The geotechnical approach in climatology is usually coupled with rainfall studies, focussing mainly on statistical data and the possibility of climatic-atmospheric events that occur with the same characteristics more than once in a specific site. In addition to being a relief sculpting agent, the climate approach has a key role in geotechnical analysis once it can be associated with the available water in the soil and dry-wetting cycles.

A large number of authors has dealt with subjects relating soil-climate interactions. For instances, Reichardt (1990) and Bertolino (2004) considered soil dry-wetting effects on vegetation quality. Vargas (1971), Lumb (1975), Brand (1984), Gerscovich *et al.* (2006), Lim *et al.* (1996), Faisal (2000), Toll *et al.* (2011) and Springman *et al.* (2013), among others, considered erosion processes and landslide occurrences due to rainfall and soil suction variations. Topics such as the interaction of soil water content and wind speed (Li *et al.*, 2006); influence of the background wind on the local soil moisture (Froidevaux *et al.*, 2014); effect of wind speed on evaporation from soil (Davarzani *et al.*, 2014); climatic effects on the soil suction and water content changes (Bicalho *et al.*, 2014) and evaluation of air-soil temperature relationships (Wang *et al.*, 2016) have also been dealt with. Bordoni *et al.* (2014) emphasises the multiple interactions between soil-climatic parameters resulting in decreased safety of slopes. However, more than one hydrologic cycle of field monitoring of rainfall and other weather variables has not been performed to verify maximum and minimum scenarios and understand related changes in water potential or matric suction.

The key aspects considered in the development of this Chapter are related to combining long-term field monitoring data (moisture/suction and atmospheric parameters) to evaluate the interaction of different soil saturation scenarios in a colluvial soil from Tinguá, Nova Iguaçu, Rio de Janeiro, Brazil (PUC-Rio – Tinguá Experimental Campus).

The main goals of this particular study are:

- Analysing the changes that occur in matric suction during different atmospheric conditions;
- Verifying the depth of the meteorological daily-influence on the soil; analysing the time scale effect (daily, monthly or yearly) to verify rainfall-suction patterns;
- Evaluating the matric suction during thunder occurrences.

For this, the current Chapter comprises five steps: Providing the environmental background, material characterisation, methods (field monitoring devices and procedures), results and conclusion.

5.1. Environmental background

The first relevant procedure is the environmental background survey. It is important to consider some atmospheric patterns in tropical areas such as Rio de Janeiro as they are relevant to the environmental-geotechnical analysis. The most commonly observed patterns include thunderstorms every summer season, orographic rainfall according to relief geometry and cold fronts entrances from autumn to winter.

Brazil's geography has a complex diversity as the country has a continental size with several geologic, geomorphologic and climatic influences. Based on a regional approach, the Rio de Janeiro state has a landscape that originated from two distinct tectonic events: The first, related to the collisional movement between Africa and South America that created an orogenetic mountainous system, is named Serra do Mar. The second, related to the disruption of the Gondwana supercontinent, created the Atlantic Ocean and faulting processes of the South American coastal rocks. Over geological time, comprising thousands of millions of years, many magmatism, folding and faulting processes

occurred, and a relief landscape emerged due to the exposure to the new temperature, pressure and climatic conditions (Schobbenhaus, 1984).

The sampling for this study took place in Tinguá, Nova Iguaçu municipality, RJ – Brazil. It is located under the UTM coordinates -22.540335, -43.504472, inside the 23k zone, considering the WGS-84 DATUM. The research was conducted inside the Tinguá PUC-Rio Experimental Campus at 62 meters above sea level. The surrounding area belongs to the Rio Negro geological Unity, comprised by Biotite-Gneiss (Migmatite) and the Foliar-Granite (Granite-gneiss) lithologies.

Based on the climate characterisation, the area is classified as an Awa according to the Köppen Climate Classification. The annual average temperature is between 15°C and 23°C, with a rainfall index between 1500 mm and 2600 mm during the summer season.

Based on the rainfall characteristics, three atmospheric events play a significant role in the soil saturation and runoff processes: Convective/Thunderstorms, Cold Frontal System and Hot Frontal System.

- Thunderstorms – they happen during the hot summer days when moisture increases as a result of the evaporation process (by the Atlantic Tropical Mass), causing a convective system on the Baixada Fluminense site and, as a result, creating *cumulus nimbus* clouds. The current direction is from the ocean to the continent.
- Cold Frontal System – it takes place mainly in the autumn when the Atlantic Polar Mass is potentialized and evolved from the south in lower levels and charges electrically during the instability, causing rainfall as a result of the contact with hot mass and lightning at its core. The current direction is from the south of South America towards the north, with a strong influence on the Brazilian east littoral.
- Hot Frontal System – it develops when the Continental Equatorial Mass is pushed through the intertropical zone, crossing over the country and reaching the southeast with a high humidity mass. The current direction moves from the Amazon to the southeast in a diagonal path (NW-SE).

It is important to emphasise that the dried period never happens during the Summer - December, January, February and the beginning of March. These months are related to the main rainfall period that presents remarkable events such as flood and landslides.

5.2. Soil characterisation

The studied material is an unsaturated colluvial soil, extracted from a soil profile in a cut slope. The sampling depths were: S1 – 0.25 m; S2 – 0.50 m; S3 – 0.75 m; and S4 – 1.0 m. The physical index, obtained by mass-volume calculations, are presented in Table 5.1. For the Atterberg limits, w_L and w_P , the NBR 6459/84b and NBR 7180/84c standards were used, with the Activity Index (AI) being given by the Skempton's equation. It is important to note that, even with the depth increase, the results were quite similar, suggesting that all the samples belong to the same mass transportation event disposed at the area during the same time interval.

Table 5.1 - Physical Index of the samples

Sample	Value	Gs	ρ_n (g/cm ³)	ρ_d (g/cm ³)	w_{nat} (%)	e	n (%)	S (%)	w_L (%)	w_P (%)	PI (%)	AI
S1 0.25 m	Max.	2.69	1.66	1.30	24.35	1.06	51.57	62.4	65.7	39.3	26.4	0.50
	Min.		1.62	1.34	24.01	1.01	50.24	61.6				
	Av.		1.64	1.32	24.18	1.04	50.90	62.0				
S2 0.5 m	Max.	2.69	1.55	1.22	25.74	1.21	54.77	58.2	61.1	38.3	22.7	0.54
	Min.		1.53	1.26	23.35	1.14	53.29	52.8				
	Av.		1.54	1.24	24.545	1.18	54.03	55.5				
S3 0.75 m	Max.	2.72	1.61	1.21	22.35	1.25	53.29	52.2	56.8	12.3	44.4	1.16
	Min.		1.48	1.32	21.91	1.06	54.03	51.2				
	Av.		1.545	1.27	22.13	1.15	53.49	51.7				
S4 1 m	Max.	2.67	1.62	1.23	22.85	1.17	51.45	55.4	33.4	27.3	6	0.44
	Min.		1.51	1.33	21.97	1.01	53.49	53.3				
	Av.		1.565	1.28	22.41	1.09	52.11	54.3				

For the grain size distribution (Table 5.2), the NBR 7181-1984 method was used. These results, along with the Atterberg Limits, present a sandy-clay CH soil (for S1) with a gradual transition to a Clay-Sandy SC soil (for S4).

Table 5.2 - Grain size distribution (GSD)

GSD (%)		S1	S2	S3	S4
Boulder		0.49	1.74	2.50	3.21
Sand	Coarse	18.36	22.38	20.96	29.48
	Medium	12.67	9.77	12.59	16.03
	Finer	6.97	8.47	9.96	18.73
Total Sand		38.00	40.62	43.51	64.24
Finer	Silt	8.23	14.87	14.87	17.81
	Clay	52.97	41.96	38.35	13.65
Total Finer		61.20	56.83	53.23	31.47

Although the results shown in Table 5.1 suggest that the colluvium is relatively homogeneous, those shown in Table 5.2 indicate a clear trend of increase of the sand fraction and decrease of the finer fraction with depth, suggesting that the saturated permeability of the material may increase with depth. In such a case, rainwater infiltration at the site essentially would comprise vertical water flow.

The soil water retention curve (SWRC) for all samples were determined using the filter paper technique (e.g. Marinho, 2006), with samples being moistened and dried from the field water content, as suggested by de Campos *et al* (2006).

Figure 5.1 shows the data points of the SWRC obtained for all the four sampling depths. The results present the volumetric water content (%) versus suction (kPa) values for the soils. The main general characteristic is the bimodal geometry observed in all samples (Figure 5.1).

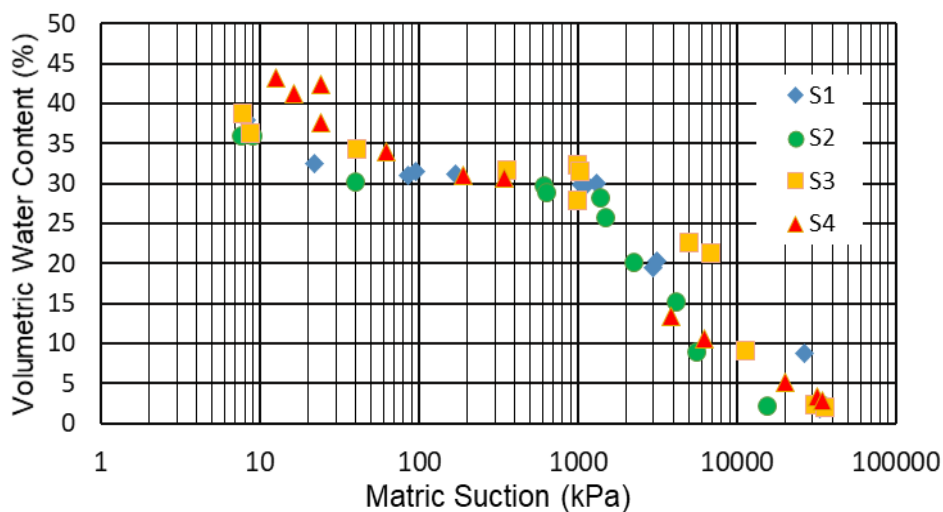


Figure 5.1 - Filter Paper Method – Soil Water Retention Curve (SWRC)

Considering all the points on the same SWRC, it is possible to verify that the macro pores air-entry is related to low suction values (~30 kPa), highlighting how the desaturation values start with low suction increments. The second air-entry values are related to the micro pores and demonstrate high suction values (~1500 kPa).

5.3. Field monitoring

The field monitoring was performed from January of 2014 to December of 2017. Regarding this, a Campbell compact weather station (CWS) was used for obtaining meteorological parameters and Decagon's probes were used for measuring volumetric water content and matric suction during soil analysis. The figure 5.2 presents all the equipment and highlights their measured parameters and resolutions.

	<p>Pyranometer PYR-Apogee CS-300 – Solar Global Radiation parameter – W/m^2 – Resolution $10^{-5} W/m^2$.</p>
	<p>Thermo-Hygrometer CS-215 – Relative Humidity parameter – % RH – Resolution 10^{-3} %RH.</p>
	<p>Anemometer Wind Sentry 3002-5 – Wind Speed/Direction – m/s and °NW - Resolution 10^{-5} m/s and 10^{-5} °NV.</p>
	<p>Pluviography I2H – Rainfall parameter – mm – Resolution 0,254 mm.</p>
	<p>Datalogger model CR200 – 128 kb internal memory – 5 analogic data channels – 2 pulse channels – 2 control ports – serial port RS232.</p>
	<p>Barograph – External Probe – model TRP Resistive – Air Pressure parameter – Resolution 0,1% F. E.</p>
	<p>Probe EC-5 - Decagon Devices – Volumetric Water Content parameter – Based in the soil dielectric permittivity – Range 0 to 100 % - Resolution 0,001 m^3/m^3 - Dimension 8,9 cm x 1,8 cm x 0,7 cm – Working temperature 0 to 50 °C.</p>
	<p>Probe MPS-2 - Decagon Devices – Matric suction and temperature parameters – Range -10 kPa to -500 kPa (Decagon highlights that this probe can reach values up to -1000 kPa).</p>
	<p>ECRN 100 - Decagon Devices – Rainfall parameter – Resolution 0,2 mm.</p>
	<p>Em-50 - Decagon Devices – Datalogger – 5 Reading Channels</p>

Figure 5.2 - System used for soil moisture monitoring

The weather station and the soil monitoring apparatus are distant in 200 meters long each other (Figure 5.3). The coordinates are $-22.589454^{\circ}/-43.406852^{\circ}$ for the Campbell equipment and $-22.590410^{\circ}/-43.405083^{\circ}$ for Decagon apparatus. It is important to emphasize that ECRN 100 was installed on the EC-5 and MPS-2 place. In addition, even surrounded by vegetation, the EC-5 was strategically installed in an area clear of trees and because of this, both pluviographic equipment (ECRN 100 and I2H) presented the same rainfall values.

Furthermore, no soil contraction was observed.

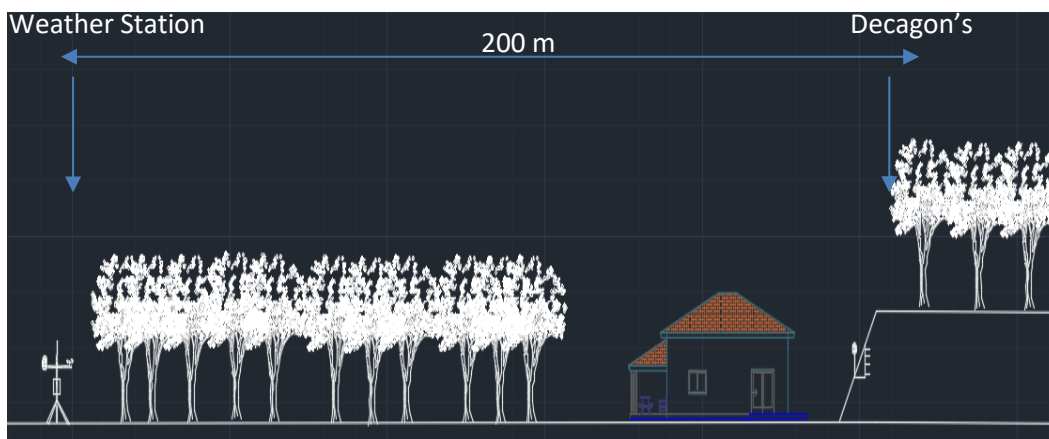


Figure 5.3 - PUC-Rio, Tinguá Experimental Campus

In the matter of data acquisition, 10 and 15 min were used as sampling rates. Further, the EC-5 and the MPS-2 probes were installed in four different depths (0.25 m, 0.50 m, 0.75 m and 1 m) using the drive-in technique for the EC-5 and a hole filled by “mud” for the MPS-2. For the ECRN 100, the equipment was placed in the sampling point one meter above the soil.

It is important to emphasize that the EC-5 sensors presented a remarkable disruption of data and because of this it will not be revealed in the long-term field monitoring graphs. However, isolated values recovered during the events will be presented in the correlation of field and laboratory data.

5.4. Results

The results are disposed in sections such as: Rainfall vs water potential vs soil temperature analysis; Correlation between rainfall, water potential, volumetric water content, air temperature, soil temperature, relative humidity, solar radiation,

wind speed and wind direction; Correlation between field and lab values of water potential/volumetric water content for S1; Thunderstorm days vs water potential – refined data acquisition data.

In terms of the probes' responses to the increasing depth, the MPS-2 installed at 0.25 m below the surface was the first probe to show changes in values with rainfall incidence. In addition, the deeper probes required more time to be influenced by rainfall, suggesting a mainly vertical seepage condition.

The first analysis is comprised of a four-year long field monitoring of rainfall, matric suction and soil temperature, revealing seven principal Events (represented by the maximum to minimum amplitude of water potential values between two rainfall occurrences).

Rainfall vs water potential vs soil temperature

During the year of 2014 (Figure 5.4 – a, b, c), three events were verified with maximum amplitudes.

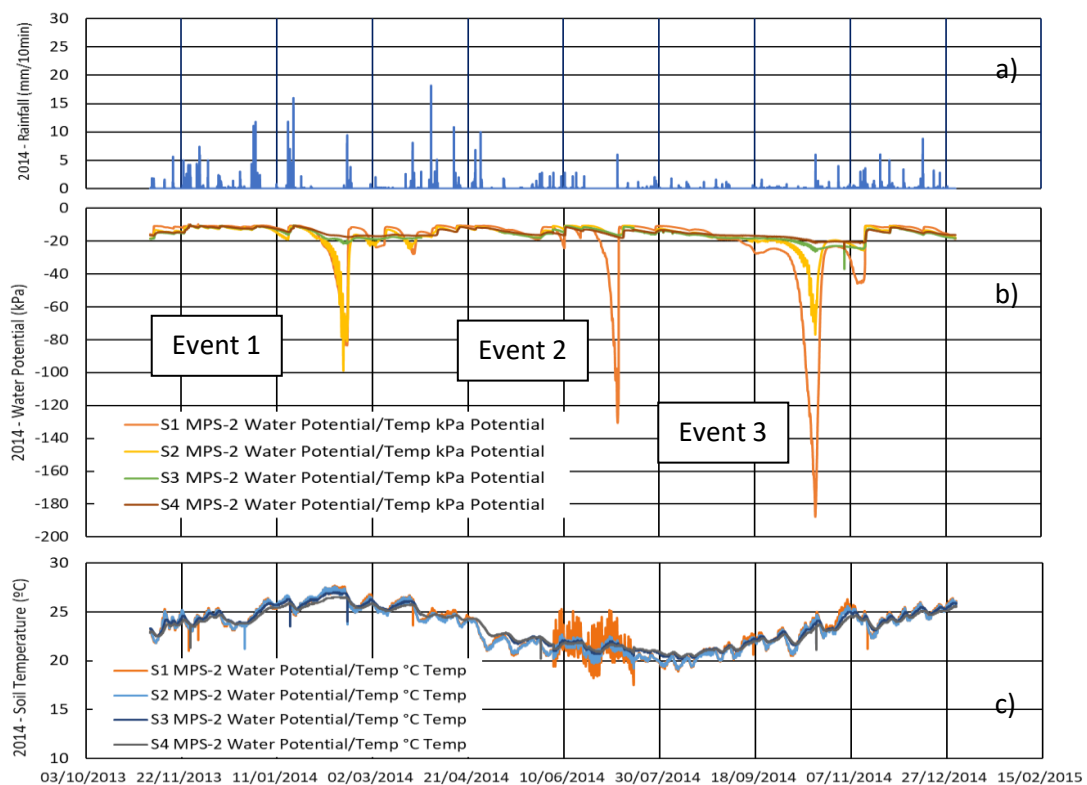


Figure 5.4 - Correlation between rainfall, matric potential and soil temperature - 2014

The first, Event 1, occurred in February and the probes installed at 0.25 m and 0.50 m reached -100 kPa of matric suction. In the matter of Event 2; the matric suction of 25 cm probe reached -120 kPa during a smaller time interval, suggesting the existence of further drying mechanisms dependent on temperature due to the intense day/night soil temperature variations shown in Figure 5.4 – c. In the matter of Event 3, all the probes, installed at 0.25 m, 0.50 m, 0.75 m and 1.0 m depths reached different values at different times. This period is related to the end of the dry season (Figure 5.4 – a), revealing a slower transition period for the distribution of matric suction throughout the monitored depths.

The year of 2015 (Figure 5.5 - a, b, c) could not be fully analysed due to the occurrence of data disruptions as a result of problems with the probes and the acquisition system. However, one event with maximum amplitude was documented.

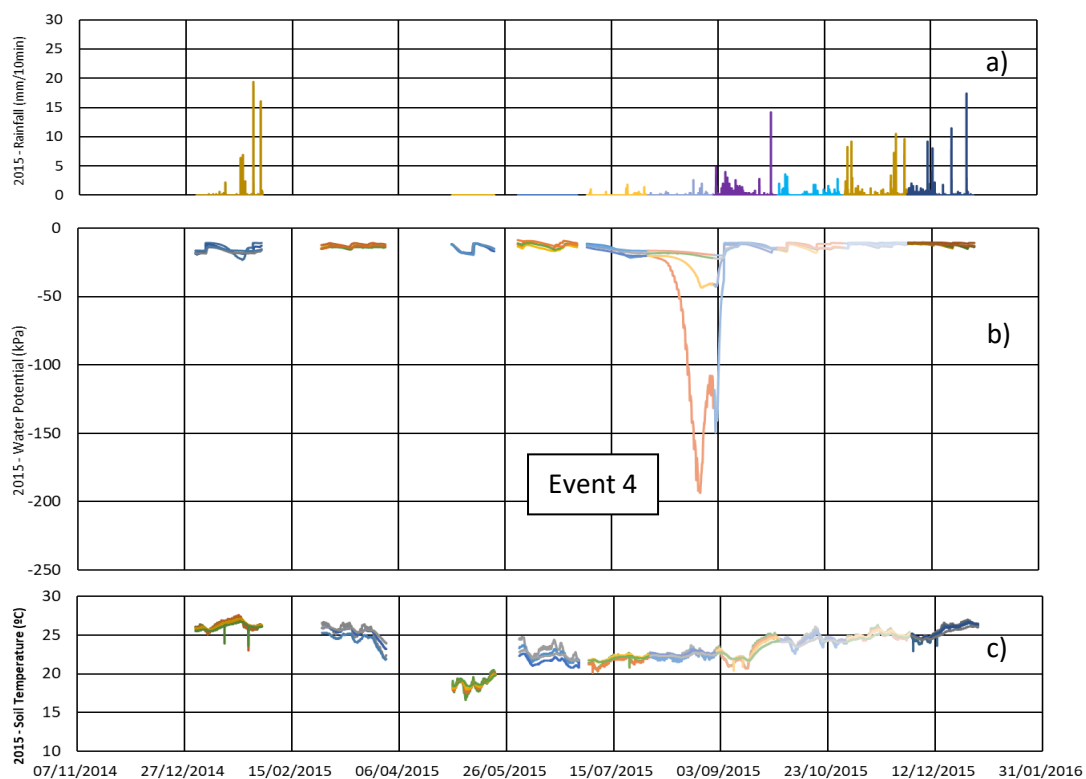


Figure 5.5 - Correlation between rainfall, matric potential and soil temperature - 2015

Event 4 occurred in August/September and reached -190 kPa of matric suction at 0.25 m and -40 kPa at 0.50 m of the MPS-2 installation point's depth. This suggests that the time interval between rainfalls was not enough to dry the

layer below the 0.25 m depth. Further, all the probes, installed at 0.25 m, 0.50 m, 0.75 m and 1.0 m reached different values at different times (similar with Event 3) depicting a gradual transition of matric potential values.

During the year 2016 (Figure 5.6 – a, b, c), the channel at 0.5 m was lost, and because of this, the values for this layer could not be analysed. However, two events with maximum amplitudes were verified.

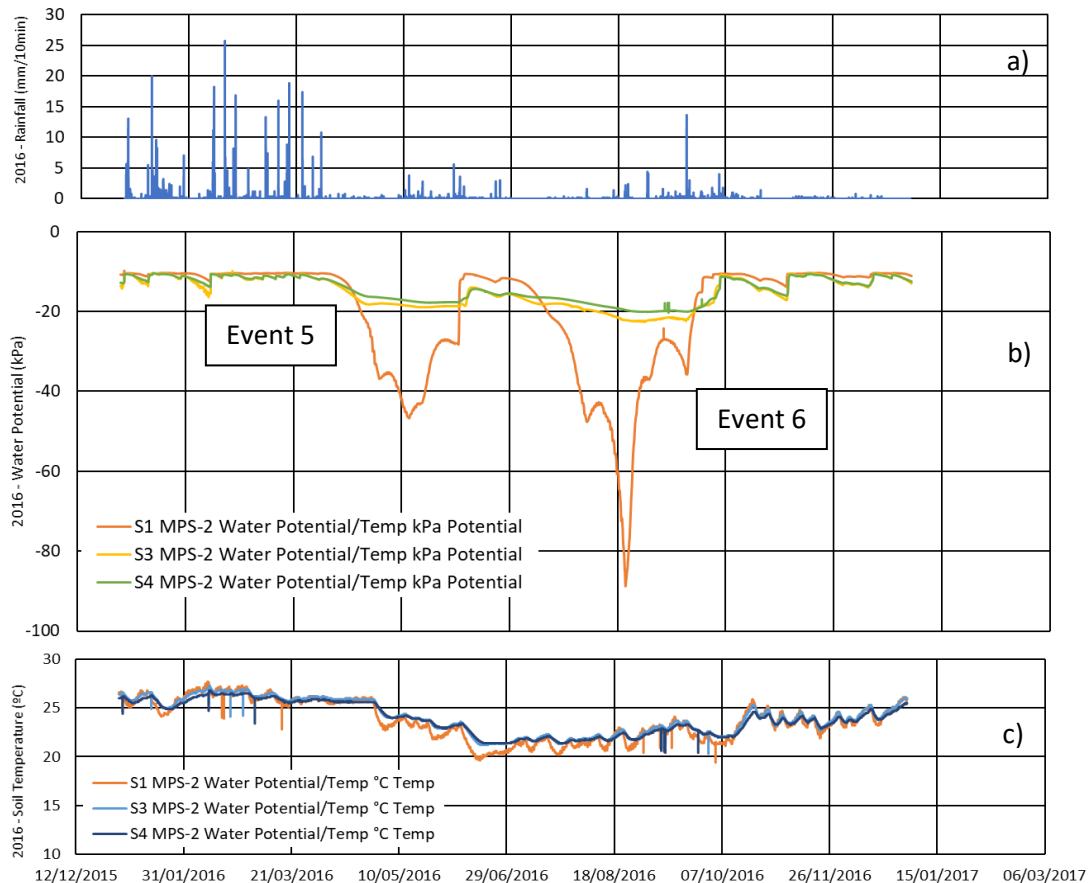


Figure 5.6 - Correlation between rainfall, soil temperature and suction – 2016

Event 5 began in April, and by May, the matric suction at the 0.25 m MPS-2 installation point had reached -45 kPa. Following that, Event 6 began at the end of June, and by August, the matric suction reached -85 kPa at the same depth.

That year presented a remarkable rainfall season until March, and because of this, the main changes in matric suction during March and August revealed a maximum of -10 kPa of matric suction variations for the 0.75 m and 1.0 m depths. This emphasises the relevance of the superficial layer (0,25 m) in the interaction of matric potential and rainfall patterns.

The last year analysed was 2017 (Figure 5.7 – a, b, c). That year had a stable period until the end of July when the maximum suction values (Event 7) were reached by the end of the dry period.

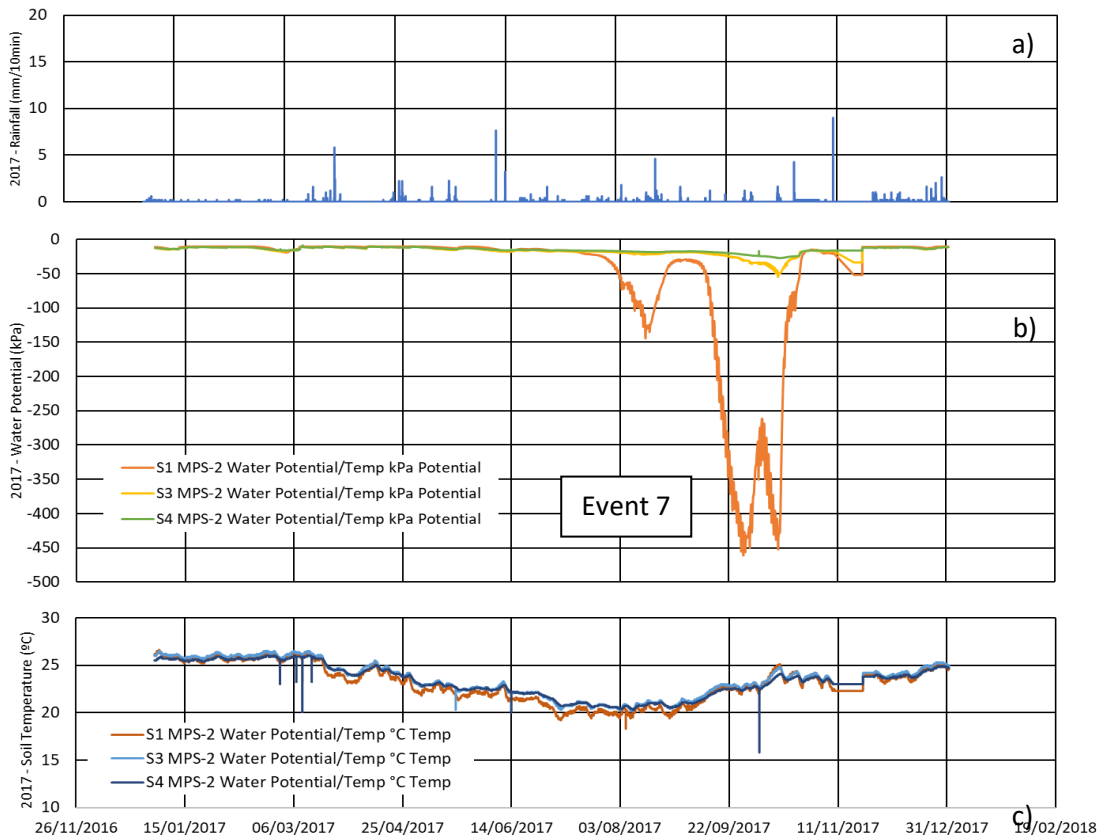


Figure 5.7 - Correlation between rainfall, water potential and soil temperature – 2017

In the light of rainfall, higher values were obtained during December, January and February, with the exception of the year of 2017 as this period did not follow the same behaviour.

The matric water potential reached -450 kPa and did not demand heavy rainfall values to reach the same matric suction values of the probes installed into 0.75 m and 1.0 m depths.

In the light of rainfall, the values obtained at the beginning of the year must be analysed in order to produce a reliable and confident result. This period was influenced by La Niña, and because of this, the rainfall characteristics were changed from high magnitude peak events to low peak values with persistent characteristic events that remained in this pattern until March 2017.

Correlation between soil matric suction and atmospheric parameters

To demonstrate the correlation between the atmosphere, matric potential and volumetric water content, the results for the events 1 are presented in the Figure 5.8, from item a to h.

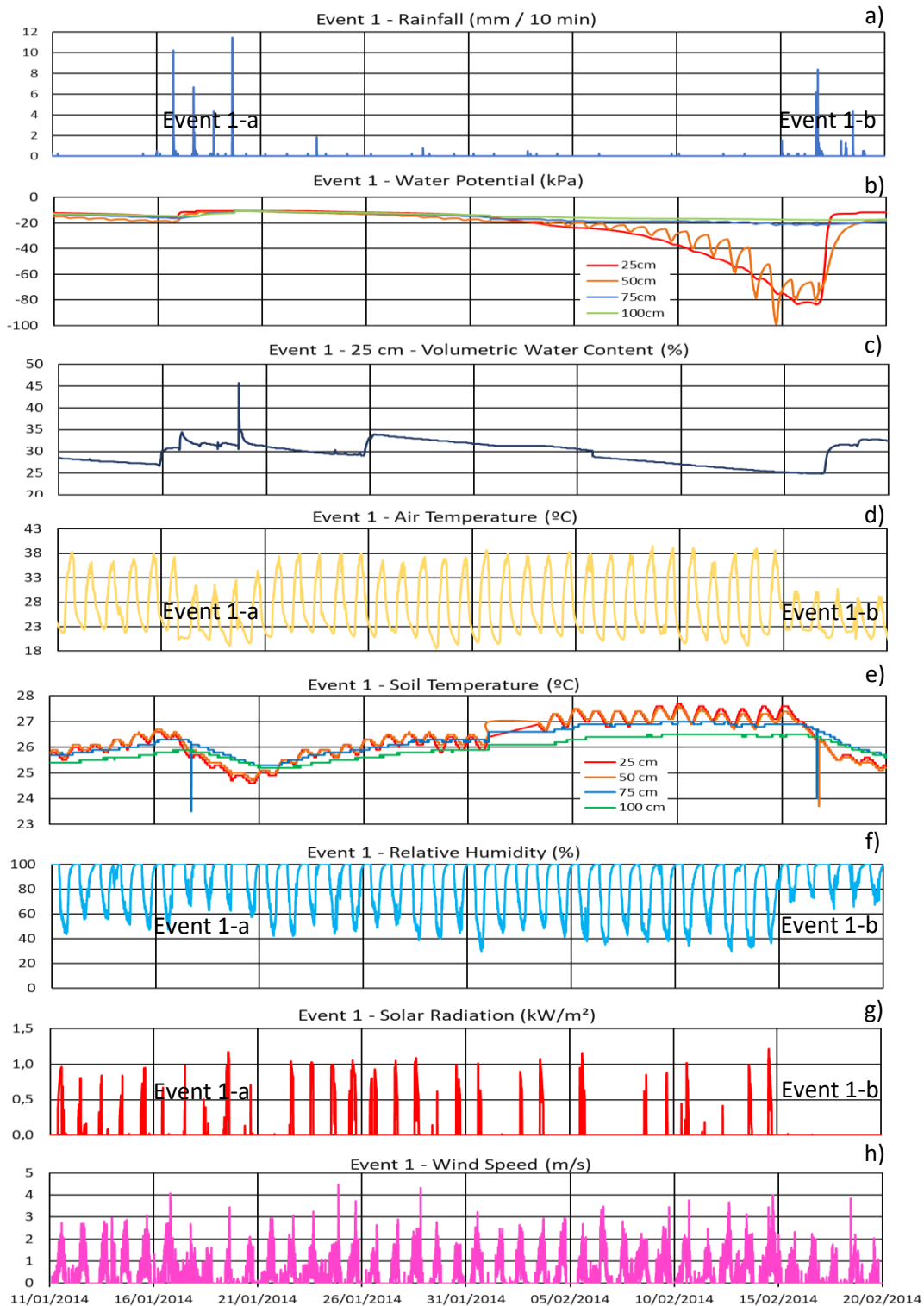


Figure 5.8 - Correlation between atmospheric and soil data – Event 1

In terms of rainfall, it is remarkable that there is a main dry season between June and July characterised by the wintertime in Rio de Janeiro. While the summer period, occurring from December to March, comprises the higher cumulated values.

The matric suction depicted a daily variation for the superficial (0.25 m and 0.50 m) probes, presenting some oscillations during the drying. This fact was not observed during the wetting, suggesting that the porous stone is moistened and dried under different conditions.

The meteorological approach points out that the air temperature results ranged between 18 and 39 °C, comprising the lower temperature between June and July. Concerning the soil temperature, a variation of 3 °C was verified from 24.8 °C to 27.8 °C at 0.25 m and 0.50 m depths. However, for 0.75 m and 1.0 m depths, the variations were much lower.

By correlating relative humidity and matric potential, it was possible to observe the interdependence of the beginning of the desaturation process with the decrease of relative humidity. According to this, lowers values of matric suction are also dependent on this parameter.

Concerning solar radiation parameters, Event 1-a and Event 1-b revealed the correlation with rainfall types once a long reduction of solar radiation was depicted by a frontal cold system. On the other hand, the convective rainfall did not cause pattern changes.

Finally, wind speed and wind direction did not presented correlations with matric potential changes.

Correlation between field and laboratory

For the correlation between field equipment and filter paper laboratory SWRC, was used the MPS and EC-5 sensors to reveal the maximum and minimum valued of water potential and volumetric water content of the seven events. The results are disposed in the Table 5.3 and in the Figure 5.9.

Table 5.3 - Time-interval used for correlation

		Water Potential (kPa)		Volumetric Water Content (%)	
Event 1	1dry	15/02/2014	-83,5	16/02/2014	27,15
	1moist	17/02/2014	-14,5	17/02/2014	32,65
Event 2	2dry	08/07/2014	-130,7	10/07/2014	33,75
	2moist	10/07/2014	-12,1	11/07/2014	38,15
Event 3	3dry	19/10/2014	-187,7	21/10/2014	26,55
	3moist	25/10/2014	-25,3	25/10/2014	29,05
Event 4	4dry	05/09/2015	-193,8	14/09/2015	26,89
	4moist	25/09/2015	-14	25/09/2015	29,55
Event 5	5dry	13/05/2016	-46,2	15/05/2016	26,95
	5moist	10/06/2016	-10,6	10/06/2016	32,04
Event 6	6dry	21/08/2016	-88,5	22/08/2016	26,65
	6moist	29/09/2016	-11,5	29/09/2016	30,71
Event 7	7dry	01/10/2017	-448,3	18/10/2017	26,65
	7moist	30/10/2017	-15,1	30/10/2017	31,25

The minimum and maximum matric suction values observed in the seven events during the four years of monitoring pointed out well-fitted values when plotted on a correlation graph with a depth of 25 cm. According to this, it is important to emphasize that only Event 2 showed a poor correlation between the field data and the filter paper water retention curve due to a problem in the data acquisition system.

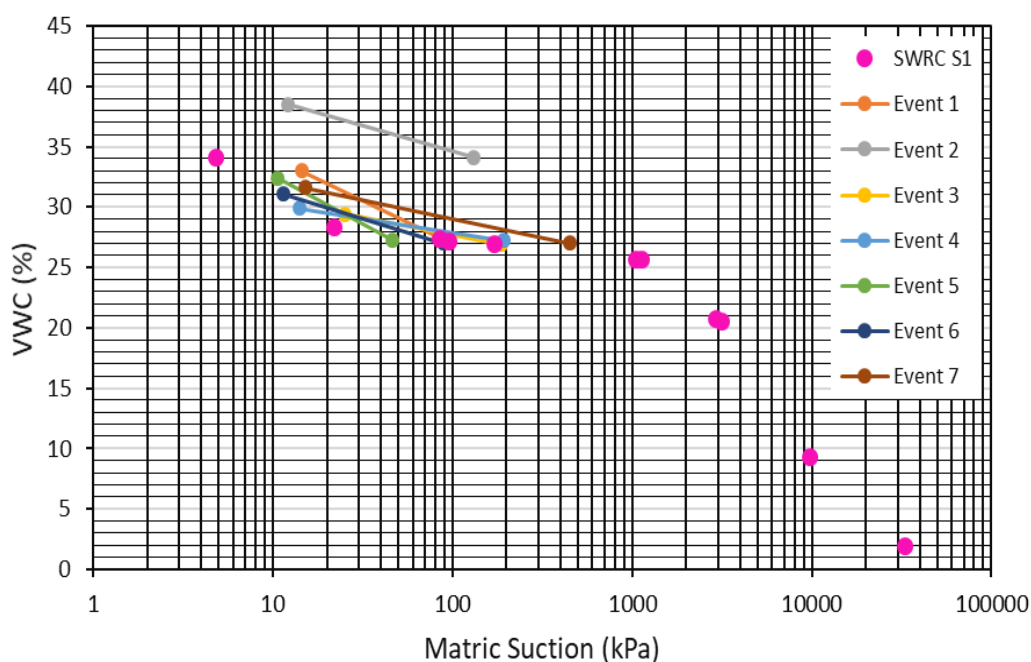


Figure 5.9 - Soil water retention curve and drying-wetting cycling points

Monitoring water potential during thunderstorm days

The final approach considered in this paper is regarding the crosschecking of thunderstorm days and its possible effects on the matric suction of the soil. To perform this analysis, the STARNET – lightning monitoring detection system – was operated with the support of the IAG - USP. The system uses a satellite monitoring apparatus and provides spatial lightning distribution (Figure 5.10).

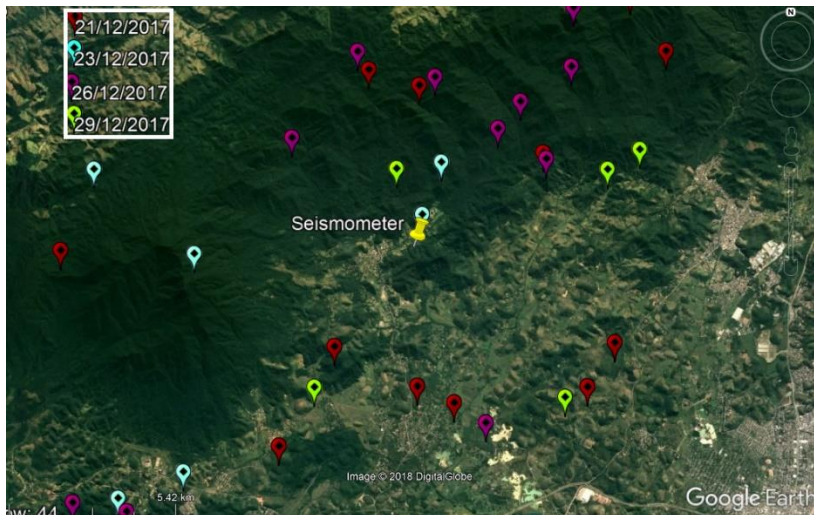


Figure 5.10 - Lightning distribution during 21, 23, 26 and 29 of December 2017

The results did not reveal any influence of lightning occurrence on the MPS-2 probes' values. The only changes were related to the rainfall occurrences, as depicted in Figure 5.11.

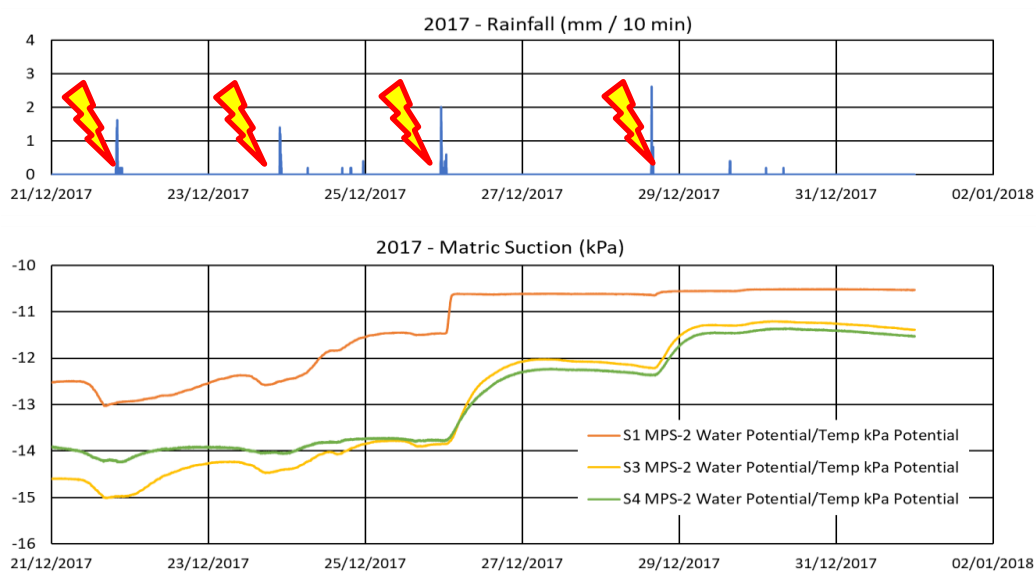


Figure 5.11 - Rainfall and Suction during thunderstorm period

5.5. Conclusions

It should be emphasised that the results from all the equipment installed for the field monitoring presented important characteristics of the wetting and drying periods that serve as great contributions for the understanding of the behaviour of soils, with regard to the variations of matric suction.

The scale problems were verified for the data acquisition rate, and because of this, it is important to note that high rates can preclude further analysis such as for flow and slope stability (since the calculation cannot refine the mesh for a long-term with the same frequency).

For a long-term field monitoring, it was possible to observe a low variation of matric potential during rainy periods (December, January, February and March), with approximately 10 kPa of the value remaining “constant” during the high saturation level. Overall, 7 events with maximum matric suction values were documented, in which the 0.25 m and 0.50 m depths were strongly influenced by atmospheric disturbances, emphasising the value of -448 kPa in Event 7.

The interlacing of meteorological data and matric potential and the rainfall data ruled lower levels of matric potential. However, relative humidity, solar radiation and air temperature were connected to the desaturation processes.

In light of correlations between soil and air temperature, it is important to emphasise that daily influences were mainly observed for the superficial probe at 0.25 m and 0.50 m depths. The 0.75 m and 1.0 m presented significant changes, but the day/night temperature fluctuations were not verified.

Finally, no influence of the lightning incidence on a rapid variation of the matric suction was detected. Even though the data acquisition interval was reduced to one minute, the graphs did not show any abrupt variation of the values.

6

Thunder: A micro seismic atmospheric source

Abstract

This Chapter aims to evaluate the thunder occurrences and its micro seismic characteristics, pointing out the influence of induced vibrations in the factor of safety reduction in a pseudostatic slope stability analysis. To perform it, the lightning' spatial distribution was monitored by the STARNET satellite network. In complement, the STS-2 triaxial seismometer was used to execute a field monitoring routine and obtain the thunder' induced vibrations for Horizontal Seismic coefficient (k_h) determination. Further, the SoilVision was used for slope stability analysis. The results of satellite and seismic monitoring depicted the vibrations induced by 39 lightning occurrences up to 10 km from the seismometer. Regarding accelerations, a maximum peak of particle of 0.02 m/s^2 was recorded. In the matter of power frequency spectrum, values around 80 Hz were revealed. The pseudostatic slope stability analysis showed that thunders Horizontal Seismic coefficient is away of the Yields coefficient values, required to reach the slope failure. Finally, the influence of vibrations caused by thunders is a subject for future researches because it is expected that, reducing the distance between the lightning occurrence and seismic monitoring, higher peak ground accelerations could be observed.

Impact factor: The current subject is considered a key-element that could contribute to explain the disaster occurred in January 2011, in Brazil.

Keywords: Thunder, micro-seismic source, thunder spatial distribution, pseudostatic analysis.

Introduction

In Brazil, both urban and countryside hilly areas have been affected by important rainfall induced soil slides and debris flows encompassing initially unsaturated soils (e.g. Ahrendt & Zuquette, 2003; Lima, 2013; da Silva & Spada, 2013; Nunes *et al*, 2013), leading to huge economical losses and large number of human losses. An example on that is given in Figure 1, which shows the distribution of the number of casualties in Brazil within the last 30 years due to such natural phenomena. It can be seen in Figure 6.1 that most of the casualties occurred in the Southeast region (SE), with Rio de Janeiro (RJ) being, by large, the most affected state of the country, with more than 50% of recorded casualties in the considered time period.

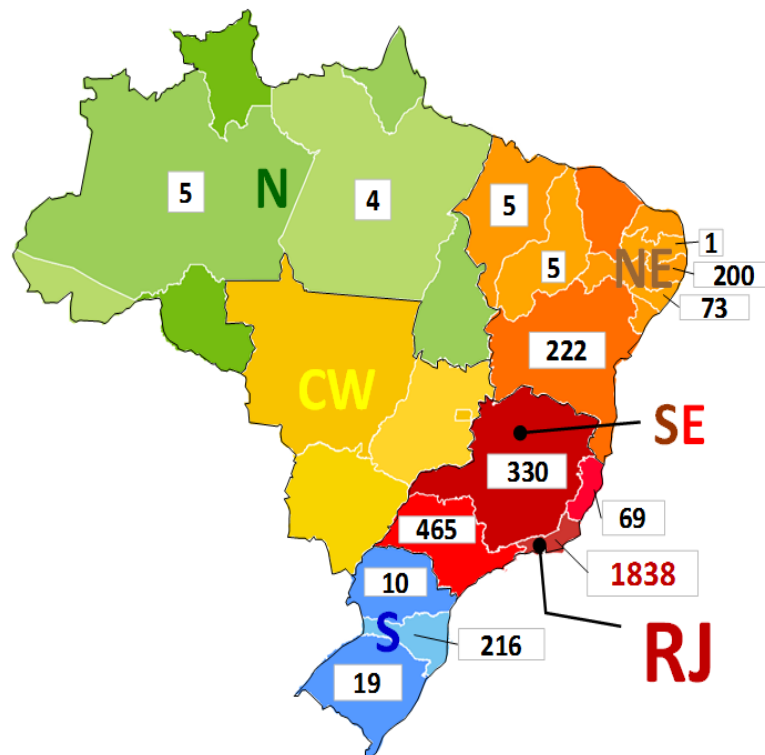


Figure 6.1 - Distribution of casualties in Brazil due to rainfall-induced landslides from January 1988 to May 2016 (data reproduced from IPT, 2016)

To have better conditions to predict and, ultimately, prevent or minimize risks associated to such types of geological hazards, the knowledge of the failure mechanisms developed under variable rainfall conditions is required and due to this, the failure of unsaturated natural soil slopes developed under variable rainfall conditions has been reported by a number of authors worldwide (e.g. Lumb,

1962; Brand,1984; Fredlund & Rahardjo, 1993; Fourie, 1996; Ng & Shi, 1998; Olivares & Picarelli, 2003; Collins & Znidarcic, 2004; Kitamura & Sako, 2010; Zhang *et al*, 2011; Kim *et al*, 2012; Wu *et al*, 2015; Zhang *et al*; 2016).

However, even with the strong background in mechanisms of failure, there are questions concerned to triggered factors responsible to start the soil displacement. Based on results of investigations of slope failures that have occurred in the city of Rio de Janeiro and taking into account the catastrophic event that occurred in the highland region of the state of Rio de Janeiro in 2011, problems comprised by thousands of landslides, such as observed in January of 2011 at municipalities of Nova Friburgo and Terezópolis, were not totally justified as a rainfall consequence (de Campos *et al*, 2018).

In this way, the current Chapter aims to monitoring thunder occurrences and reveal its micro seismic characteristics, pointing out the influence of induced vibrations in the factor of safety reduction of a pseudostatic slope stability analysis.

6.1. Review

Concerning lightning, there are two ways to generate ground motion / seismic response: by the lightning strike itself and by the acoustic coupling of thunders (Hinzen, 2012). Thunder is a lightning-dependent phenomenon, originated “*by a thermally driven expanding channel, producing shock waves that quickly degenerate into acoustic waves*” (Kappus & Vernon, 1991). Its sound’s characteristics are dependent of the heated channel geometry (Few *et al.*, 1967) by the conversion of shock wave into an acoustic wave (Few, 1969).

The transition from shock to acoustic wave is a complex subject and the current research doesn’t focus on this topic. However, it is important to emphasize that the atmospheric pressure decrease with the distance increase (Figure 6.2) of the heated channel and time (Rakov & Uman, 2003). In the zone of contact with the luminous channel, change in pressure due to shock waves can be as large as 800 kPa (Orville, 1968). At 35 cm from the heated channel, such change in atmospheric pressure is of the order of 200 kPa (Newman *et al.*, 1967). At a

distance of 1 km streaming of shock waves is negligible, being of the order of 0,1 kPa (Few, 1970).

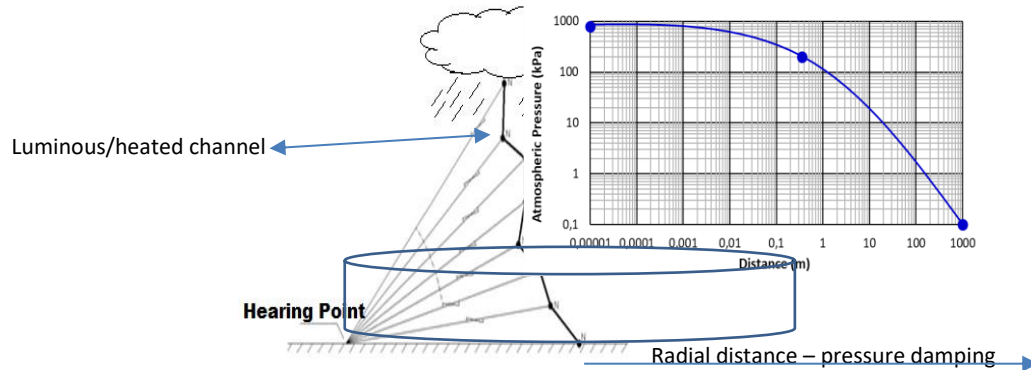


Figure 6.2 - Increase of atmospheric pressure caused by lightning incidence vs. distance

Regarding wave forms and air pressure variation, acoustic transducers/receivers were the first equipment used for field monitoring (Few, 1970). This method was replied by Holmes *et al.* (1971) that presented the power spectrum of 40 intracloud and cloud-to-ground lightning events that pointed out peak frequencies that ranged from less than 4 Hz to 125 Hz, with a main peak value of power at 50 Hz for cloud-to-ground occurrences.

In the light of the acoustic waves (thunders) sensitivity, Roy and Ribner (1984) emphasized it can reach 25 km from the sound emission point, depending on the characteristics of lightning and the geometry of the propagation site (Bass, 1980).

In the matter of seismic approach, Kappus & Vernon (1991) presented records and emphasized that the “*sound wave transfers sufficient energy to the ground to trigger seismometers set to record regional earthquakes*”. Lin & Langston (2007) revealed that “*lightning activity is a common natural meteorological phenomenon in many areas that produces a plentiful supply of acoustic shockwaves (thunder) that can be used as a seismic source*”. Voss *et al.* (2015), emphasized that seismic signals performed by lightnings are comprised by many subsequent peaks in thunderstorm events and “*the thunder signals differ from the earthquake signal and explosions by the absence of body waver and are characterized by an apparent surface velocity around the speed of sound*”.

6.2. Methods

- *Lightning incidence monitoring*

For the lightning incidence monitoring was used the STARNET (Sferics Timing And Ranging NETwork) lightning detection network, designed by the company Resolution Display Inc. (RDI) from NASA's development program, in which the Connecticut and National Observatory of Athens recently deployed a second-generation network (named Zeus).

The system operates on the VLF frequency (7-15 kHz) and detect radio noise emitted by electric discharges into the atmosphere. These noises are called spheres and can be activated during the frequency range when there is no waveguide delimited by the earth's surface and the ionosphere. In relation to the system of localization as electric shocks in its area of damping through the concept developed by Lee (1986b) called ATD (Arrival Time Difference), or difference of the time of arrival. Anagnostou & Chronis (2004) highlights the network as a current state of the art on continuous lightning monitoring from ground-based radio receivers combining satellite and lightning estimation over large regions.

In Brazil, the data access is managed by IAG-USP and can be required by (<http://www.starnet.iag.usp.br/index.php>). Concerning the method for lightning location, it was delimited a boundary of 15 km from the seismic apparatus installing point. The area was monitored from 01/12/2017 to 31/01/2018.

The thunder sections, based in the satellite monitoring (time accuracy - approximately 5 minutes), revealed 39 registers up to 10 km from the installed seismometer.

- *Seismic monitoring*

With the aim to analyze the induced vibrations from lightning, it was performed a field monitoring into the PUC-Rio, at Tinguá experimental campus (Figure 6.3), under coordinates 663961E and 7500946N.



Figure 6.3 - Tinguá experimental campus

The experimental apparatus, provided by a cooperation with the National Observatory (ON), is comprised by the seismometer STS-2, manufactured by Kynometrics (Figure 6.4 - a) and a Quanterra data acquisition system, comprised by the Baler PB44 and Q-330 (Figure 6.4 - b and c).



a)



b)



c)

Figure 6.4 - Experimental apparatus. a) STS-2 Seismometer. b) Baler PB44. c) Q-330

Regarding the STS-2, the sensor is a portable very-broad-band triaxial seismometer. The equipment is designed for quick and simple installation, wide temperature range of operation, and secure transport.

The setup has a cylindrical package with approximately 235 mm of diameter and 260 mm of high. The STS-2 is vacuum-tight and its construction is further designed to minimize the distortion of the package by barometric pressure changes by isolating the top and bottom covers from the massive base plate, in a similar way to the isolation of a seismograph pier from its surrounding building. In addition, the top and bottom covers are secured to the base plate with compliant O-ring allowing the covers to compress without stressing the entire package. Further, the sealed construction and massive metal base plate provide thermal isolation and inertia.

The STS-2 uses identical 3 obliquely-oriented mechanical sensors (Figure 6.5) to provide an output signal proportional to ground velocity over a broad range. In addition, the tri-axial design guarantees that horizontal and vertical components are matched as closely as possible.

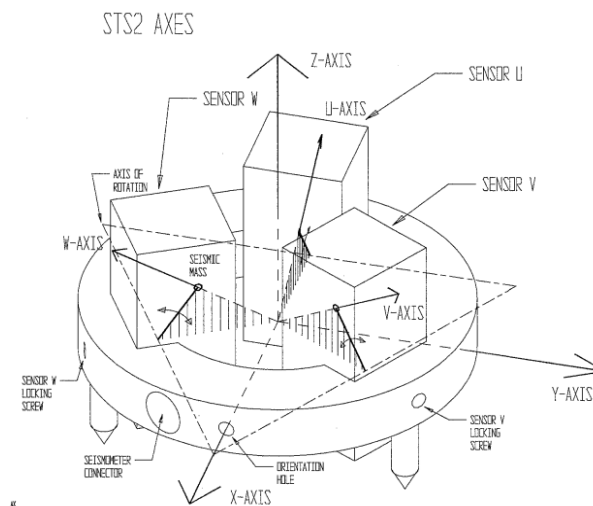


Figure 6.5 - STS-2 internal arrangement. The 3 obliquely-oriented sensors (Quanterra, 1996)

Since all 3 sensors are mutually aligned by mounting to a common frame and the complete package is factory-calibrated using a standardized 3-dimensional shake table, the STS-2 eliminates some common causes of installation and calibration error.

In the matter of data acquisition, were used two sets of dataloggers. The first, comprised by PB44 and Q330 and the second, comprised by Q330S+.

The Quanterra Packet Baler PB44 is a modular, field-ready high-capacity recording system for the Quanterra Q330 ultra low-power high-resolution seismic data acquisition equipment (Quanterra, 2018). The system uses telemetry for ready-to-use data in internationally-standardized Federation of Digital Seismic Networks miniseed format. The Quanterra Q330 is an advanced IP network-aware very low-power 3-6 channel remote broadband seismic digitizer. It is comprised by an ultra-low-power delta-sigma 24-bit ADC, a DSP/RAM module, a GPS receiver, power conversion, sensor control, and a telemetry management module.

- *Installing procedures and data manipulation*

For installing procedure, the equipment was handled and moved when the three locking screws were in the locked position. It protects the seismic mass and the sensitive internal electronic arrangements. Further, the data acquisition system and the sensor are sensitive to temperature variations, also requires protections.

Concerning this, a metallic chamber was used to isolate the data acquisition and a concrete ring protection with 1-meter of diameter and 60 cm height was used to protect the sensor (Figure 6.6).

The concrete ring was sealed (Figure 6.7) with an expanding polyurethane foam. It is important to emphasize that a maintenance/verification window was left to be opened whenever required.

To achieve the current goals, the data acquisition systems was set to provide data in the SEED (Standard for the Exchange of Earthquake Data) format. In the matter of ground vibration signals, detected by the seismic sensors, it requires computer processing to output mini seed files and then in the txt extension.

The ground vibration signals were recorded simultaneously in both directions (n-s, e-w and z). In addition, the signals were converted from time domain to frequency domain using FFT by Origin software manipulation.

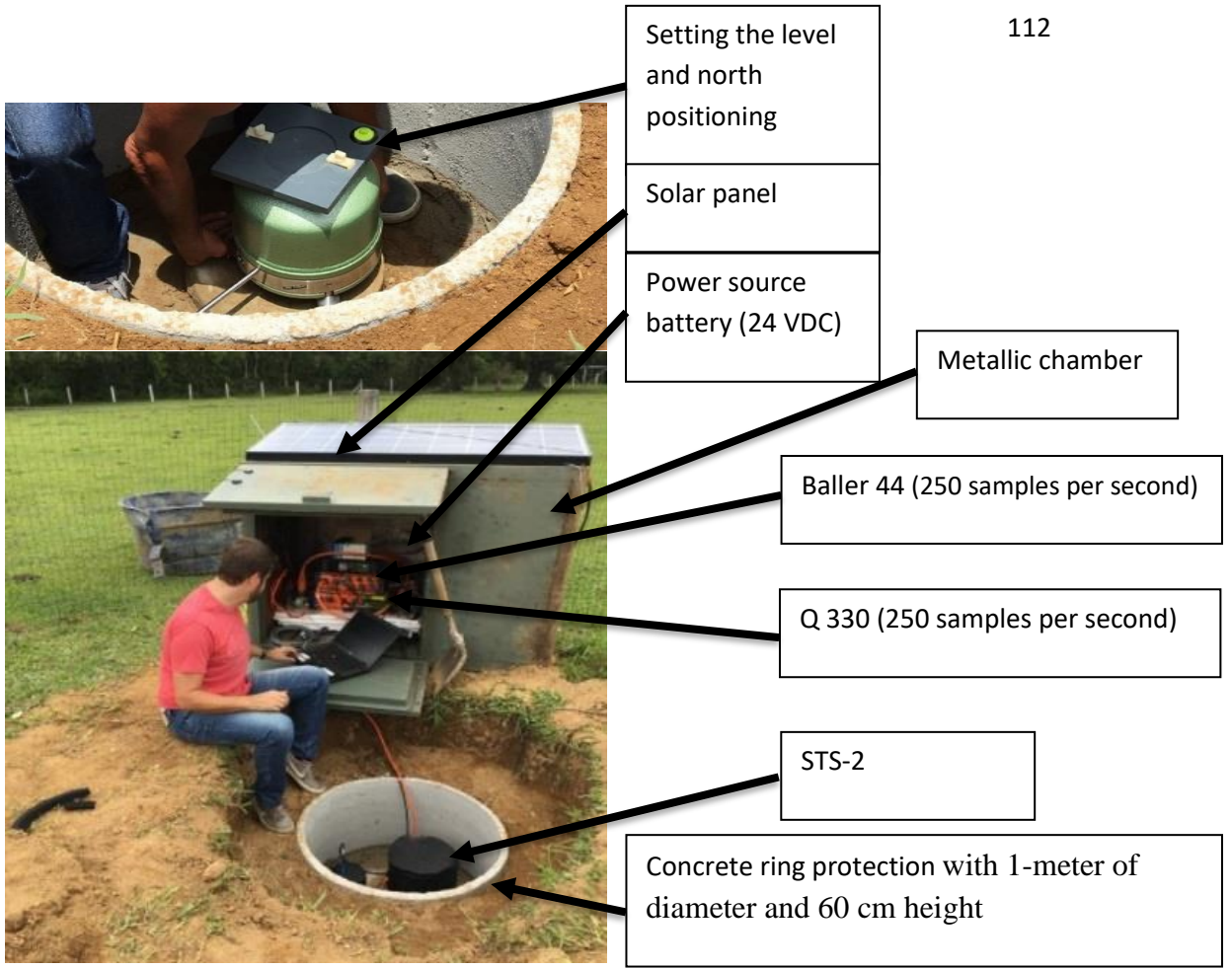


Figure 6.6 - Seismographic equipment setup

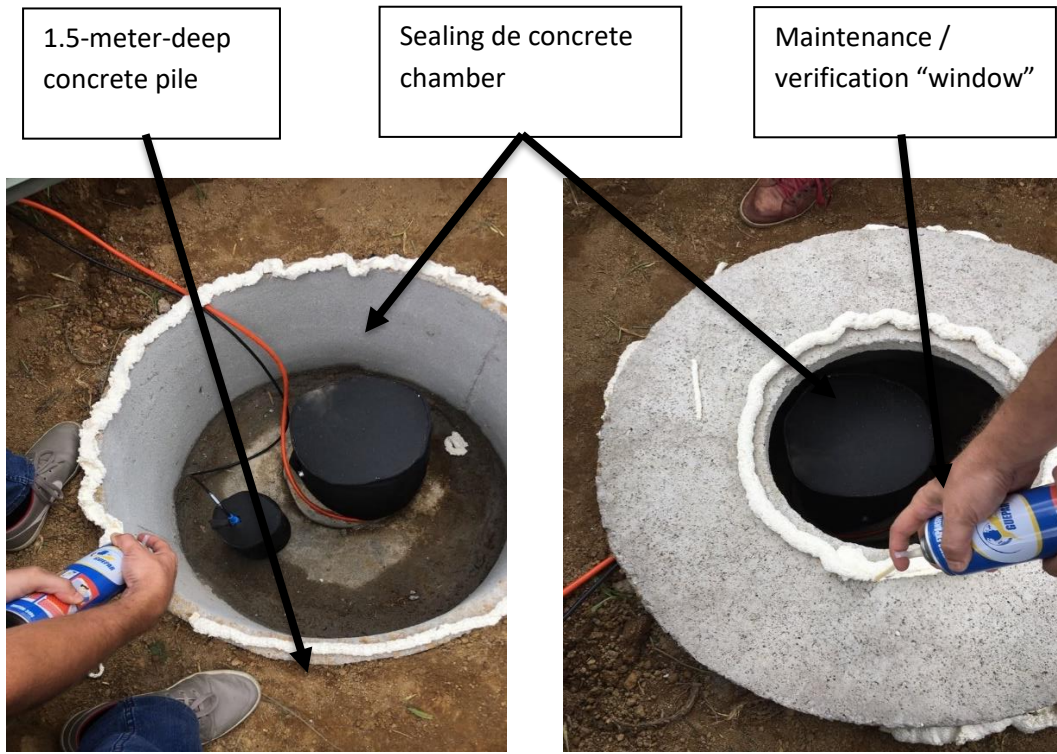


Figure 6.7 - Installing procedure and field disposal

- *Slope stability: A static and pseudostatic approach in limit equilibrium analysis.*

For the current research was used the SoilVision software to perform a slope stability analyse based on the GLE - *General Limit Equilibrium Method* (Fredlund and Kran, 1977; Fredlund *et al.* 1981). The procedure evolved from a static to a pseudostatic method by the introduction of Seismic coefficient k_h .

The GLE method considers two factors of safety equations to determine force and/or moment equilibrium of a mass of soil above a potential failure surface. The principle assumptions of these analyses are: The soil above the potential failure plane is rigid thus shearing can only occur on the potential failure surface; the material is perfectly plastic which means that there is no shear deformation until soil resistance is reached; and the shear strength is mobilized at the same rate along the failure surface (i.e., the factor of safety is constant along the entire failure surface).

The pseudostatic method is the most common solution in the matter of seismic issues in slope stability procedures. It consists of adding horizontal and vertical static forces in the Equilibrium Limit Analysis (Figure 6.8). These two forces are chosen to be equivalent to the effects of dynamic components generated during the soil mass shaking, being proportional to the weight W of failing soil mass. These static forces are named Seismic Coefficients and are related to the proportionality for the horizontal and vertical directions (respectively k_h and k_v).

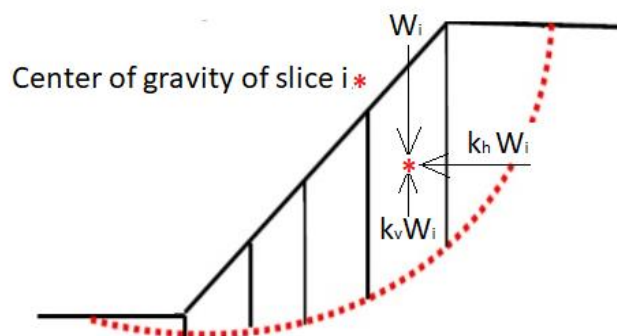


Figure 6.8 - Seismic forces k_h and k_v

Even with the theory considering both forces, it is common to assume k_v to be zero (Briaud, 2013). Further, considering only horizontal forces, the peak acceleration generated during a vibration source occurs for a very short period,

and seismic coefficients correspond to acceleration values well below the peak ground accelerations (Kramer, 1996). Furthermore, Abramson *et al.* (2002), revealed standard values of horizontal seismic coefficient (Table 6.1)

Table 6.1 - Horizontal seismic coefficient. Adapted from Abramson *et al.* (2002)

Seismic Coefficient K_h (g)	Comment
0.10	Major earthquake, U.S. Army Corps of Engineers, 1982
0.15	Great earthquake, U.S. Army Corps of Engineers, 1982
0.05 to 0.15	State of California
0.15 to 0.25	Japan
1/3 to 1/2 of peak ground acceleration (PGA)	Marcuson and Franflin, 1983

An assumption of finding the horizontal coefficient k_h responsible to cause a failure of a slope is related to the critical value of k_h and is named as *yield horizontal seismic coefficient* (k_y). The general terms, the value of k_y can be related to the peak ground acceleration (PGA) of a vibration in a slope (Table 6.2) and corresponds to a required acceleration to reach the value 1 in the factor of safety of a slope (Figure 6.9).

Table 6.2 - Relative Position of K_y and PGA (adapted from Abramson *et al.* 2002)

Relative Position of K_y and PGA	Observation
$k_y > \text{PGA}$	No failure likely
$0.5 \text{ PGA} < K_y < \text{PGA}$	Minor damage possible
$k_y < 0.5 \text{ PGA}$	Failure likely

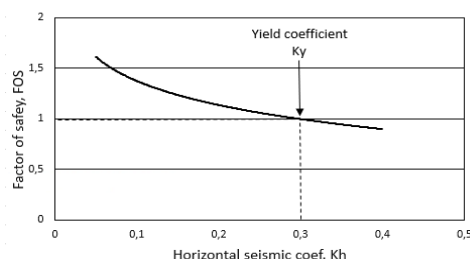


Figure 6.9 - Yield coefficient (k_y)

Concerning the boundary conditions to perform the slope stability analysis, the dynamic/pseudostatic condition is a short-term stability problem and because of this, the undrained approach is commonly required. In this way, for the current research, the analysis was carried out in undrained conditions for 4 slope

geometries (Table 6.3) comprised by a soil with: Specific weight = 18.8 kN/m³; – Undrained Shear Strength S_u – 25 kPa (Karray *et al.*, 2018); Ratio ($k = \tau/\sigma_v'$) – 0.5. In addition, concerning the pseudostatic approach, was used the horizontal Seismic coefficient (k_h) acquired in the seismic field monitoring. Further, synthetic horizontal seismic coefficient was increased to verify the k_y . crosschecking k_h and factor of safety calculated.

Table 6.3 - Slope geometries

Slope	Slopes geometries			
	2:1	1.5:1	1:1	0.5:1
Width (m)	20	15	10	5
Height (m)	10	10	10	10
Alfa (m)	26,56	33,69	45	63,43

6.3. Results

The STARNET lightning detection system revealed 39 occurrences between December 24th and January 22th (Table 6.4).

Table 6.4 - Lightning spatial distribution

Lightning	Longitude	Latitude	Year	Month	Day	hh	Min	sec
L1	-43,362862	-22,61216	2017	12	24	20	38	47
L2	-43,37281	-22,601601	2017	12	24	20	0	8
L3	-43,44025	-22,59819	2017	12	24	19	58	10
L4	-43,41061	-22,56926	2017	12	29	17	12	2
L5	-43,406921	-22,592369	2018	1	2	19	45	3
L6	-43,379169	-22,59128	2018	1	2	20	17	57
L7	-43,384689	-22,618071	2018	1	2	20	28	54
L8	-43,376831	-22,570511	2018	1	3	18	42	38
L9	-43,376831	-22,570511	2018	1	3	18	42	38
L10	-43,421089	-22,583719	2018	1	3	18	2	7
L11	-43,37463	-22,58469	2018	1	3	18	41	6
L12	-43,387508	-22,5921	2018	1	3	18	24	48
L13	-43,43969	-22,60754	2018	1	3	18	30	41
L14	-43,43969	-22,60754	2018	1	3	18	30	41
L15	-43,416561	-22,620609	2018	1	3	18	35	13
L16	-43,433529	-22,61182	2018	1	10	21	15	34
L17	-43,36702	-22,609461	2018	1	10	21	17	25
L18	-43,433769	-22,57472	2018	1	13	23	25	29
L19	-43,371429	-22,60265	2018	1	15	19	1	2
L20	-43,431839	-22,571939	2018	1	20	18	49	58
L21	-43,394451	-22,576891	2018	1	22	19	25	35
L22	-43,39872	-22,578711	2018	1	22	19	25	35
L23	-43,396069	-22,587709	2018	1	22	18	54	57
L24	-43,37077	-22,59305	2018	1	22	19	14	7
L25	-43,411751	-22,60585	2018	1	22	17	36	40
L26	-43,380169	-22,59944	2018	1	22	19	25	36
L27	-43,430809	-22,55969	2018	1	23	21	54	26
L28	-43,42643	-22,591009	2018	1	23	22	5	52
L29	-43,386688	-22,59079	2018	1	25	16	59	36
L30	-43,396259	-22,596581	2018	1	25	16	51	55
L31	-43,426239	-22,568029	2018	1	26	16	50	54
L32	-43,431141	-22,56683	2018	1	26	15	13	54
L33	-43,431591	-22,5665	2018	1	26	15	13	54
L34	-43,411789	-22,58996	2018	1	26	17	10	25
L35	-43,389339	-22,58893	2018	1	26	16	58	8
L36	-43,373619	-22,56992	2018	1	29	20	34	27
L37	-43,383881	-22,582781	2018	1	29	20	37	42

L38	-43,36438	-22,60626	2018	1	29	20	39	0
L39	-43,38232	-22,599489	2018	1	29	20	39	0

Figure 6.10 shows the lightning incidence spatial distribution and the Table 6.5 depicts the distances of L34, L10, L23, L5, L22 and L21 from the sampling point (seismic monitoring).



Figure 6.10 - Lightning distribution

Table 6.5 - Distances of lightning occurrences in comparison with sampling point (seismic monitoring)

Lightning	Distance (m)
L34	500
L10	1,575
L23	1,150
L5	868
L22	1,460
L21	1,900

The field monitoring results emphasizes that thunders can be considered as a natural seismic source because it presented energy to trigger the seismograph and cause wave-forms.

In the light of events analysis, was chosen 6 lightning occurrences (L5, L22, L21, L34, L10 and L23) for accelerations and frequency spectrum analysis. The results (Figure 6.11 to 6.16) shows the 3-axis overlaid signals with a maximum acceleration of 0,02 m/s² and 30 seconds of maximum time. Further, in the matter of frequency spectrum, were revealed values from 24 Hz to 84 Hz.

The results presented the classical signal for a clap, comprised by a single-branch lightning for the occurrence of L34, L10 and L23 (Figure 6.11 to 6.13), and depicted signals associated to rumble, comprised by a multiple-branch lightning for the occurrence of L5, L22 and L21 (Figure 6.14 to 6.16). The

seismograms revealed a higher peak ground acceleration in the vertical components (z-axis).

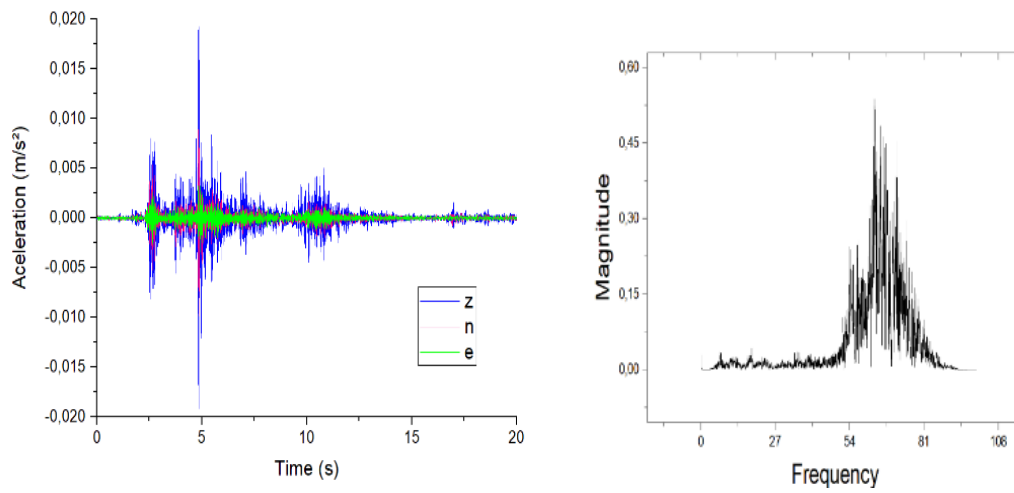


Figure 6.11 - Lightning L5. Acceleration vs Time (a); dB vs Frequency (b)

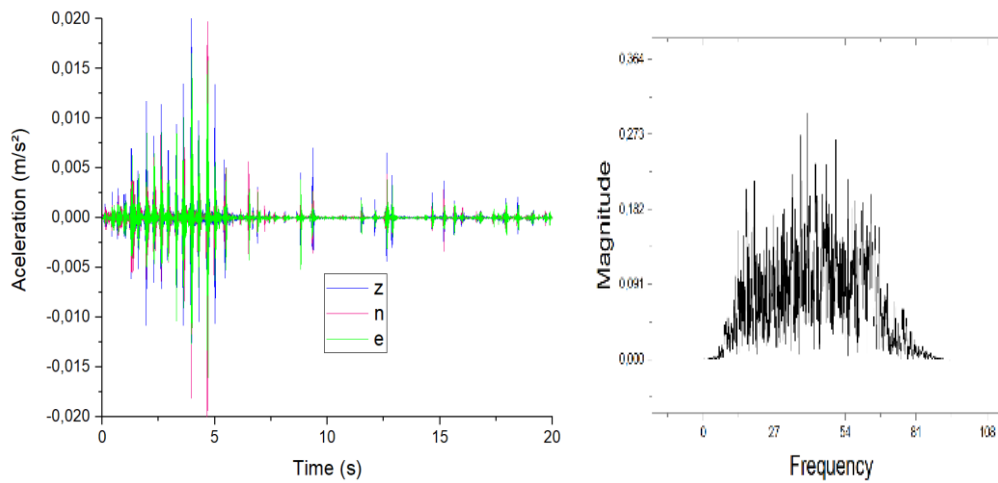


Figure 6.12 - Lightning L22. Acceleration vs Time (a); dB vs Frequency (b)

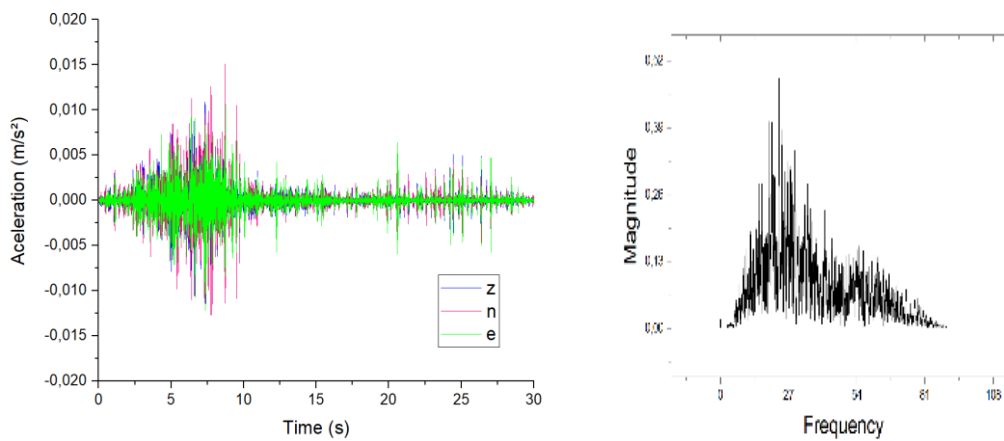


Figure 6.13 - Lightning L21. Acceleration vs Time (a); dB vs Frequency (b)

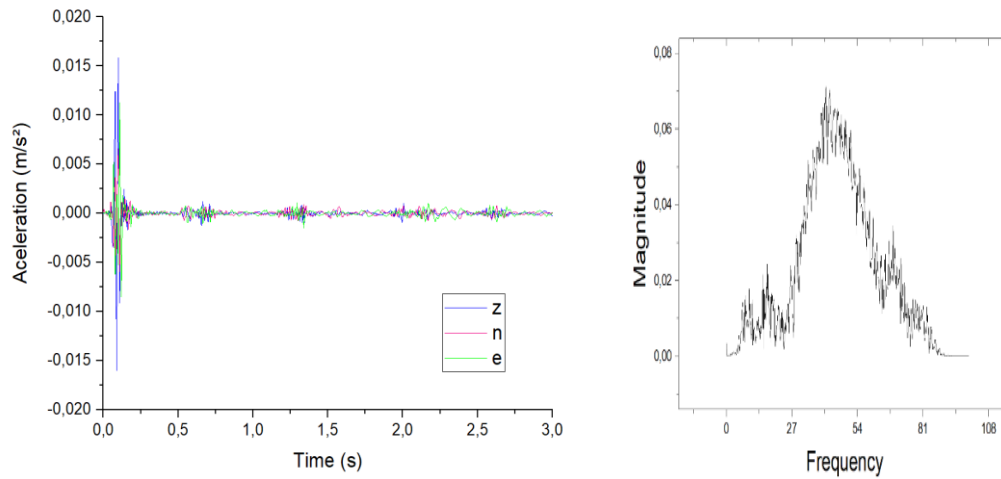


Figure 6.14 - Lightning L34. Acceleration vs Time (a); dB vs Frequency (b)

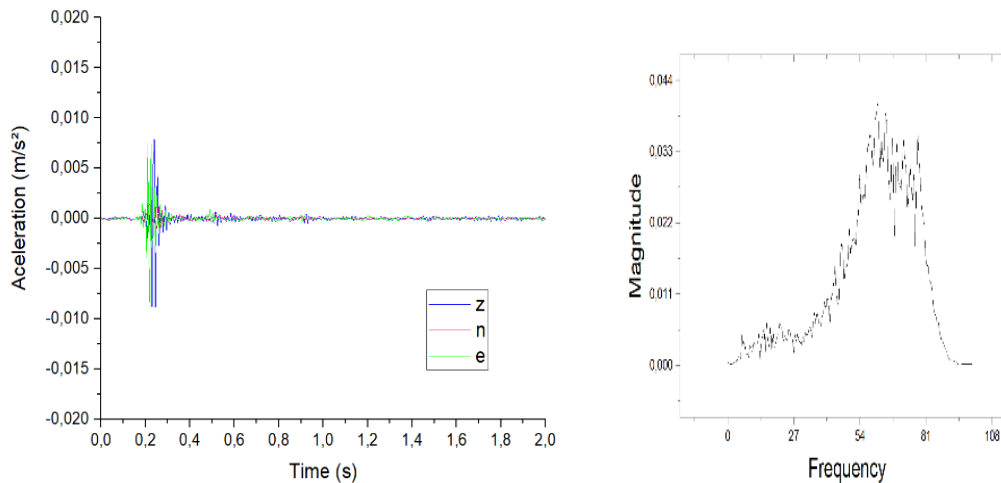


Figure 6.15 - Lightning L10. Acceleration vs Time (a); dB vs Frequency (b)

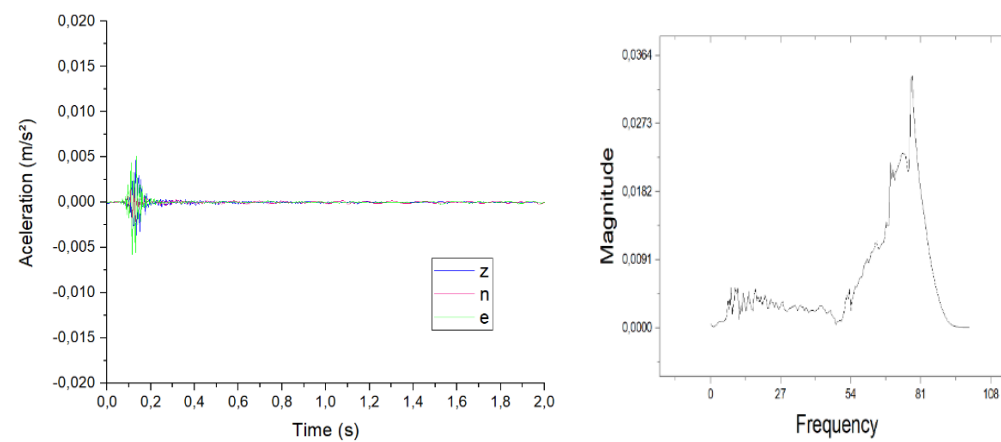


Figure 6.16 - Lightning L23. Acceleration vs Time (a); dB vs Frequency (b)

In the matter of k_h determinations and its use in SoilVision pseudostatic method, the thunder-based peak ground acceleration (PGA) must be changed from m/s^2 to g . Further, the vibrations to determine the horizontal seismic coefficient k_h were based in 1 and $\frac{1}{2}$ PGA revealed a k_h of 0.002 g and 0.001 g respectively.

The Table 6.6 presents the FOS obtained for the slope geometries submitted to the Horizontal Seismic Coefficients. The results highlighted that thunders' k_h do not cause a significant influence in comparison with the slope stabilities executed without a thunder micro-seismic loading.

Table 6.6 - k_h and the equivalent FOS

Horizontal Seismic Coefficient k_h (g)	FOS (Slope w:h)				
	2:1	1.5:1	1:1	0.5:1	
0,000	2,149	1,898	1,663	1,568	
0,001	2,121	1,894	1,658	1,565	Lightning 1/2 Peak Ground Acceleration
0,002	2,115	1,891	1,655	1,563	Lightning Peak Ground Acceleration
0,010	2,079	1,865	1,625	1,56	
0,020	2,063	1,84	1,6	1,536	
0,050	1,915	1,754	1,537	1,477	
0,100	1,74	1,623	1,459	1,352	
0,150	1,59	1,513	1,455	1,422	
0,200	1,464	1,402	1,396	1,298	
1,000	0,566	0,58	0,597	0,6	

The coefficient k_y was revealed for the slope geometries (Figure 6.17). The results showed that small slope gradients require higher Yields coefficients when factor of safety reaches 1. Further, k_y is much higher than thunder PGA or $\frac{1}{2}$ PGA (k_h) and because of this, no failure is likely.

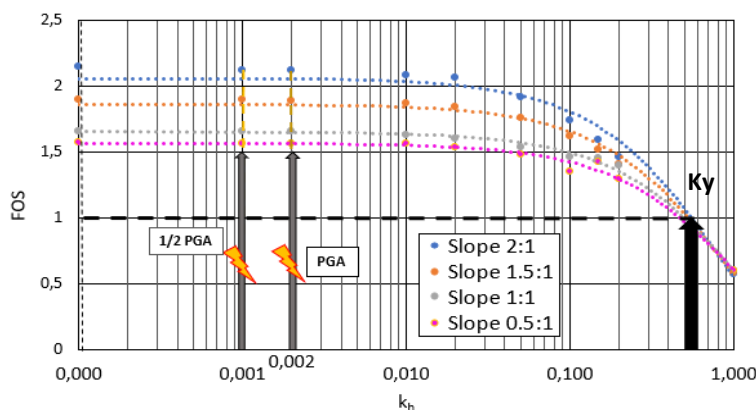


Figure 6.17 - Comparison of horizontal seismic coefficient obtained during thunder monitoring (PGA and $\frac{1}{2}$ of PGA) and Yield coefficient

6.4.

Conclusions – Final considerations

The lightning monitoring is a time-consuming procedure because the lightning season just occurs between December and February in Rio de Janeiro. Further, considering the unprecedented approach (related to monitoring an intermittent atmospheric phenomenon), the 250 samples per second was chosen as the sampling rate.

Regarding the crosschecking of satellite and seismometer data, it is proved that thunders can be considered as an atmospheric micro-seismic source.

Concerning power signal-distance correlations, it was not possible to identify remarkable characteristics as dumping or time-dependence. It emphasizes thunders as a lightning dependent phenomenon (related to the heated channel geometry).

By the seismic data analysis, it is possible to identify the rumble and clap characteristics, depicted by the peak acceleration and time correlations. In this way the figures 6.11, 6.12 and 6.13 are related to rumble and figures 6.14, 6.15 and 6.16 are related to clap sounds. The signals and frequency spectra can be well correlated with literature microphone or geophone previous results, even without the filters introduction or any other data treatment.

Regarding the pseudostatic analysis, it was verified no practical influence in the factor of safety due to thunder occurrence. However, we must emphasize that closer lightnings can produce higher vibrations and increase the seismic coefficient values.

Finally, by the current research analysis, it is possible to emphasize that thunders can be inputted in pseudostatic stability procedures, revealing a new approach for landslides triggering factors responsible to start a failure of a slope.

7

Final considerations

- Lightning and thunders are interdependent phenomena. In this way, the sound characteristics cannot be dissociated from the heated channel geometry.
- The lightning-soil direct incidence can reveal structural damages especially in saturated soils. It also suggests a possible correlation between the electrical conductivity and permittivity of the soil, ruled by the soil material constitution and its structural arrangement.
- The use of 3D-microtomography was extremely important because it depicted the structural characterization, revealing the material internal arrangement for samples collected up to 1 m deep.
- To produce reliable field monitoring data, the calibration of probes revealed the dependence of Bulk density for EC-5 readings. In addition, was confirmed that different values are measured for different installing procedures.
- The soil-atmosphere interaction revealed few dried periods, usually associated to the lower relative humidity value. However, was not possible to observe rapid changes of soil matric potential during thunderstorms (lightning occurrences).
- Thunders can trigger seismic equipment set to regional seismic records;
- Thunder field monitoring revealed induced accelerations up to 0.02 m/s^2 .
- Was not possible to correlate the spatial lightning/thunder distribution and the induced acceleration;
- Regarding the pseudostatic analysis, it was verified no practical influence in the factor of safety due to thunder occurrence. However, we must emphasize that closer lightnings can produce higher vibrations and increase the seismic coefficient values.
- Finally, by the current research analysis, it is possible to emphasize that thunders can be inputted in pseudostatic procedures, revealing a new approach for landslides triggering factors responsible to start a failure of a slope.

References

ABNT - Associação Brasileira de Normas Técnicas. **ABNT NBR 5418: Instalações elétricas em atmosferas explosivas**. Rio de Janeiro, Brazil. 2005.

ABNT - ASSOCIAÇÃO BRASILEIRA DE NORMAS TÉCNICAS. **NBR-6508: Solo – Determinação da massa específica dos grãos**. Rio de Janeiro. 1984.

ABNT - ASSOCIAÇÃO BRASILEIRA DE NORMAS TÉCNICAS. **NBR-7181: Amostras de Solo – Granulometria conjunta**. Rio de Janeiro. 1984.

ABNT - ASSOCIAÇÃO BRASILEIRA DE NORMAS TÉCNICAS. **NBR-6459: Solo – Determinação do Limite de Liquidez**. Rio de Janeiro. 1984.b.

ABNT - ASSOCIAÇÃO BRASILEIRA DE NORMAS TÉCNICAS. **NBR-7180: Solo – Determinação do Limite de Plasticidade**. Rio de Janeiro. 1984.c.

ABNT - ASSOCIAÇÃO BRASILEIRA DE NORMAS TÉCNICAS. **NBR-6457: Amostras de Solo – Preparação para ensaios de compactação e ensaios de caracterização**. Rio de Janeiro. 1986.

ABRAMSON, L. W. et al. **Slope Stability and Stabilization Methods**. New York, John Wiley & Sons. 2002.

AHRENDT, A.; ZUQUETTE, L. V. **Triggering factors of landslides in Campos do Jordão city, Brazil**. Bull. Eng. Geol. Env. 62:231–244, DOI 10.1007/s10064-003-0191-8. 2013.

ALVES, H. D. L. **Metodologia de microtomografia computadorizada com dupla energia para caracterização mineralógica de rochas**. Tese de Doutorado, UFRJ/COPPE. 2015.

ANTUNES, F. dos S.; WERNICKE, J.; VETTORI, L. **Contribuição ao estudo da relação molecular sílica alumina (Ki) dos solos**. Rio de Janeiro: IME. 15 p. (IME. Publicacao técnica, 42). 1975.

ASTM. **Standard Test Method for Measurement of Soil Suction in ASTM 5298-9a**. 1997.

ASTM. **Standard Test Method for Moisture Retention Curves of Porous Building Materials using Pressure Plates in ASTM C1669.** 2015.

ASTM. **American Society for Testing Materials. ASTM-D 5298-03. Standard test method for measurement of soil potential (suction) using filter paper.** 2003.

ANDREAS, J.; KOESTEL, J. **Three-Dimensional Printing of Macropore Networks of an Undisturbed Soil Sample.** *Vadose Zone Journal*. 14. 1-10. 10.2136/vzj2014.08.0111. 2015.

BALACHANDRAN, N. K. **Infrasonic Signals from Thunder.** *Journal of Geophysical Research*. Vol.84, NO. C4. 1979.

BASS, H. E. **The propagation of thunder through the atmosphere.** *J. Acoust. Soc. Am.*, 67:1959-1966. 1980.

BAYER, A.; VOGEL, H-J.; ROTH, K. **Direct measurement of the soil water retention curve using X-ray absorption.** *Hydrol. Earth Syst. Sci.*, 8, 2–7, doi:10.5194/hess-8-2-2004, 2004.

BECKERS, E. et al. **X-ray microtomography: A porosity-based thresholding method to improve soil pore network characterization.** *Geoderma*, 219–220, 145–154. 2014.

BERTOLINO, A. V. F. A. **Influência do Manejo na Hidrologia de Solos Agrícolas em Ambiente Serrano: Paty do Alferes – RJ.** Tese de Doutorado, UFRJ, Rio de Janeiro. 2004.

BHARTENDU, H. **Acoustics of thunder.** Ph.D. dissertation, Univ. of Saskatchewan, Saskatoon, Canada. 1964.

BICALHO, K. V.; CUI, Y. J. **Simulations of in situ water content and temperature changes due to ground-atmospheric interactions.** *Proceedings of the 17th International Conference on Soil Mechanics and Geotechnical Engineering: The academia and practice of geotechnical engineering*, Alexandria, Egypt, Publisher IOS Press, 534-537. 2009.

BICALHO, K. V.; VIVACQUA, G. P. D.; CUI, Y. J. **Influences of the soil-atmosphere interface interactions on the soil water content and temperature profiles.** *Unsaturated soils*, Alonso & Gens (eds), 2, 1103-1108. 2011.

BLIGHT, G. E. **Interactions between the atmosphere and the earth.** *Geotechnique*, vol.47 (4): pp. 715-767. 1997.

BLIGHT, G. E. **Unsaturated Soil Mechanics in Geotechnical Practice**. CRC Press. ISBN: 978-0-415-62118-2, eBook ISBN: 978-1-315-88293-2. 2013.

BORDONI, M. et al. **Rainfall-Induced Landslides: Slope Stability Analysis Through Field Monitoring**. doi:10.1007/978-3-319-04996-0_42. 2014.

BORE, T. et al. **3D-FEM modeling of F/TDR sensors for clay-rock water content measurement in combination with broadband dielectric spectroscopy**. in Sensors Applications Symposium (SAS), doi:10.1109/SAS.2015.7133601; 2015.

BORGES, J.; PIRES, L.; PEREIRA, A. **Computed tomography to estimate the representative elementary area for soil porosity measurements**. Sci World J. doi:10.1100/2012/526380. 2012.

BORKOWSKI A. K. **Análise de curvas de retenção e de distribuição de poros de um latossolo vermelho distrófico submetido aos sistemas de plantio convencional e direto**. Dissertação (Mestrado em Engenharia Civil) - Universidade Estadual de Ponta Grossa, Ponta Grossa. 2009.

BOSZCZOWSKI, R. B; CAMPOS, T. M. P. de. **Avaliação de propriedades mecânicas e hidráulicas de um perfil de alteração de granito-gnaise de Curitiba, PR**. Tese (Doutorado em Engenharia Civil) - Pontifícia Universidade Católica do Rio de Janeiro, Rio de Janeiro. 2008.

BOUMA. J. et al. **The Function of different types of macropores during saturated flow through four swelling soil horizons**. Soil Sci Soc Am J. 41:945-50. 1977.

BOURSCHEIDT, V. **Study of the relation among lightning, relief, surface temperature and soil types in the Rio Grande do Sul**. INPE-15238-TDI/1325, 126p (in Portuguese). 2008

BRAND, E. W. **Landslides in south Asia: A state-of art report**. Proc. 4th International Symposium on Landslides, Toronto, Canada, pp. 17-59. 1984.

BRAND, E. W. **Slope instability in tropical areas**. Proc. 6th Int, Symp. on Landslides, D. H. Bell, ed., Balkema, Rotterdam, The Netherlands, pp. 2031-2051. 1992.

BRANDT, E. W. **Geotechnical engineering in tropical residual soils**. 1st International Conference on Geomechanics in Tropical Lateritic and Saprolitic Soils, Brasília, Brazil, V.3, 23-100. 1985.

BRIAUD, J-L. **Geotechnical Engineering: Unsaturated and Saturated Soils**. New York, John Wiley & Sons. 2013.

HOLMES, C. R.; BROOK, M.; KREHBIEL, P.; MCCRORY, R. **Reply to Comment by Bhartendu on “On the Power Spectrum and Mechanisms of Thunder.”** J. Geophys. Res., 76 p. 7443. 1971.

CARNAVALE, T. S.; DE CAMPOS, T. M. P. & OLIVEIRA, A. R. M. B. **Response of tensiometers to laboratory thunder sound replicated waves**. Unsaturated Soils: Research and Applications, CRC Press Taylor & Francis Group. Proc. 6th International Conference on Unsaturated Soils, Sidney, Australia, V. 2. pp. 1721-1726. 2014.

CARNAVALE, T. S. et al. **Mechanical behaviour of a reconstituted granite-gneissic soil submitted to a replicated lightning**. In: From Fundamentals to Applications in Geotechnics, IOS Press. XV Pan-American Conference on Soil Mechanics and Geotechnical Engineering, Buenos Aires, V. 1. pp. 2236-2242. 2015.

CARNAVALE, T. S. et al. **Unconfined strength of an unsaturated residual soil struck by replicated lightning**. 3rd European Conference on Unsaturated Soils, E-UNSAT <http://dx.doi.org/10.1051/e3sconf/20160914006>. 2016.

CARVALHO, T. M. O. **Desenvolvimento de um sistema de medição de variação de volume total de amostras não saturadas em ensaios triaxiais e avaliação da influência da técnica de saturação no comportamento tensão-deformação-resistência de solos residuais**. Tese de Doutorado, PUC-Rio, Rio de Janeiro. 2012.

CHILAR, J., ULABY, F. T. **Dielectric Properties of Soils as Function of Moisture Content**. Kansas Univ. Center for Research. N75-26555. 1974.

CHOI, E-Y.; YOON, Y-H.; CHOI, K-Y.; LEE, Y-B. **Environmentally sustainable production of tomato in a coir substrate hydroponic system using a frequency domain reflectometry sensor** Journal Article Horticulture, Environment, and Biotechnology - Korean Society for Horticultural Science; URL: <http://dx.doi.org/10.1007/s13580-015-0036-y> 167-177. 2015.

COELHO NETTO, A. L. et al. **January 2011: the extreme landslide disaster in Brazil**. 2nd World Landslide Forum, Rome, Italy, 6p. 2011.

COLLINS, B. D. & ZNIDARCIC, D. **Stability analyses of rainfall induced landslides**. Journal of Geotechnical and Geoenvironmental Eng. 130(4):362-372. DOI: 10.1061/(ASCE)1090-0241(2004)130:4(362). 2004.

CRESTANA, S. **Técnicas recentes de determinação de características do solo.** In: Reunião Brasileira de Manejo e Conservação do Solo e da Água, 10., Florianópolis, 1994. Resumos. Florianópolis, Sociedade Brasileira de Ciência do Solo. p.86-97. 1994.

CRESTANA, S. et al. **Calibração e uso de um tomógrafo computadorizado em ciência do solo.** R. Bras. Ci. Solo, 16:161-167. 1992.

CRESTANA, S.; MASCARENHAS, S.; POZZI-MUCELLI, R. S. **Static and dynamic three-dimensional studies of water in soil using computerized tomographic scanning.** Soil Sci., 140:326-332. 1985.

CRUVINEL, P. E.; CESAREO, R.; CRESTANA, S.; MASCARENHAS, S. **X-ray and gamma-ray computerized minitomograph scanner for soil science.** IEEE Trans. Instr. Meas., 39:745-750. 1990.

DA SILVA, L. F. M.; SPADA, J. L. G. **The tragedy in Angra dos Reis in the passage of the year of 2009 to 2010 – design and recovery works.** Conferência Brasileira de Encostas – COBRAE 2013, Angra dos Reis, RJ, pp. 96-104 (in Portuguese). 2013.

DAL FERRO, N. et al. **Coupling X-ray microtomography and mercury intrusion porosimetry to quantify aggregate structures of a cambisol under different fertilisation treatments.** Soil Till. Res., 119, 13–21. 2012.

DAVARZANI, H.; SMITS, K.; TOLENE, R. M.; ILLANGASEKARE T. **Study of the effect of wind speed on evaporation from soil through integrated modelling of the atmospheric boundary layer and shallow subsurface.** Water Resour. Res., 50 (1), pp. 661-680, 10.1002/2013WR013952. 2014.

DAVID SUITS, L.; SHEAHAN, T. C.; MARINHO, F. A. M.; OLIVEIRA, O. M. **The filter paper method revisited.** Geotechnical Testing Journal. v. 19. doi: 10.1520/GTJ14125. 2006.

DAWSON, G. A. et al. **The acoustic output of a long spark.** J. Geophys. Res. 73: 815–16. 1968a.

DAWSON, G. A.; UMAN, M. A.; ORVILLE, R. E. **Discussion of paper by E.L. Hill, and J.D. Robb “Pressure pulse from a lightning stroke.”** J. Geophys. Res. 73: 6595–7. 1968b.

DE CAMPOS, T. M. P. **Resistência ao cisalhamento de solos não saturados.** Anais do 3o Simpósio Brasileiro de Solos Não-Saturados – ÑSAT'97, Rio de Janeiro. v. 2, pp. 399-417. 1997.

DE CAMPOS, T. M. P. **Relatório técnico de atividades**. REBIO-TRANSPETRO. 2012.

DE CAMPOS, T. M. P. et al. **Evaluation of the failure mechanism of an unsaturated tropical soil slope**. ASCE- Geotechnical Special Publication 147, pp. 485-496. 2006.

ECAGON. **Fundamentals and perspectives on soil moisture measurements**. <http://www.decagon.com/education/virtual-seminar-soil-moisture-401-fundamentalsand-perspectives-on-soil-moisture-measurements/> Acesso em : 25 nov. de 2018.

DECAGON. **EC-5 Manual**. <http://www.decagon.com/products/soils/volumetric-water-content-sensors/ec-5-small-soil-moisture-sensor/> Acesso em : 25 nov. de 2018.

DECAGON. **MPS-2 Dielectric Water Potential Sensor – Operator’s Manual**. V.1. 2011.

DIAMOND, S. **Pore size distributions in clays**. Clays and Clay Minerals 18, 7–23. 1970.

DIAMOND, S. - **A critical comparison of mercury porosimetry and capillary condensation pore size distributions of portland cement pastes**. Cement and Concrete Research 1, 531–545. 1971.

DIN ISO 11274: **Soil quality determination of the water retention characteristics** – Laboratory methods (ISO 11274:1998 + Cor. 1:2009) English translation of DIN ISO 11274:2012-04, Deutsches Institut für Normung, Berlin, Germany. 2012.

DRAKE, L. C. **Pore-size distribution in porous materials**. Ind. Eng. Chem., 41(4), 780–785. 1949.

DURIEZ, M. A. de M.; JOHAS, R. A. L.; BARRETO, W. de O. **Método simplificado para determinação do K_i e K_r na terra fina**. Rio de Janeiro: EMBRAPASNLCS, 10p. (EMBRAPA-SNLCS. Boletim de Pesquisa 2). 1982b.

DURNER, W. **Hydraulic conductivity estimation for soils with heterogeneous pore structure**. Water Resour. Res., 30, 211–233, 1994.

ELAT (2010) – **Lightning Distrubution: Website of the National Institute of Space Research**, INPE, Brazil. Available in: <http://www.inpe.br/webelat/homepage/>. Acessado em dez. 2011.

ELAT (2012) - **Lightning Distrubution: Website of the National Institute of Space Research**, INPE, Brazil. Available in: <http://www.inpe.br/webelat/homepage/>. Acessado em dez. 2012.

ELLIOT, T. R.; HECK, T. R. **Comparison of 2D vs. 3D thresholding of X-ray CT imagery**. Can J Soil Sci. 2007a;87:405-12. 2007a.

ELLIOT, T. R.; HECK, R. J. **A comparison of optical and X-ray CT technique for void analysis in soil thin section**. Geoderma; Vol.141. pp.60-70.2007b.

ELSTER, J.; GEITEL, H. **Ueber eine methode, die glektrische natur der atmosphaf ischen niederschlaege zu bestimmen**. (A new method to determine the electrical nature of precipitation). Meteorologische Zeitschrift, 23:95-i90. 1888.

ENTRALGO, J. F. T. **Statistical and spatial analysis of the mass movements triggered by the rains on the 11th and 12th of January of 2011 in the mountainous region of the state of Rio de Janeiro, Brazil**. M.Sc. Dissertation G. DM – 220/13, Civil and Environmental Engineering Department, University of Brasilia (in Portuguese). 2013.

FAISAL, H. A. **Unsaturated tropical residual soils and rainfall induced slope failures in Malaysia**. Proc. of the Asian Conference on Unsaturated soil, UNSAT-ASIA, Singapore, 41-52. 2000.

FEW, A. A. **Reply to letter by W.J. Remillard**. J. Geophys. Res. 74: 5556. 1969a.

FEW, A. A. **Power spectrum of thunder**. J.Geophys. Res.74: 6926–34. 1969b.

FEW, A. A. **Lightning channel reconstruction from thunder measurements**. J. Geophys. Res. 75: 7517–23. 1970.

FOURIE, A. **Predicting rainfall-induced slope instability**. Geotechnical Engineering 119(4):211-218. DOI: 10.1680/igeng.1996.28757. 1996.

FREDLUND, D. G.; MORGENSTERN, N. R. **Stress state variables for unsaturated soil mechanics**. J. Geotech. Engng Div., ASCE 103, No. GT5, 447–466. 1976.

FREDLUND, D. G.; KRAHN, J.; PUFAHL, D.E. **The relationship between limit equilibrium slope stability methods**. In Proceedings of the 10th International Conference on Soil Mechanics and Foundation Engineering, Stockholm, 3: 409-416. 1981.

FREDLUND, M. D.; FREDLUND, D. G.; WILSON, G.W. **An equation to represent grain-size distribution.** Canadian Geotechnical Journal, 37: 817–827. 2000.

FROIDEVAUX, P.; SCHLEMMER, L.; SCHMIDLI, J.; LANGHANS, W.; SCHÄR, C. **Influence of the background wind on the local soil moisture–precipitation feedback.** Journal of the atmospheric sciences 71, 782–799. 2014.

GARDNER, R. **A method of measuring the capillary tension of soil moisture over a wide moisture range.** Soil Sci. 43, No. 4, 277–283. 1937.

GERCOVICH, D.M.S.; VARGAS, E.A.; DE CAMPOS, T.M.P. **On the evaluation of unsaturated flow in a natural slope in Rio de Janeiro, Brazil.** Engineering Geology, Published by Elsevier, B.V. doi:10.1016/j.enggeo.2006.07.008. 2006.

GITIRANA JR, G. F. N.; FREDLUND, D. G. **Soil-water characteristic curve equation with independent parameters.** Journal of Geotechnical and Geoenvironmental Engineering, 130 (2), p. 209-212. 2004.

GLASSNER'S, A. **The digital ceraunoscope: Synthetic thunder and lightning, Part 1.** IEEE Computer Graphics and Applications. 2010a.

GOMES, M. A. S. S. **Lightning in the south-eastern region of Brazil in function of the geographic characteristics.** M.Sc. Dissertation, INPE (in Portuguese). 2002.

GUERRA, A. J. T.; DA CUNHA, S. B. **Geomorfologia: Uma Atualização de Bases e Conceitos.** Rio de Janeiro: Bertrand Brasil. p. 114. ISBN 85-286-0326-1 <http://dx.doi.org/10.1590/S0102-311X1995000200022>. 1994.

HAINSWORTH, J. M.; AYLMORE, L. A. G. **The use of computer-assisted tomography to determine spatial distribution of soil water content.** Aust. J. Soil Res., 21:1435. 1983.

HAJNOS, M.; LIPIEC, J.; SWIEBODA, R.; SOKOLOWSKA, Z.; WITKOWSKAWALCZAK, B. **Complete characterization of pore size distribution of tilled and orchard soil using water retention curve, mercury porosimetry, nitrogen adsorption, and water desorption methods.** Geoderma, 135, p. 307-314. 2006.

HAYAT, W. H.; BUCK, J. A. **Eletromagnetismo.** tradução JÚNIOR, A.S.; revisão JÚNIOR, A.P. – 7. Ed. – Porto Alegre: AMGH, 2011; ISBN 978-85-63308-76-4. 2008.

HERNANI, L. C. **Perdas de nutrientes e matéria orgânica por erosão: dez anos de pesquisa.** Dourados: Embrapa a Agropecuária Oeste. 14p. (Embrapa Agropecuária Oeste. Coleção Sistema Plantio Direto, 2). ISSN 1676-4412. 1999.

HERNANI, L. C.; FABRICIO, A. C. **Perda de água por erosão.** Embrapa – Dourados – MS. ISSN 1676-4412. 1999.

HILL, E. L.; ROBB, J. D. **Pressure pulse from a lightning stroke.** J. Geophys. Res. 73: 1883–8. 1968.

HOLMES, C. R.; BROOK, M.; KREHBIEL, P.; MCCRORY, R. **On the Power Spectrum and Mechanism of Thunder.** J. Geophys. Res., 76, pp. 2106-2115. 1971.

IASSONOV, P.; GEBRENEGUS, T.; AND TULLER, M. **Segmentation of X-ray computed tomography images of porous materials: a crucial step for characterization and quantitative analysis of pore structures.** Water Resour. Res., 45, W09415, doi:10.1029/2009WR008087. 2009.

IMHOFF, S. et al. **Porosity characterization of Argiudolls under different management systems in the Argentine Flat Pampa.** Geoderma, 158, 268–274. 2010.

IPT **Databank of casualties by landslides in Brazil.** Technological Research Institute of São Paulo – DIGEO/AGAMA/IPT (in Portuguese). 2016.

IRIS - STS-2. **Portable Very-Broad-Band Triaxial Seismometer.** Accessed in 05/11/2018 in https://www.passcal.nmt.edu/webfm_send/488. 1996.

KAPPUS, M. E.; VERNON, F. L. **Acoustic Signature of Thunder from Seismic Records.** Journal of Geophysical Research. Vol 96, No, D6, Pg. 10,989-11,006. 1991.

KARRAY, M. et al. Framework to assess the pseudo-static approach for the seismic stability of clayey slopes. Can. Geotech. Pp1-43 manuscript. 2018

KRAMER S. L. **Geotechnical Earthquake Engineering.** Prentice-Hall, Inc., Upper Saddle River, New Jersey 07458, pp. 434-437. 1996.

KUILA, U.; PRASAD, M.; DERKOWSKI, A.; MCCARTY, D. K. **Compositional Controls on Mud rock Pore-Size Distribution: An Example from Niobrara Formation.** SPE 160141-PP. Presented at presentation at the SPE Annual Technical Conference and Exhibition held

in San Antonio, Texas, USA, 8–10. 2012.

KUILA, U.; PRASAD, M. **Specific surface area and pore-size distribution in clays and shales.** *Geophysical Prospecting*, 61: 341–362. doi:10.1111/1365-2478.12028. 2013.

LACERDA W. A. **Stability of natural slopes along the tropical coast of Brazil.** In *Proceeding of International Symposium on Recent Developments in Soil and Pavement Mechanics*, Almeida M (ed.). Balkema: Brookfield; 17–39. 1997.

LEE, S. W. **Generating Synthetic Sound of Thunder** - Final Project M.S, Computer Science. University of North Carolina, Chapel Hill. 2009.

LEMES, M. W.; RODRIGUES, H. M.; ROSAS, R. O. **Comportamento hidrológico em latossolos sob diferentes sistemas de plantio: Subsídios à recuperação de áreas degradadas.** In: *Revista Digital Simonsen*. Rio de Janeiro, n.2. 2015.

LEOUREIL, S. **Geotechnics of slopes before failure. Proceedings of the Ninth International Symposium on Landslides, Rio de Janeiro.** *Landslides: Evaluation and stabilization*; Lacerda, Ehrlich, Fontoura & Sayao (eds), Taylor & Francis Group, London, vol. 2, p. 863-884. 2004.

LI, N.; GU, W.; DU, Z; SONG, P. **Observation on soil water content and wind speed in Erlianhot, a dust-source area in northern China.** <https://doi.org/10.1016/j.atmosenv.2006.04.019>. 2006.

LIM, T.; RAHARDJO, H.; CHANG, MING-FANG.; G FREDLUND, D. **Effect of rainfall on matric suctions in a residual soil slope.** *Canadian Geotechnical Journal - CAN GEOTECH J.* 33. 618-628. 10.1139/cgj-33-4-618. 1996.

LIMA, I. F. **The gravitational mass flow of Vieira, Teresópolis-RJ, megadisaster of 2011: description and classification,** VI Conferência Brasileira de Encostas – COBRAE 2013, Angra dos Reis, RJ, pp. 139-144 (in Portuguese). 2013.

LIN, T. L.; LANGSTON. C. A. **Ground motions induced by thunder: 1. Observations.** *J. Geophys. Res.*, 114, B04303, doi:10.1029/2008JB005769. 2009.

LIN, T. L.; LANGSTON, C. A. **Infrasound from thunder: A natural seismic source.** *Geophysical Research Letters*, Vol. 34. L14304, doi:10.1029/2007GL030404. 2007.

LUMB, P. **Effect of rain storms on slope stability.** Proc. Symposium on Hong Kong Soils, pp. 73-87. 1962.

LUMB, P. **Slope failure in Hong Kong.** Quarterly Journal Engineering Geology Pp. 31 - 95. 1975.

LUO, L.; LIN, H.; LI, S. **Quantification of 3-D soil macropore networks in different soil types and land uses using computed tomography.** J. Hydrol. 2010;393:53-64. 2010.

MACEDO, A.; CRESTANA, S. **Avaliação da macroporosidade e da densidade de partículas do solo através da microtomografia de raios-x.** Revista Brasileira de Ciência do Solo, 23(4), 763-771. <https://dx.doi.org/10.1590/S0100-06831999000400002>. 1999.

MARCUSON, W.; G. FRANKLIN, A. **Seismic Design, Analysis, and Remedial Measures to Improve Stability of Existing Earth Dams.** 23. 1983.

MARINHO, F. A. M. **Medição de Sucção Com O Método do Papel Filtro.** In: X Congresso Brasileiro de Mecânica dos Solos e Engenharia de Fundações. Medição de sucção com o método do papel filtro. Foz do Iguaçu. v. 2. p. 515-522. 1994.

MARINHO, F. A. M. **Medição de sucção em solos.** In: III Simpósio Brasileiro de Solos Não Saturados, Rio de Janeiro, RJ, v.2, p. 373-397. 1997.

MARINHO, F. A. M.; OLIVEIRA, O.M. **The filter paper method revisited.** Geotechnical Testing Journal, v. 29, n. 3, p. 1-9. 2006.

MARINHO, F. A. M.; TEIXEIRA, P. F. . **The Use of a High Capacity Tensiometer for Determining the Soil Water Retention Curve -** Technical note. Solos e Rochas, v. 32, p. 91-96, 2009.

MEDEIROS, V. S.; DE BARROS, M. T. L. **Analysis of the critical precipitation events occurred in the mountainous region of the Rio de Janeiro state in the days 11 and 12 of January of 2011.** XIX Brazilian Symposium on Hydric Resources, Maceio, AL, 19p. (in Portuguese). 2011.

MENDES, J. B.; LI, H.; XIN, H.; DO NASCIMENTO, J. W. B. **Evaluation of EC-5 Soil Moisture Sensors for RealTime Determination of Poultry Manure or Litter Moisture Content.** 2014.

MONCADA, M. P. H. **Avaliação de propriedades hidráulicas de solos tropicais não saturados.** 2008. Tese (Doutorado em Engenharia Civil) -

Pontifícia Universidade Católica do Rio de Janeiro, Rio de Janeiro, 2008.

MOTTA, M. F. B. **Physical-hydric-structural characterization and effect of air pressure increase on the shear strength of unsaturated tropical soils.** D.Sc. Thesis, DEC/PUC-Rio (in Portuguese). 2016.

MUÑOZ-CARPENA, R. et al. **Field Methods for Monitoring Soil Water Status.** 167-195. 10.1201/9781420032086.ch5. 2004.

NETTO, C. et al. **January 2011: The Extreme Landslide Disaster in Brazil.** 6. 10.1007/978-3-642-31319-6_51. 2013.

NEWMAN, M. M.; STAHMANN, J. R.; ROBB, J. D. **Experimental study of triggered natural lightning discharges.** Report DS-67-3, Project 520-002-03X, Federal Aviation Agency, Washington, DC. 1967a.

NEWMAN, M. M.; STAHMANN, J. R.; ROBB, J. D.; LEWIS, E. A.; MARTIN, S. G.; ZINN, S. V. **Triggered lightning strokes at very close range.** J. Geophys. Res. 72: 4761-4. 1967b.

NG, C. W. W.; SHI, Q. **A numerical investigation of the stability of unsaturated soil slopes subjected to transient seepage.** Computers and Geotechnics 22(1): 1-28. doi: 10.1016/S0266-352X(97)00036-0. 1998.

NIMER, E. **Climatology of Brazil. Brazilian Institute of Geography and Statistics (IBGE).** Rio de Janeiro. V. IV. (in Portuguese). 1979.

NUNES, A. L. L. S.; SAYÃO, A. S. F. J.; RIOS FILHO, M. G.; DIAS, P. H. V. **Disasters and actions in the natural slopes of Rio de Janeiro.** Conferência Brasileira de Encostas – COBRAE 2013, Angra dos Reis, RJ, pp. 74-96 (in Portuguese). 2013.

OJO, E.R. et al. **Calibration and Evaluation of a Frequency Domain Reflectometry Sensor for Real-Time Soil Moisture Monitoring.** Vadose Zone Journal, Vol. 14 no. 3; 2015.

OLIVARES, A.; PICARELLI, J. **Shallow flowslides triggered by intense rainfalls on natural slopes covered by loose unsaturated pyroclastic soils.** Géotechnique 53(2):283-287. DOI: 10.1680/geot.53.2.283.37268. 2003.

ORTIGÃO, J. A. R. **Applications in geotechnical engineering.** 4th Materials Conference, ASCE, 1996, 11p. 1996.

ORVILLE, R. E. **Spectrum of the lightning stepped leader**. J. Geophys. Res., 73, 6999–7008, doi:<https://doi.org/10.1029/JB073i022p06999>. 1968b.

ORVILLE, R. E. **Lightning detection from ground and space**. In **Handbook of Atmospheric Electrodynamics**. vol. 1, ed. H. Volland, pp. 137-49, Boca Raton, Florida: CRC Press. 1995.

ORVILLE, R. E. **A high-speed time-resolved spectroscopic study of the lightning return stroke: Part III, A time dependent model**. J. Atmos. Sci. 25: 852–6. 1968a.

PASSONI, S.; PIRES, L. F.; HECK, R.; ROSA, J. A. **Three-dimensional characterization of soil macroporosity by x-ray microtomography**. Revista Brasileira de Ciência do Solo, 39(2), 448-457. <https://dx.doi.org/10.1590/01000683rbc20140360>. 2015.

PATHAK, Y., & LOKHANDE, J. N. **Handbook of Metallonutraceuticals**. <http://www.crcnetbase.com/isbn/9781439836996>. 2014.

PENUMADU, et al. **Compressibility effect in evaluating the pore-size distribution of kaolin clay using mercury intrusion porosimetry**. Canadian Geotechnical Journal. 37. 393-405. 10.1139/cgj-37-2-393. 2011.

PETROVIC, A. M.; SIEBERT, J. E.; RIEKE, P. E. **Soil bulk density analysis in three dimensions by computed tomographic scanning**. Soil Sci Soc Am J. 46:445-50. 1982.

PLOUGONVEN, E. **Link between the microstructure of porous materials and their permeability**. Ph.D. Thesis, Université Bordeaux 1, Bordeaux. 2009.

PORTOCARRERO, H. **Avaliação do efeito de técnicas de bioengenharia em parâmetros hidrossedimentológicos utilizando instrumentação automatizada**. Tese de Doutorado, Pontifícia Universidade Católica do Rio de Janeiro – PUC-Rio. 2009.

Q330 – Quanterra Q330 - Low-power High Resolution Network Aware Seismic System. Accessed in 05/11/2018 in <http://www.q330.com/>. 2018.

RAB, M. A. et al. **Evaluation of X-ray computed tomography for quantifying macroporosity of loamy pasture soils**. Geoderma. 213:460-70. 2014.

RAHARDJO, H.; LEONG, E. C.; REZAUR, R. B. **Rainfall-induced slope failures: mechanism and assessment**. Keynote Lecture: International

Conference on Management of the Land and Water Resources, Hanoi, Vietnam, pp. 281-291. 2001.

RAHJARDJO, H.; ONG, T. H.; REZAUR, R. B.; LEONG, E.C. **Factors controlling instability of homogeneous soil slopes under rainfall.** J. Geotechnical and Geoenvironmental Engineering, ASCE 133 (12), pp. 1532-1543. 2007.

RAKOV, V. A.; UMAN, M. A. (2003) – **Lightning: Physics and Effects.** 3. ed. New York: Cambridge, v.II, 2005.

RASIAH, V.; AYLMOORE, L. A. G. **Computed tomography data on soil structural and hydraulic parameters assessed for spatial continuity by semivariance geostatistics.** Aust J Soil Res. 36:485-93. 1998.

REICHARDT, K. **A água em sistemas agrícolas.** São Paulo: Manole, 188p. 1990.

RIBNER, H.S. et al. **Computer Model of the Lightning – Thunder Process, with Audible Demonstration.** 2nd Aero-Acoustics Conference, Hampton, Va. 1975. 1975.

RIBNER, S. H.; ROY, D. **Acoustics of thunder: A quasilinear model for tortuous lightning.** University of Toronto, Institute of Aerospace Studies, Ontario, Canada M3 H5T6. 1984

RICHARDS, L. A.; WEAVER, L. R. **Moisture Retention by Some Irrigated Soils as Related to Soil-Moisture Tension.** United States Regional Salinity Laboratory, Riverside, Calif., Bureau of Plant Industry, Soils, and Agricultural Engineering, Agricultural Research Administration, United States Department of Agriculture Journal of Agricultural Research, Washington, D. C. vol. 69 no 6. 1944.

ROMERO, E.; SIMMS, P. H. **Microstructure investigation in unsaturated soil: a review with special attention to contribution of mercury intrusion porosimetry and environmental scanning electron microscopy.** In: Laboratory and Field Testing of Unsaturated Soils. Tarantino et al. (eds), p. 93-115. 2009.

SATYANAGA, A.; RAHARDJO, H.; LEONG, E. C.; WANG, J. Y. **Water characteristic curve of soil with bimodal grain-size distribution.** Computers and Geotechnics, 48, p. 51-91. 2013.

SCHOBENHAUS, C. et al. **Geologia do Brasil. Texto Explicativo do Mapa Geológico do Brasil e da Área Oceânica Adjacente incluindo Depósitos Mineraiis.** Brasília, DNPM-MME. 1984.

SEKI, K. **SWRC fit – a nonlinear fitting program with a water retention curve for soils having unimodal and bimodal pore structure.** Hydrology and Earth System Sciences Discussions, 4, p. 407-437. 2007.

SPRINGMAN, S. M.; THIELEN, A.; KIENZLER, P.; FRIEDEL, S. **A long-term study for the investigation of rainfall-induced landslides.** Geotechnique 63, No. 14, 1177-1193. <http://dx.doi.org/10.1680/geot.11.P.142>. 2013.

STOLF, R.; THURLER A. M.; BACCHI O. O. S.; REICHARDT K. **Method to estimate soil macroporosity and microporosity based on sand content and bulk density.** R Bras Ci Solo. 35:447-59. 2011.

TAINA, I. A.; HECK, R. J.; ELLIOT, T. R. **Application of X-ray computed tomography to soil science: A literature review,** Can. J. Soil Sci., 88, 1–20. 2008.

TIPPKÖTTER, R. et al. **Detection of soil water in macropores of undisturbed soil using microfocus X-ray tube computerized tomography (μ CT).** Soil Till Res. 2009;105:12-20. 2009.

TOLEDO, M. C. M.; OLIVEIRA, S. M. B.; MELFI, A. J. **Da rocha ao solo: intemperismo e pedogênese.** In: Decifrando a Terra, Companhia Editora Nacional, 2ª Edição, p. 210-239. 2009.

TOLL, D. G. **Soil suction monitoring for landslides and slopes.** Quarterly Journal of Engineering Geology and Hydrogeology, v. 44, p. 23-33. doi: 10.1144/1470-9236/09-010. 2011.

TOPP, G. C.; DAVIS, J. L. & ANNAN, A. P. **Electromagnetic determination of soil water content: Measurement in coaxial transmission lines.** Water Res. Res., 16:547-582. 1980.

TOPP, G. C.; DAVIS, J. L. & ANNAN, A. P. **Electromagnetic determination of soil water content using TDR: I. Applications to wetting fronts and steep gradients.** Soil. Sci. Soc. Am. J., 46:547-582. 1982.

TOWHATA, I. **Geotechnical Earthquake Engineering.** Springer, Tokyo, Japan. 2008.

TSAI, T-L. **Influences of soil water characteristic curve on rainfall-induced shallow landslides.** Environmental Earth Sciences. 64. 449-459. [10.1007/s12665-010-0868-9](https://doi.org/10.1007/s12665-010-0868-9). 2011.

UMAN, M. A.; COOKSON, A. H.; MORELAND, J. B. **Shock wave from a four-meter spark.** J. Appl. Phys. 41: 3148– 55. 1970.

VAN GEET M, LAGROU D, SWENNEN R. **Porosity measurements of sedimentary rocks by means of microfocus X-ray computed tomography.** In: Mees F, Swennen G, Geet U, van Jacobs P, editors. Applications of X-Ray computed tomography in the geosciences. London: Geological Society. p.51-61. 2003.

VARGAS, M. **Effect of rainfall and ground water levels.** Proceedings of the 4th Pan American. Conf. Soil Mech. And Foundation Engineering, vol 3. p. 1971.

VAZ, C. M. P.; CRESTANA, S. & REICHARDT, K. **Tomografia computadorizada na avaliação da compactação de solos.** R. Bras. Ci. Solo, 16:153-1159. 1992.

VELDKAMP, E.; O'BRIEN, J. J. **Calibration of a Frequency Domain Reflectometry Sensor for Humid Tropical Soils of Volcanic Origin.** Soil Science Society of America Journal. Vol. 64 no. 5 Soil Science Society - Madison, WI DOI: 10.2136/sssaj2000.6451549x URL: <http://dx.doi.org/10.2136/sssaj2000.6451549x>; 1549-1553. 2000.

VOSS, P. H.; DAHL-JENSEN, T.; LARSEN, T. B. **Acoustic events on a small seismological network – shock waves from thunder and fireballs.** © GEUS. Geological Survey of Denmark and Greenland Bulletin 33, 25–28. Open access: www.geus.dk/publications/bull. 2015.

WANG, W., KRAVCHENKO, A. N., SMUCKER, A. J. M., AND RIVERS, M. L. **Comparison of image segmentation methods in simulated 2D and 3D microtomographic images of soil aggregates.** Geoderma, 162, 231–241. 2011.

WRIGHT, M. W.; MEDENDORP, W. N. **Acoustic of radiation from a finite line source with N-wave excitation.** Kalamazoo College, Kalamazoo, Michigan. 1967.

WU, L. Z.; HUANG, R. Q.; XU, Q.; ZHANG, L. M. & LI, H. L. **Analysis of physical testing of rainfall-induced soil slope failures.** Environmental Earth Science. DOI 10.1007/s12665-014-4009-8. 2015.

ZEISS. **XRADIA 510 VERSA Submicron X-ray Imaging: Maintain High Resolution Even at Large Working Distances.** Technical Notes. 2017.

ZHANG, L.; LI, J.; LI, XU; ZHANG, J. & ZHU, H. **Rainfall-induced soil slope failure: stability analysis and probabilistic assessment.** CRC Press – Shangai Jiao University Press, 374p. 2016.